Vital Signs Monitoring Based On UWB Radar

Keyu Pan

A Thesis
in
The Department
of
Electrical and Computer Engineering

Presented in Partial Fulfillment of the Requirements
For the Degree of
Master of Applied Science at
Concordia University
Montréal, Québec, Canada

August 2021

CONCORDIA UNIVERSITY
School of Graduate Studies

This is to certify that the thesis prepared

By: **Keyu Pan**
Entitled: **Vital Signs Monitoring Based On UWB Radar**

and submitted in partial fulfillment of the requirements for the degree of

Master of Applied Science (Electrical and Computer Engineering)

complies with the regulations of this University and meets the accepted standards with respect to originality and quality.

Signed by the final examining committee:

________________________ Chair
Dr. John Xiupu Zhang

________________________ External
Dr. Muthu Packirisamy

________________________ Examiner
Dr. Wei-Ping Zhu

________________________ Examiner

________________________ Thesis Supervisor
Dr. Wei-Ping Zhu

Approved by ________________________
Prof. Wei-Ping Zhu, Graduate Program Director

September 1, 2021 ________________________
Prof. Mourad Debbabi, Dean
Gina Cody School of Engineering and Computer Science

Abstract

Vital Signs Monitoring Based On UWB Radar

Keyu Pan

Contactless detection of human vital sign using radar sensors appears to be a promising technology which integrates communication, biomedicine, computer science etc. The radar-based vital sign detection has been actively investigated in the past decade. Due to the advantages such as wide bandwidth, high resolution, small and portable size etc., ultra-wideband (UWB) radar has received a great deal of attention in the health care field. In this thesis, an X4 series UWB radar developed by Xethru Company is adopted to detect human breathing signals through the radar echo reflected by the chest wall movement caused by breath and heartbeat. The emphasis is placed on the estimation of breathing and heart rate based on several signal processing algorithms.

Firstly, the research trend of vital sign detection using radar technology is reviewed, based on which the advantages of contactless detection and UWB radar-based technology are highlighted. Then theoretical basis and core algorithms of radar signals detection are presented. Meanwhile, the detection system based on Xethru UWB radar is introduced. Next, several preprocessing methods including SVD-based clutter and noise removal algorithms, the largest variance-based target detection method, and the autocorrelation-based breathing-like signal identification method are investigated, to extract the significant component containing the vital signs from the received raw radar echo signal. Then the thesis investigates four time-frequency analysis algorithms (fast Fourier transform + band-pass filter (FFT+BPF), empirical mode decomposition (EMD), ensemble empirical mode decomposition (EEMD) and variational mode decomposition (VMD) and compare their performances in estimating breathing rate (BR) and heart rate (HR) in different application scenarios.

A python-based vital signs detection system is designed to implement the above-mentioned preprocessing and BR and HR estimation algorithms, based on which a large number of single target experiments are undertaken to evaluate the four estimation algorithms. Specifically, the single target experiments are divided into simple setup and challenging setup. In the simple setup, testees face to radar and keep normal breathing in an almost stationary posture, while in the challenging setup, the testee is allowed to do more actions, such as site sitting, changing the breathing frequency, deep hold the breathing. It is shown that the FFT+BPF algorithm gives the highest

accuracy and the fastest calculation speed under the simple setup, while in a challenging setup, the VMD algorithm has the highest accuracy and the widest applicability.

Finally, double targets breathing signal detection at different distances to the radar are undertaken, aiming to observe whether the breathing signals of two targets will interfere with each other. We found that when two objects are not located at the same distance to the radar, the object closer to the radar will not affect the breath detection of the object far from the radar. When the two targets are located at the same distance, the 'Shading effect' appears in the two breathing signals and only VMD algorithm can separate the breathing signals of the targets.

Acknowledgments

I would like to thank to my supervisor, Dr. Weiping Zhu for the huge support to me in this project. He was always helpful during any time I ran into issues or had any question and I would also like to thank him for believing in me and giving me the opportunity carry out this research.

I would also like to thank Dr. Jianfeng Gu from Moonshot Healthcare Company for giving me advice and helping me in this research. Both Dr. Zhu and Dr. Gu helped out in numerous situations such as, reserving and arranging laboratory environments for data collection/testing, getting ethics approval for tests, helping out in transporting equipment etc. in addition to helping out in conventional methods such as help solve problems on thesis.

I would also like to thank Moonshot CEO Etienne Lagace, Co-Founder Remy Beaumont, and my friends Dr.Mojitaba, Dr. Kalpesh Ranipa, Dr. Hongjiang Yu , Zhiheng Ouyang, Miao Wang, Jamil from Concordia University, who helped out in numerous ways such as helping out in conducting experiments, developing basic hardware drive code, working on commercializing this research, and in many other ways. Also my senior high school friend Jianmin Tu give me gave me great spiritual encouragement in my most difficult moment. Moreover, Dr. Weiping Zhu, Dr. Jianfeng Gu, and CEO Etienne, always believed in the potential of this research work and worked tirelessly to apply this research in real world situations to help elderly people in elder care facilities.

Finally and most important, I would like to express my sincere gratitude to my parents who always believed in me and helped me achieve all that I have achieved in life. My parents always put helping me in front of all other things in their life and their selfless commitment to help me have a better life.

Contents

List of Figures

List of Tables

Chapter 1

Introduction

1.1 General Background

Continuous monitoring of vital signs, like body temperature, blood pressure, heartbeat, and respiration rate is crucial as they provide key information about human's health condition and physical functioning. In particular, developing intelligent sensing technology and devices for measuring physiological signals/parameters becomes essential and imperative during the current pandemic time when all countries in the world are being affected by the coronavirus. As health care resources are insufficient to accommodate a large number of patients suddenly generated, majority of the patients are recommended and placed for home care. Hence, continuous monitoring of vital signs at home and work is necessitated in order to detect and track individual's health condition changes, especially for elderly and vulnerable ones.

Monitoring of human vital signs especially the heart rate and respiration rate, is not only crucial for diagnosis of fatal conditions, but also very important in many other areas such as fitness assessment and emotion recognition. For example, it can be applied to monitor the cardio-respiratory rates of athletes and non-athletes during exercises to regulate the desired intensity of exercise for the body. Moreover, complicated systems, including physically connected or integrated sensors and computers, are necessary to measure and control breath and heart rate. More importantly, traditional methods of detecting these vital signs leverage contact sensors, which is impractical for long-term monitoring and inconvenient for repeatable measurements. These contact sensors are mainly wearing devices such as electronic bracelets and chest-wearing receivers, in which the electric current is generated by direct contact between the electrode pad and the skin to monitor the characteristics of respiratory and heart rate after passing through the body. Unfortunately, most of these contact vital signs monitoring devices are of poor performance and bring an irritating effect on the user.

Contactless health monitoring devices or wireless body area networks (WBANs) perform physiological sensing, which collects massive data from human body [7], without physical contact, and analyse and report the physical characteristics of the human during daily life. Real time monitoring without wires or skin connection is a novel topic of research. Typical contactless techniques may leverage visual information, thermal sensors, acoustic changes, lasers, or radar to monitor the vital signs.

Among these contactless methods, one of the most commonly used ones is to leverage computer vision algorithms to analyze video streaming or photography [70]. For respiratory monitoring, one technique is to monitor the thorax's movement based on the surface of the thorax. The movements are captured by a camera under natural light and then projected with an intensity to estimate respiratory rate [60]. The other method is the infrared-video technique that the research group had developed to detect the elderly or ill people's paroxysm accidents in bed [2]. That system contains a fiber grating (FG) vision sensor and a processor module. The FG vision sensor includes an FG bright spots projector and a CCD camera, where the FG bright spots projector generates a dot-matrix light pattern of bright spots onto the plane. The spots projected on the object move to a certain orientation on the image plane of the CCD camera under the existence of object exists among the plane and the FG bright spots projector. The shift values of all spots can be changed into three-dimensional data of the object. With regard to monitoring the heartbeat, one interesting method uses cameras to perform the photoplethysmographic (PPG) imaging without contact [5]. A color video containing the human face is thus obtained through an ordinary camera, and is then converted into a digital signal, which will be processed by blind source separation to obtain the PPG signal. Finally, performing spectrum analysis of the PPG signal yields the heart rate estimate. Another technique measures heart rate by observing small head motions caused by blood flow during each heartbeat. Specifically, principal component analysis (PCA) is conducted on the recorded head movements to determine which movement is directly related to heartbeat [3, 59, 62].

The noncontact detection of human vital signal using radar appears to be a promising technology which integrates communications, biomedicine, computer science and other domain knowledge. The radar-based vital sign detection has been actively investigated in the past decade. In the search and rescue incurred by natural disasters such as earthquakes, high-power radar is used to scan the ruins find signs of life like survivors' basic physiological state [55, 65]. For the purpose of home medical care, radar monitoring equipment can remotely monitor the elderly and children's physiological conditions at home and transmit them to the user's mobile phone in real time [28, 88]. For heartbeat monitoring, a technique is proposed in [43] that can detect whether the driver's heart rate is too fast, thereby determining whether the driver performs fatigued driving [43].

Thermal sensing and imaging have also been studied in a variety of vital signs monitoring works. Typically, thermal imaging captures changes in facial skin temperature for monitoring the respiratory rate[72]. It can also be used for heartbeat monitoring by observing the changes in vein temperature due to pulsating blood pressure [21]. Results from several existing studies have proved the concept of thermal sensing in vital signs capturing but researchers have found that it is sensitive to movement [3, 21, 59, 62], making it less attractive in practical applications [1]. The authors in [76] have proposed a novel technique based on airflow-caused acoustic change, in which a speaker is employed to emit inaudible sound waves and a microphone is utilised to produce Doppler effect on breathing-caused ambient air. This technique can accurately carry out vital sign monitoring for sleeping subjects. Other contactless devices including laser [36], ultrasonic sensor [58] etc. have also been exploited to capture chest movement for breathing rate estimation. But they are not efficient for heart rate detection.

Although there are many techniques proposed in literature for vital signs monitoring, yet, many of them are suitable for practical. For example, infrared technology needs to focus the beam on the objects' chest at all times which is not realistic in continues monitoring. Also, both microphone and thermal imaging based detection methods are limited by strong ambient interference (such as noise, and other heat sources, etc.). The two most popular noncontact life monitoring methods that have been proven to be useful for real vital signal monitoring are video-based and radar-based life signal monitoring. However, the video-based breathing and heart sound detection technologies still suffer from many problems, such as lighting, blocking blind areas, and privacy issues. Moreover, most visual approaches can only measure respiratory signals but not efficient for heartbeat [64, 57, 5]. In contrast, vital sign detection based on radar surveillance has recently received much more attention for many reasons. First, it can accurately measure signals in the absence of light. Second, using radar signals can protect visual privacy and detect people through walls. Third, radar can capture large time-varying ranges and speed information about human breathing [8]. Finally, radar can separate the breathing and heartbeat signals more easily and display the objects' real-time life state intuitively.

It is known that ultra-wideband (UWB) radar has ultra-high resolution characteristics and can penetrate non-metallic materials, and thus is widely used in indoor vital signs monitoring. This thesis focuses on UWB radar based breathing detection and monitoring of breathing and heart rate. This research is a part of a Mitacs project, sponsored by Moonshot Health Company in Montreal, in which a collocation X4 series UWB radar from Xethru Company is used to collect vital signal data. The raw data are collected in the real scene processed by the algorithms designed in this thesis to estimate the breaths and heartbeats frequency. Ultimately, it is hoped that this thesis work promotes the application of UWB radar in human vital signs monitoring.

1.2 Literature Review

This section gives an overview of the radar-based bio-surveillance technology in general, as well as breathing and heartbeat monitoring algorithms based on UWB bio-radar. We will also summarize the advantages and disadvantages of bio-radar technology and algorithms, thereby providing background material to support the design and implementation work to be introduced in the later chapters of this thesis.

Bio-Radar Technology

A radar system makes use of electromagnetic waves to determine the distance, velocity, direction and elevation of stationary or non-stationary objects. Specifically, a bio-radar can accurately measure vital signals by transmitting a microwave signal and analysing the received signal that is reflected by a person's chest. The bio-radar technology is commonly classified as continuous-wave (CW) radar, frequency-modulated continuous-wave (FMCW) radar, and ultra-wideband (UWB) radar. However, respiratory and heart sound monitoring radar technology has been explored mainly using CW radar and UWB radar. The following section will give a brief introduction to CW radar and UWB radar.

The CW radar was first used to detect human body signs in the 1980s, as Lin etc. developed an X-band detection device [54] based on the single-frequency continuous-wave radar in which the X- band waves are radiated directionally to the subject's upper body in order to detect the displacement of the chest. The respiratory signal was extracted by comparing the received echo with transmitted wave. The attempt by Lin et al. triggered the research of radar monitoring of vital signs. Since then many researchers became interested in the use of radar for non-contact physical sign detection. The Droitcour research team in the United States designed a CW bio-radar in 2006 that can accurately detect abnormalities in cardiopulmonary information within a range of $2m$. Li et al. at the University of Florida developed a C-band portable vital signs CW radar system in 2007 [47]. It is shown that, when the transmission power is $20uW$, the accuracy of detecting human biological signals within $2.8m$ distance is as high as 80% [2]. Later, the same team developed an infant physical sign parameter detector based on a $5.8GHz$ CW radar in 2009, which can detect infant physical signs within $1.15m$. Also in 2010, the team developed a $5.8GHz$ CW radar chip with an adjustable bandwidth of more than $1GHz$ using $0.25m$ micron CMOS technology [17] and successfully detected vital signs with the chip in the laboratory.

Some researchers try to use multi CW radars or video-CW radar combined methods to remove complex noise and clutters generated by objects. Li et al. designed an array radar to eliminate strong noise caused by random movements of objects during non-contact vital signs monitoring. This technique uses two [48] or four [74] sets of transceivers and antennas to monitor signals from different parts of the body. Based on polarization and frequency reuse technology, the signals detected from other parts of the human body are combined. Finally, the noise caused by human body's random motion is eliminated by using the difference in patterns of human body's random motion and physiological motion signals. After the first version of the system, they developed a coin-sized CW radar system to monitor the human body in 2012 [6]. Moreover, this small radar chip can be easily embedded into various portable devices for the detection of multiple micro-motion information. Another CW radar for vital signs monitoring was proposed by Gu et al. [6] based on adaptive phase compensation. This system incorporates CW radar in a camera, where the camera detects vital signs by monitoring random body motion and then feeding them back to the CW radar as phase information.

Later, researchers have developed UWB radar utilized in various applications due to its robustness in a harsh situation, precise ranging at the level centimeters, low power consumption, and well object penetration capability [40]. Stanford University firstly applied UWB radar to vital sign detection in 1994. Then, in 2007, Zito D et al. proposed a wearable UWB radar device with a system-on-chip to detect heartbeats and respiratory rates [89]. Meanwhile, Russia's EGZiganshin's team developed a UWB radar to monitor the infant respiratory system [3]. This system can effectively prevent Sudden Infant Death Syndrome (SIDS). In contrast, the bio-motion UWB radar-based system reported by Philip de Chazal's et al. at the University of Sydney can identify adult sleep patterns/awaking patterns. Based on the measured motion signal, this radar classifies the monitored signal as sleeping or awaking within 30 seconds [12]. Besides, UWB radars have been used widely in the detection of people obscured by obstacles. In 2006, Levitas used a UWB radar with large operational bandwidth (11.7GHz) made by Geozondas Lithuania, to detect the breathing and heartbeat of a human standing 2.4m behind a wall [45]. In 2010, Levitas and Matuzas used one impulse UWB radar with an operating frequency of 2.5 GHz and a bandwidth of 0.5 GHz to detect the breathing of a target behind the wall. These researchers were able to discriminate the targets as being either human or a dog according to the breathing rate [84].

UWB Radar Based Vital Signs Monitoring Algorithms

Over the past decade, many effective vital signs detection algorithms have been developed based on UWB radar to deal with clutter and noise cancellation. K.-C. Lee et al. proposed a clutter removal algorithm based on singular value decomposition (SVD) in 2008 [42]. The received signals are arranged into a Hankel-form matrix and then decomposed into two subspaces: the noise-related subspace and the clean-signal subspace. Noise reduction is then performed by suppressing the noise-related subspace and retaining the clean-signal space only. Simulations demonstrate that the precision of target detection is significantly increased using the SVD noise-reduction technique. Donelli M. et al. proposed a clutter elimination algorithm based on independent component analysis (ICA) algorithm in 2011. The ICA algorithm can effectively remove most of the clutters of the echo signal, but it can't distinguish the bio-like clutters from the received signal [15].

In terms of the discrimination and separation of vital signs signals, In [40] ,the usefulness of the vital signs was demonstrated. The mathematical expression of the reflected signal involving breathing and heartbeats was accomplished. Then, an in-depth analysis of the intermodulation of breathing and heart rate signals was performed. Besides, to achieve accurate detection of the heart rate, a filter to suppress the harmonics of the breathing signal is proposed. Chang Li in [46] used the Welch periodogram introduced by P. Welch in [77] to identify the respiratory rate by searching for the frequency corresponding to the largest peak in Welch periodogram. The Welch periodogram outperforms the Fourier transform-based technique when the signal is unstable [77].

Jian et al. in [30], have used EMD to extract heartbeat and breathing signals from UWB radar returns. Their work focuses on reconstructing the heartbeat and respiration signal by combining multiple intrinsic mode functions that can be candidates for a respiration or heartbeat signal. However, this work does not lead to an automatic selection of the candidate IMFs and does not present a reference that can confirm the extracted signal is the correct respiration heart signal. The authors in [30] also suggested using a band-pass filter, after obtaining the combined signal from several IMFs to remove frequencies out of the heartbeat/respiration range. Sun and Li in [73] employed EMD to detect life in coal mines. Where the reflected signal is processed based on a Fourier analysis of each IMF to detect the dominant frequencies of the IMFs. The life signal is characterized by the presence of frequency components that are in the frequency ranges typically associated with breathing or heartbeat signals. A major drawback of their method is its inability to confirm whether the selected IMF is a human breathing signal or a noise signal falling within the same frequency range.

Authors in [50] have proposed SVD to remove dynamic clutter and an ensemble empirical mode decomposition (EEMD) based frequency accumulation algorithm for breathing frequency. Leib et al. have presented an autocorrelation-based receiver to detect vital signs, precisely the heart rate of a human [44]. A Wiener filter was adopted for deconvolution to improve the resolution of the signal. Besides, a wooden board was utilized for the UWB signal reflections, and it was demonstrated that UWB might also be beneficial for imaging systems since the UWB signal can go into the wooden board and is reflected from its both sides. Khan et al. [31] have established an accurate algorithm for vital signs measurement, containing noise reduction through a Kalman Filter (KF) and random body movement identification via the vital signal's autocorrelation. It was indicated that the KF could enhance the signal-to-noise ratio (SNR) of the signal, and the movement identification eliminated some outliers under the real-time monitoring where the person can easily move his/her hands, body, lips, and eyes.

In [14], the scholars have addressed the problem of the weak heart signal compared with the powerful breathing harmonics, making it challenging to separate the heart signal from the noise and breathing harmonics. They have presented a technique that employs the first valley-peak of IMF energy function (FVPIEF) obtained from a pseudo-bi-dimension ensemble empirical mode decomposition approach to extract the vital signals using the EEMD. In the [61], harmonic path and averaged harmonic path algorithms were established to estimate the vital signs under breathing harmonics. Moreover, A new multiple higher-order cumulant-based non-contact vital sign identification technique was established [80]. According to the characteristic of the vital sign for impulse ultrawideband radar, the quasi-periodic reflected echo in slow-time is analyzed. The mentioned technique was theoretically derived from fourth-order cumulant, and its superiority to the fast Fourier transform technique was demonstrated through simulations and experiments.

The recent progress in using UWB radar to detect and extract vital signs has been mainly on breathing measurement, heartbeat measurement and trajectory tracking. Machine learning and deep learning algorithms have been used in the detection of human features and activity trajectories. For example, in [24], the authors use the principal component analysis (PCA) algorithm [87] to extract vital signs from a single radar signal. PCA ensures the process results in a representation with lower dimensionality, thereby eliminating the interference of motion harmonics. And then, GoogleLeNet is used to learn the characteristics of the moving target for quantitative judgment, and the VGG convolutional neural network is finally exploited to determine whether the breathing and heartbeat are normal. This method can obtain accurate results and can recognize different biological events, for example, fall, sleep breathing, heartbeat, etc. in specific situations. However, when the target is stationary, the Doppler information is very weak or undetectable, and thus, it is difficult or impossible to distinguish between breathing state and clutters [39]. In addition,the author stated that in the case of many people walking randomly, the measurement results are inaccurate.

The literature on multi-person vital signs monitoring using UWB radar is limited. The paper [81] applied a single-input single-output (SISO) UWB radar system with high precision in through-wall multiple-target vital signs detection and VMD-based multiple-target vital signs tracking algorithm for through-wall detection. Taking advantage of the high-resolution decomposition of the

VMD-based algorithm, the respiration signals of different targets can be decomposed into different sub-signals, and then, the research group can track the time-varying respiration signals accurately when human targets located in the similar distance. After that, the author applied the algorithm to the detection of human vital signals behind a 0.15m thick concrete wall. The VMD-based algorithm has the superior capability of tracking multiple targets' vital signs in most detection applications like urban search and rescue missions. Similarly, an autocorrelation concept was first used by Shen et al. [68] for localization of the subject, and then a VMD algorithm is used for measuring the periodic vital signals. Researchers in [49] have used impulse radar for vital signal detection. The multiple automatic gain control (AGC) technique is used to increase SNR, thus enhancing the amplitudes of the breathing signals. The experiments were carried out in different environmental scenarios such as indoor, outdoor and actuator. Averaging filters were employed to increase the SNR value of the respiratory signal.

In paper [63], a logarithmic-based algorithm, suitable for UWB radars and multiple people real-time monitoring, was presented to distinguish the phase changes of reflected pulses induced by the tiny cardiac movements. The mentioned algorithm is superior to the traditional FFT vital signs detecting approach in respiration harmonics reduction and avoidance of interference in the respiration and heartbeat signals.

A discussion on the latest studies on vital signs evaluation through radar reveals that most scholars are now studying the robustness of the algorithms employed for vital sign extraction [33]. In summary,UWB radar technology is one of the rare technologies that can attain more popularity in the digital health industry.

1.3 Research Challenges

From above literature review, the UWB radar based human body signs monitoring is still in infancy. Although a number of UWB radar based solutions have been proposed for vital signal monitoring, the existing monitoring methods still face many challenges:

1. Object motion: From the previous literature review, one of the main challenges that researchers face and that limits the wide use of this technology in real scenarios is objects' motion on algorithms' performance. Researchers have provided different solutions for the assessment of vital signs of a non-stationary (random jogging, jumping) human subject [19, 41]. We can conclude that most life monitoring preprocessing algorithms can only eliminate simple noise and clutter. These algorithms cannot deal with the clutter and harmonics generated when the subject moves randomly or even shakes the body. Developing a new algorithm that can eliminate most of the human body's clutter is a huge challenge. If this problem is overcome, then this heath monitoring technology will be widely used in hospitals, nursing homes, and moving cars.

2. Single object monitoring in different positions: Most vital signs monitoring algorithms only measure the life signals when the body faces the UWB radar. However, even if objects remain stationary in an indoor scenario, it is impossible to face the radar all the time. Moreover, most UWB radars can not monitor faint heartbeats signal where there is a wall blocking and the signal is attenuated [11]. When the distance between the radar and the object is too far or the angle is too large, the clutter and noise will be much higher than the weak heartbeat signal or even the breathing signal. This means that most likely the reflected signal back to radar may not contain useful vital signals. If relevant information cannot be extracted, determining the precise angle and distance at which life information can be extracted is also a question that needs more in-depth research.

3. Multi-object vital sign monitoring: When the UWB radar system monitors multiple objects, their vital signs will likely overlap, interfere, occlude, and contain multiple echoes. These phenomena will seriously affect the stability and accuracy of monitoring results. In real applications, it is a significant challenge to develop efficient algorithms to extract multiple objects' life signals.

4. Limitation to ideal breathing and heartbeat scenario: The above references' [4, 68, 40] radar data are obtained in an ideal environment such as their laboratory. These data are too ideal such do not reflect practical measurement in real scenarios. In a real-world situation, there will be more metal objects, energized furniture (Electric heater, refrigerator, etc.) and walls from which these objects will reflect or shield the radar signal. It means that an echo signal obtained by a radar

system contains stronger clutter and noise. Moreover, the radar signal may get more reflections instead of being directly received by the receiver, which dramatically influences the radar's detection of the object's position. Therefore, in real scenarios, we need more powerful preprocessing algorithms and biological information separation algorithms to obtain accurate breathing and heartbeat calculations.

1.4 Contribution and Organization of the Thesis

The objective of this thesis is to design accurate and effective life signal detection algorithms to estimate breathing and heartbeat rates by using the UWB radar echo signals. The new algorithms are also expected to effectively capture and monitor the radar echo signals in complex application scenarios. The specific contributions are highlighted as follows.

a. Several preprocessing methods are investigated, including SVD-based clutter and noise removal algorithms, the largest variance-based target detection method, and the autocorrelation-based breathing-like signal identification method, to extract the significant component containing the vital signs from the received raw radar echo signal.

b. Fast Fourier transform + band-pass filter (FFT+BPF), Empirical mode decomposition (EMD), ensemble empirical mode decomposition (EEMD), and variational mode decomposition (VMD) methods are investigated to detect the breath signal and estimate the breath and heartbeat rates.

c. Based on the LUNNA embedded boards provided by Moonshot Health company and radar sensor provided by XeThru company, a software system is designed to implement the above-mentioned preprocessing and BR and HR estimation algorithms.

d. By using the designed system, a large number of single target experiments are undertaken in both a simple setup (facing with radar and normal breathing) and a challenging setup (side sitting, breathing frequency changing, breathing holding and deep breathing), to evaluate the four estimation algorithms. It is shown that the FFT+BPF algorithm gives the highest accuracy and the fastest calculation speed under the simple setup, while in a challenging setup, the VMD algorithm has the highest accuracy and the widest applicability.

e. Extensive experimental studies are also undertaken to estimate the breathing signals of double targets, where different locations of the two targets are considered. Our experimental results show that the target located at different distances to the radar do not interfere with each other. However, when the targets are very close or at same distance to the radar, only the VMD algorithm can separate mixed breathing signals.

It is to be mentioned that the work in this thesis is supported by a Mitacs Accelerate project with Moonshot Health in Montreal as industrial sponsor. While the thesis is mainly focused on the detection of vital signs using UWB radar, some other testing and data collection tasks are preformed but they are not included in this thesis, since these tasks are not closely related to the above-mentioned major contributions. One of those tasks, for example, is to establish radar echo data sets for human breathing signals that will be used for further development of machine learning algorithms for vital signal monitoring. The thesis is structured as follow:

The first chapter is the introduction, which covers the research trend in using UWB radar for vital sign signal detection briefly explains the application background and significance of UWB radar for non-contact vital sign signal monitoring. Moreover, this chapter elaborated on several main difficulties and corresponding solutions in the current research.

The second chapter introduces the principle of UWB radar based vital signs signal detection. The theoretical basis and core algorithms of radar signals detection are presented, at the same time, the detection system based on Xethru UWB radar is introduced.

The third chapter is dedicated to the introduction and optimization of the radar echo signal processing algorithms. Firstly, it introduces some preprocessing algorithms such as SVD-based clutter removal and noise cancellation, largest variance-based vital sign component extraction and the autocorrelation-based biosignal detection. After that, the FFT+BPF, EMD, EEMD, VMD algorithms are introduced to process the preprocessed components.

The fourth chapter comprises extensive experimental work to analyze and compare the algorithms introduced in the previous chapter. It is divided into two parts. In the first part, we study the accuracy and applicability of the four algorithms on single human vital signs detection (target facing the radar normal breathing) and challenging scenarios (side sitting, changing breathing frequency, hold the breath and deep breath). The second part is to study the possibility of vital signs signal detection in double-breathing scenarios, where the vital sign signals of two targets at different distances and the same distance are detected with the four algorithms under the condition of known distance. It is found that only the VMD algorithm can successfully separate the breathing signals of the two objects when they are at almost the same location.

The fifth chapter contains a summary of the thesis work, a description of the shortcomings of the current UWB radar detection method and a prospect of possible future work.

Chapter 2

Radar Technology in Physiological Sensing

2.1 Physiological Basis

Here, we first discuss the feasibility of bio-radar-based breathing and heartbeat monitoring, followed by an introduction of the radar cross-section (RCS), a key term that affects the intensity of radar echoes. A quick overview of the ECG method of estimating heartbeat and breathing rate, is also presented, since it will be used as ground truth in this thesis to verify the accuracy of radar detection.

2.1.1 Bio-Radar Detection

Previous literature review shows that the bio-radar can capture human's cardiopulmonary signal through the chest vibrations caused by breathing and the human body micro-movements generated by the heartbeat. From the perspective of the frequency domain, cardiopulmonary signals are of very low frequency. In a stationary state, the heartbeat frequency of adults is 50-100 beats per minute. The heartbeat of infants and young children or adults in exercise could be much faster, which can reach 200 beats per minute. Under normal circumstances, people breathe 8-24 times per minute [44]. Physiologically, breathing is detected through thoracic cavity palpation and observation. Table 2.1 shows the physical parameters of breathing and heartbeat in terms of chest wall's vibration amplitude [67]. Note that the vibration due to heartbeat is less than 0.6 mm, much smaller than the vibration caused by breathing. Although these vital sign signals are weak, they can be extracted by bio-radars [29].

Table 2.1: Physical parameters of breathing and heartbeat

	Frequency (Hz)	Body surface vibration amplitude(mm)
Breathing	0.13-0.40	4-12
Heartbeat	0.83-1.66	<0.6

Radar, known as Radio Detection and Ranging, operates by transmitting an electromagnetic signal and analyzing the signal returns or echoes, through which a target can be detected for its range and velocity. Suppose that a radar transmits a signal with power P_t (W). When the radar is transmitting with a balanced antenna, the power density S_1' at any target far away from the radar is equal to the power divided by the imaginary ball area $4\pi R^2$, namely,

$$S_1' = \frac{P_t}{4\pi R^2} \tag{2.1}$$

where R is the distance from the radar to the target. If the radar uses a directional antenna to concentrate the transmit power in certain directions and applies an antenna gain G to increase the power received at a target in the radiation direction, then, the power density illuminated by the target at distance R from the radar is modified as

$$S_1' = \frac{P_t G}{4\pi R^2} \tag{2.2}$$

The target intercepts part of the irradiation power and re-radiates it in different directions. The power scattered by the target depends on the radar cross-sectional (RCS) area σ, namely, it is given by $\sigma S_1'$. Thus, the power density of the echo signal arrived at the radar can be written as

$$S_2' = \frac{P_t G}{4\pi R^2} \frac{\sigma}{4\pi R^2} \tag{2.3}$$

The size of σ varies with the specific target, and it can be interpreted as the size that the radar 'sees'. If the effective receiving area of the antenna is A_e, then the echo power P_r in Watt (W) received by the radar is given by

$$P_r = \frac{P_t G A_e \sigma}{(4\pi)^2 R^4} \tag{2.4}$$

Usually, the radar transceiver uses a common antenna, where the antenna gain G is associated with the effective receiving area A_e by the following equation:

$$G = \frac{4\pi A_e}{\lambda^2} \tag{2.5}$$

where λ is the wavelength of the radar carrier frequency. Thus the power P_r of the received echo signal can be written as [4].

$$P_r = \frac{P_t\, G^2 \sigma \lambda^2}{(4\pi)^3 R^4}, \tag{2.6}$$

In the above analysis, it is assumed that the radar is far enough from the target such that the wave impinging on it is a spherical wave whose field intensity decays with the increase of distance R. Also, the target is small enough, such that the wave scattered by the target and received by radar is also spherical. Under these assumptions, the RCS can be expressed as [35].

$$\sigma = \frac{4\pi R^2 \left|E_s\right|^2}{\left|E_i\right|^2} \tag{2.7}$$

where E_i is the strength of the incident electric field at the target and E_s is that of the scattered electric field at the radar. It is of interest to mention that the radar cross-section can also be equivalently expressed using the corresponding magnetic field strengths. The commonly used unit for the RCS is square meter (m^2) or its decibel version $(dBsm)$, namely,

$$\sigma_{dBsm} = 10lg\sigma \tag{2.8}$$

With equation 2.7 the distance to the target or its maximum range considering a minimum received power at the radar can be determined. Researchers have already studied how the scattering of electromagnetic waves are produced by the human body.

Firstly, let us consider the effect of human body size on the RCS. Literature [34] pointed out that although there may be significant variation in the strength of radar signature for three body types(skinny, medium and fat) with respect to the aspect angle, the radar signature for these body types normally remains within a small range (between -3 and 1 $dBsm$) when the radar frequency varies from 0.5GHz to 4.5GHz. Typically, a skinny man has a greater RCS than a fat one while observed from front and back, especially for the considered low-frequency range. Simultaneously, his signature is less than that of the fat man when observed from profile. In general, human beings of any size or different height with any postures, when facing the radar, give a cross-sectional radar area of above -10 $dBsm$ which means their RCS is $0.1m^2$. Majority of bio-radars' resolution can reach the centimeter level so that vital signs can be captured.

Secondly, when radar's electromagnetic waves irradiate on the human body, both reflected waves and refracted waves will be generated on the human body surface. Only partial electromagnetic waves reflected by the human body surface are captured by the radar antenna, while partial electromagnetic waves will be transmitted into the human body and absorbed by body tissue. Since the radar's detecting ability depends on the received target echo power, it is important to investigate the modeling of human body surface and internal organs as well as their echos. Researchers at Nanyang Technological University (NFU) in Singapore used UWB pulse signals to measure the signal reflection from the interface between different biological tissue layers [9]. They modeled the human chest as a planar multilayered medium with one dimensional inhomogeneity, where the electromagnetic property is piecewise constant in each layer. They also proposed a multi-ray propagation model to take into account significant multipath components contributed to the received signal including the line-of-sight (LOS) component and the signals reflected by the air/skin/fat/muscle interfaces. Based on the proposed model, the time-of-arrival information of the echo is utilized to measure the breathing frequency.

2.1.2 Electrocardiogram

The Electrocardiogram (ECG) is a procedure of detecting the cardiac electrical activity through the action potential caused by heartbeats. Its basis is to measure the potential difference between two or more points on body surface of the subject [23]. ECG test is essential for diagnosing myocardial ischemia, arrhythmia and other cardiac diseases [27]. Although the main function of ECG machine is to monitor the signal of the heart, breathing rate can be evaluated by the ECG data analysis as well [18, 66]. This technique is called ECG derived respiration (EDR), which is in accordance with sinus arrhythmia process [25]. The 12-lead clinical ECG and the portable ambulatory ECG are two common types of ECG systems. To measure heart rate and its variability, a clinical ECG system is still the best method, even though it is bulky and expensive.

The traditional ECG measurement approach can only be performed in a hospital environment, where specific equipment and various wired direct-skin-contact electrodes are needed, which is not appropriate for long-term daily-life ECG monitoring due to the imposed skin irritation, movement artifacts, and daily-life disturbance induced by the wired electrodes. Scholars have constructed various monitoring systems to eliminate the mentioned deficiencies. For instance, dry electrodes and indirect contact approaches have been presented to alleviate skin irritation [10, 26]. Sensors integrated into the home, and office furniture and devices like chairs, toilet seats, baths, computer mice, and beds have been constructed to provide unlimited long-term monitoring [53, 52]. Wearable medical systems, which benefit from ubiquitously measuring physiological signals, have also been designed for daily physiological monitoring. Wearable medical devices have been developed through smartphones and their relevant applications [38, 86]. In this thesis work, a chest strap ECG is used as benchmark to compare with the breathing and heartbeat measurement acquired by the radar measurement.

An ECG device captures the electrical activity of the heart over time, as the heart contracts and relaxes. A typical waveform is shown in Figure 2.1. For a single heartbeat, the waveform consists of four segments: (1) P wave (represents atrial depolarization); (2) QRS complex (represents ventricular polarization); (3) T wave (ventricular repolarization); and (4) U wave (papillary muscle repolarization).

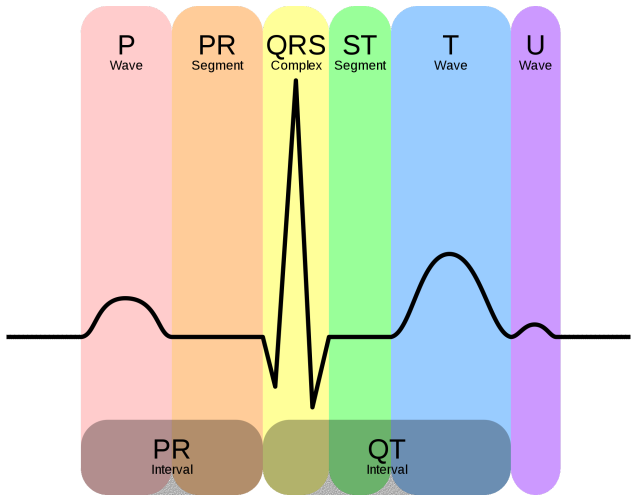

Figure 2.1: ECG waveform for a single heart beat (source: Wikipedia)

The heart rate is measured by calculating the interval between two heart beats, also called inter-beat interval (IBI). IBIs are most commonly measured using the R peak as the reference point, as shown in Figure 2.2. Because of that, the terms IBI and RR-intervals are used interchangeably. From IBIs, one can compute: (1) Instantaneous heart rate, as the inverse of the IBI; (2) Average heart rate, as a number of IBIs over some period of time divided by the sum of their durations.

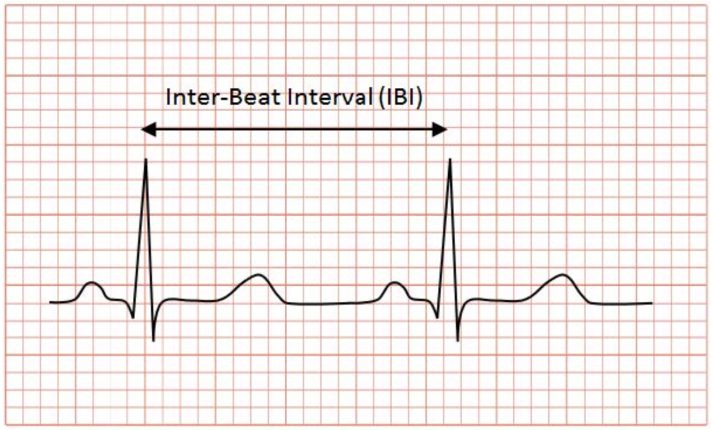

Figure 2.2: Inter-beat intervals (IBI)

2.2 UWB Radar Technology

In this section, we first introduce the basics of UWB radar to get a better understanding of UWB radar's advantages in monitoring vital signals. We will then describe the carrier-modulated signal and its echo as well as the structure of the radar transmitter. Finally, we will present a brief discussion on radar doppler frequency shift.

2.2.1 General UWB radar

An ultra-wideband signal has a bandwidth of a minimum of $25\ \%$ of its center frequency. This allows the UWB radar to place a subject with a precision superior to other radars. UWB radar operates based on transmitting narrow impulses on Nano or even Pico seconds, at high pulse repetition frequencies. Since these pulses have short periods, the range resolution is very high.

Here we focus on a UWB monostatic radar, i.e., a radar with the transmitter and receiver placed at a same location. A radar with a separated transmitter and receiver in space is called bistatic radar. Similarly, a radar with various receivers placed at different positions is called a multi-static radar. Nowadays, most indoor bio-monitoring radars use a monostatic module. Although it technically has a separated transmitter and receiver, they are very close, such that the radar is considered a monostatic radar. It has been utilized to distinguish the existence of people, to monitor respiration and track. Moreover, it emits little power, so its use is safe for human beings and animals.

The investigation of the UWB radar signal features demonstrates that the transmission of short duration and large bandwidth pulses makes the design of object detecting and monitoring algorithms more challenging than other radars. Various factors exist that affect the received signal, including the target's relative angle, distance, and frequency response. Besides, this makes the signal processing of UWB returned echoes more difficult than other radars. Compared with other radar systems, on the other hand, UWB radar has many advantages:

1. Strong ability to resist multipath fading: In the past, wireless communication technology could not develop rapidly due to multipath fading. Prior to the emergence of ultra-wideband technology, sine waves-based radio technology was more susceptible to multipath interference from surrounding complicated environment which degrades wireless transmission performance. UWB system has a very high operating frequency and a very low duty cycle. The duration of time returns through different paths is only nanoseconds. Moreover, the UWB radar is also differentiated from reflected channels based on the extremely narrow waveform. This will also lower the degree of multipath fading. In general, the pulse width of the transmitted signal is on the order of sub-nanoseconds. Finally, a distance resolution of the centimetre-level can be obtained.

2. Large capacity and high transmission rate: UWB signal has wide bandwidth which can be estimated from the channel capacity formula. The transmission rate of UWB signals can reach 500 Mbit/s [22], which leads to a more significant advantage in the application of short-distance sign detection.

3. Strong penetrating ability: Due to the ultra-wideband characteristics of UWB radar, it can distinguish many scattering points of the target, and accumulate the echo signals of each scattering point to enhance the signal-to-noise ratio and thus the resolution. Furthermore, UWB radar has a large bandwidth and can penetrate various non-metal obstacles [82]. As such, many hidden targets can be found.

4. Low power consumption and long sustainable use: UWB radar emits intermittent pulses at

the transmitter, each transmitted pulse lasting $0.20ns$ to $1.5ns$. The whole detecting duration and power consumption of the entire system are relatively low. Even in fast communication, a complete UWB radar system usually needs only about a few hundred microwatts to tens of milliwatts of electricity.

2.2.2 UWB radar signal acquisition

The target, along with a specific environment that the radar can distinguish, can be described as a set of point scatterers. Without loss of generality, the theory can be established with an individual point scatterer since one can suppose that the actual target and the multipath interference are a superposition of L-point scatterers. A short outline of a pulse radar employed in the current study is presented in Fig.2.3. It emits a pulse signal $s(t)$, captures the echo $r(t)$ from a single point scatterer, and downconverts it to baseband for further processing. The distance (range) between the radar and the point scatterer is denoted as $R(t)$ which is in general a function of time while the target is moving.

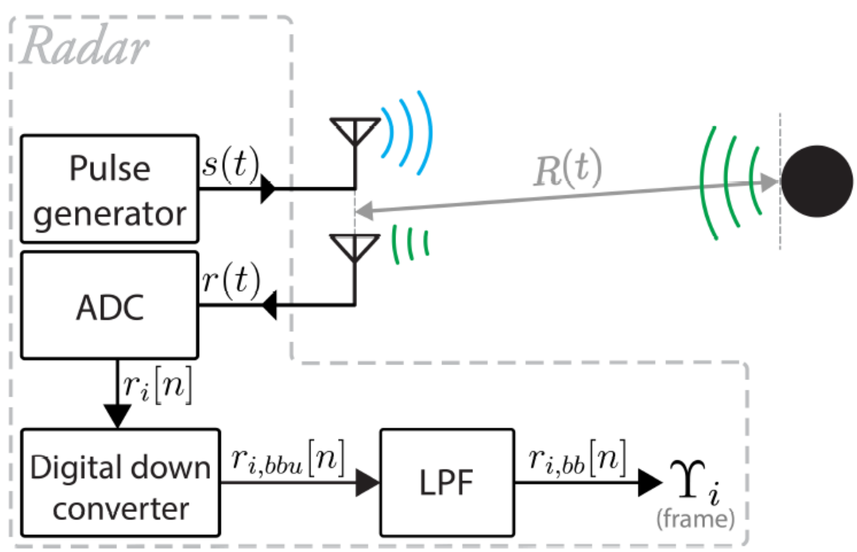

Figure 2.3: Conceptual overview of the radar with only one point scatterer ($L = 1$) [20]

In a real complicated environment, multipath propagation should be considered. For example, the electromagnetic waves transmitted by a UWB radar may be reflected by the metals and then radiated into the object. Thus, the waves radiated by radar system could reach the target through direct a path and multiple reflective paths. This is normally modelled as multipath propagation. For different applications, multipath propagation may give rise to complicated problems in target detection. Fig.2.4 indicates that the multiple paths between the radar and the target have different lengths. Assuming a line of slight or a direct path between the radar and the target is available, the non-direct or reflective paths are always be longer. In the figure, the black lines show the direct propagation, and the red lines denote the multipath propagation. When the radar receives multiple signals from different paths and the echo signals overlap, two problems may be caused: (1)the multipath signal may corrupt the direct-path radar echo if it is strong enough and has a similar propagation delay as the direct path; (2) the multipath echo may generate a 'ghosting target' in a longer range. Furthermore, it is difficult to distinguish the 'ghosting targets' in the long reflection path [13], because the UWB radar has a resolution of cm level, and any 'ghost targets' can clearly appear in the radar scan to confuse the real biological signal. Therefore, in the preprocessing of the radar echo signal and the separation of breathing and heartbeat, an attempt will be made to eliminate the influence of multipath propagations.

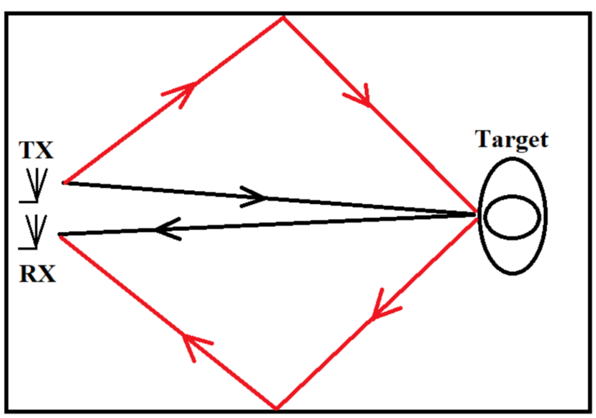

Figure 2.4: Multi-path propagation.

In detecting vital signs, the periodic change (for example continues breathing or heartbeat) of a target in the range is an important variable, rather than the absolute range to the target. At a good range resolution, the signal from both the real target and the phantom target will oscillate at the chest motion frequency. The radar will analyse this acquired information to detect the breathing rate and heartbeat. Irrespective of multipaths, it is still possible to estimate the range of the target. Moreover, by determining the shortest range from the target, the direct path can be identified.

Unlike most radars that downconvert the carrier radio frequency signal in the analog domain, the earlier XeThru UWB radar does this in the digital domain as outlined in Fig.2.3. Using an analog-to-digital converter (ADC) with an extremely high sampling frequency the radar digitizes $r(t)$ directly. However, the radar does not sample $r(t)$ all the time. Instead, it will digitize only a portion of $r(t)$ that covers the signal echoed by the target. This digital portion of r(t) is called a frame and thus the radar captures and holds signal samples for all frames.

In general, a radar manufacturer keeps the duration constant between two consecutive emissions of the pulse, and according to this constant duration, a window is set to determine the maximum scanning distance of the radar. Then within the maximum detection range, the frame span and offset are two important parameters of the whole frame which can be adjusted so that the frame span can cover the desired target (for example, the human body). This concept is illustrated in Fig. 2.5,which

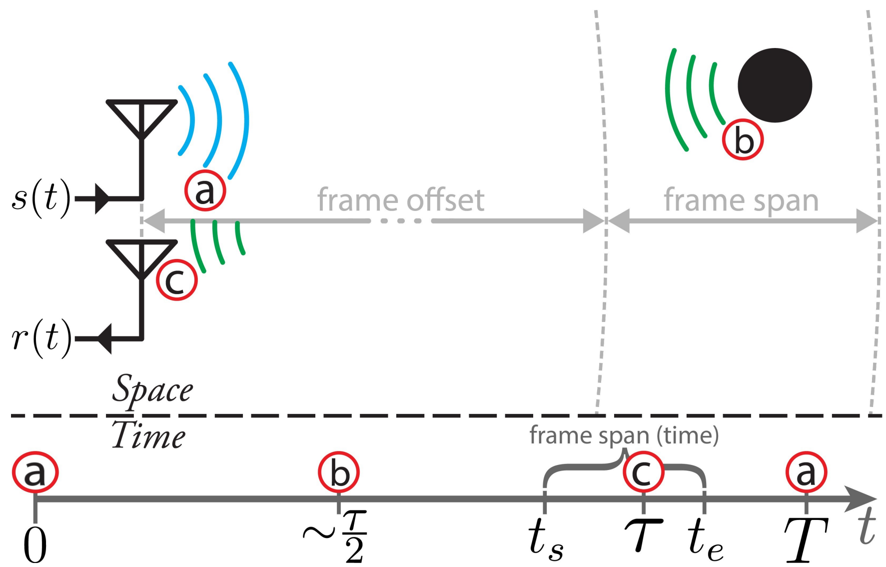

Figure 2.5: Frame offset and frame span illustrated, with a time line detailing when and where events happen. [20]

illustrates one cycle of emitting a pulse and recording its echo. Three letters, a, b, and c, indicate three time instants in one cycle where 'a' means t=0 when the radar begins emitting the first pulse, 'b' marks $t \approx \frac{\tau}{2}$, when the pulse is reflected off the target, and 'c' indicates $\tau = \frac{2R(t)}{c}$, which indicates the time when the reflected pulse arrives at the receiver. At $t = t_s$ the radar starts recording (sampling) $r(t)$ and this data sampling and acquisition process lasts until time t_e. Therefore, t_s and t_e should be set properly such that the entire echo is captured by the radar, thereby we have $t_s < \tau < t_e$. Moreover, if the farthest detection range of the radar is marked by the right "dashed line", then this location should correspond to t_e in the time axis of the echo signal. Similarly, the dashed line on the left represents time t_s. Therefore, the distance bounded by the two dashed lines which corresponds to time interval $[t_s, t_e]$ is referred to as the frame span. At $t = T$, the next pulse starts emitting, repeating the cycle again. Therefore, $f_p = \frac{1}{T}$ is called the pulse repetition frequency. Obviously, each pulse emitted will produce one frame.

The complete analog signal $s_i(t)$ sent by the radar, is defined as the sum of all carrier frequency modulated pulses, mathematically written as

$$s(t) = \sum_{i=0}^{\infty} p(t - iT)cos(2\pi f_c(t - iT)) \tag{2.9}$$

where f_c is the carrier frequency, and p represents the pulse waveform generated. For instance, Gaussian pulse is defined as

$$p(t) = a \cdot \exp\left(-\frac{\left(t - \frac{T_p}{2}\right)^2}{2\sigma_p^2} \right) \tag{2.10}$$

where a, T_p and σ_p^2 represent the maximum amplitude, the duration and the variance of the Gaussian pulse, respectively. Such a pulse is then modulated using a high-frequency carrier signal $cos(2\pi f_c t)$. Fig.2.6(a) illustrates the Gaussian pulse (typical values for σ_p and pulse duration T_p are $0.2ns$ and $1ns$ respectively) and the modulated version. Fig.2.6(b) shows a block diagram of a typical UWB signal generator. It is made up of a pulse producer and a modulator which can control the timing or polarization of the UWB impulse signal.

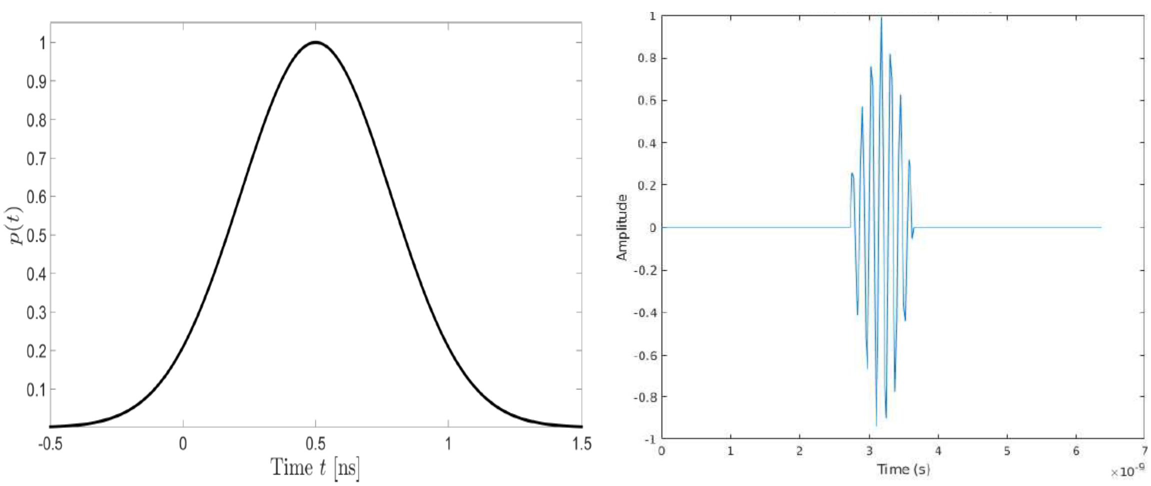

(a) Gaussian pulse (b) Modulated pulse signal

Figure 2.6: A Gaussian pulse and its modulated version

Following the notation in [20], we define t_f as the time variable within the time interval $(0, T)$.

Then the global time t can be written as

$$t = t_f + iT \tag{2.11}$$

With this definition of t it is easy to separate individual pulses (and therefore frames) using variable i. It follows that $t_f = t - iT$ when $t > T$, which means that the ith sent pulse can be written as

$$s_i(t_f) = p\left(t_f\right) \cdot \cos\left(2\pi f_c t_f\right) \tag{2.12}$$

By neglecting the attenuation, distortion and noise, the ith pulse being received by the antenna is the same signal as was sent, but now with a time delay τ.

$$r_i(t_f) = s_i(t_f - \tau) = p(t_f - \tau)cos(2\pi f_c(t_f - \tau)) \tag{2.13}$$

where τ is given as

$$\tau = \frac{2 \cdot R(t)}{c} = \frac{2 \cdot R\left(t_f + iT\right)}{c} \tag{2.14}$$

Substituting (2.14) into (2.13) results in

$$r_i(t_f) = p(t_f - \frac{2R(t_f + iT)}{c})cos(2\pi f_c(t_f - \frac{2R(t_f + iT)}{c})) \tag{2.15}$$

Figure 2.7 shows the block diagram of a typical UWB receiver which consists of a low-noise amplifier (LNA), a correlator and a template pulse generator. The oscillator drives the pulse generator and determines the pulse repetition frequency (PRF) of the UWB impulse system. After passing the LNA, the received pulse is coherently correlated with the template pulse generated by the pulse generator, converting the input modulated pulses into a digital signal.

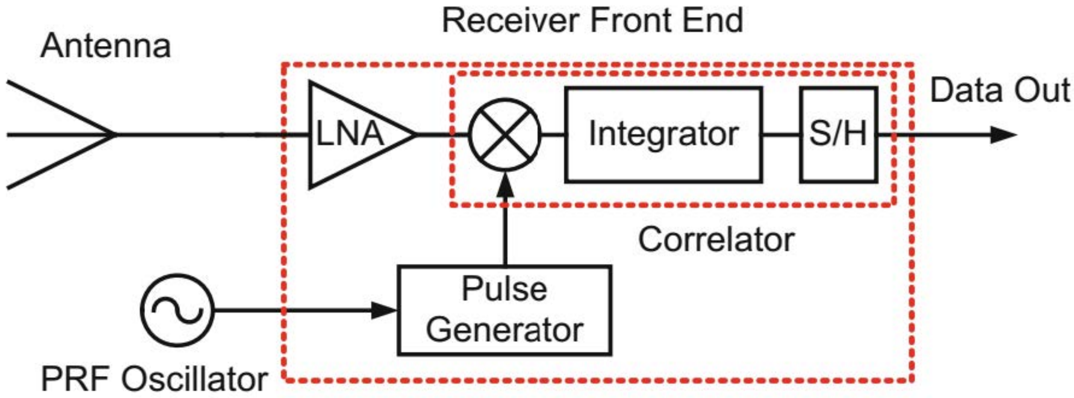

Figure 2.7: Block diagram of a typical pulse UWB receiver

In practice, we should consider the free space loss L of the receiving signal. The free space loss depends on the transmitted power P_t and the received power P_r, namely,

$$L = \sqrt{\frac{P_r}{P_t}} \tag{2.16}$$

where the power of the received signal at the LNA input is computed as:

$$P_r = \frac{P_t G_t G_r \lambda^2 \sigma}{(4\pi)^3 R_t^2 R_r^2} \tag{2.17}$$

where G_t and G_r are the gains of the transmitting and receiving antennas respectively, λ the wavelength of the radar carrier signal, σ the RCS of the target, R_t and,R_r are the ranges from the transmitting antenna and the receiving antenna to the target, respectively. We assume that the radar module has a monostatic configuration, which means that similar antennas placed at nearly the same location are used for transmitting and receiving. Then we have $G_t = G_r$ and $R_t = R_r$, thereby (2.16) can be simplified as

$$L = \sqrt{\frac{G^2 \lambda^2 \sigma}{4\pi^3 R^4}} \tag{2.18}$$

Moreover, the expression for the received signal becomes

$$r_i\left(t_f\right) = Lp\left(t_f - \tfrac{2\cdot R\left(t_f+iT\right)}{c}\right)\cos\left[2\pi f_c\left(t_f - \tfrac{2\cdot R\left(t_f+iT\right)}{c}\right)\right] \tag{2.19}$$

Following the sampling process in the ADC, we get $t_f = t_s + nT_s$, where T_s is the sampling period and $n = 0, 1, 2, \cdots N-1$, N being the number of samples to be recorded for each frame. The discrete-time version of the received signal is then given by

$$\begin{aligned} r_i\left[n\right] = r_i\left(t_s + nT_s\right) = Lp\left(t_s + nT_s - \tfrac{2\cdot R(t_s+nT_s+iT)}{c}\right) \\ cos\left[2\pi f_c\left(t_s + nT_s - \tfrac{2\cdot R(t_s+nT_s+iT)}{c}\right)\right] \end{aligned} \tag{2.20}$$

Considering that the distance traveled by the target during each frame is several orders of magnitude smaller than the range of the target, we have the following approximate relation,

$$R(t_s + nT_s + iT) \approx R(iT) \tag{2.21}$$

which means that the range to the target will remain unchanged throughout the frame. Accordingly, equation 2.20 can be simplified as

$$r_i[n] \approx Lp\left(t_s + nT_s - \tfrac{2\cdot R(iT)}{c}\right)\cos\left(2\pi f_c\left(t_s + nT_s - \tfrac{2\cdot R(iT)}{c}\right)\right) \tag{2.22}$$

Next, to perform downconversion, the received signal $r_i[n]$ is multiplied with a complex phasor of the radar carrier frequency (complex sinusoid), yielding

$$\begin{aligned} r_{i,bbu}\left[n\right] &= r_i\left[n\right]\exp\left(-j2\pi f_c\left(iT + nT_s\right)\right) \\ &= Lp\left(t_s + nT_s - \frac{2\cdot R\left(iT\right)}{c}\right) \\ &\frac{1}{2}\left[\exp\left(-\frac{j4\pi f_c R\left(iT\right)}{c}\right)\exp\left(-j4\pi f_c\left(t_s + nT_s - \frac{R\left(iT\right)}{c}\right)\right)\right] \end{aligned} \tag{2.23}$$

Then, the signal is filtered using a time-reversed version of the pulse-shaping filter function as given in equation 2.10, which serves as a matched filter that maximizes the signal to noise-ratio and to remove the high-frequency components present in equation 2.23, giving

$$r_{i,bb}\left[n\right] = \frac{1}{2}Lp(t_s + nT_s - \frac{2\cdot R\left(iT\right)}{c})\exp\left(-\frac{j4\pi f_c R\left(iT\right)}{c}\right) \tag{2.24}$$

The above equation describes one frame of the sampled baseband signal that corresponds to the $i-th$ received pulse by the radar.

The XeThru X4 series UWB radar used in this thesis has a build-in downconversion and decimation module that performs sampling, demodulation, filtering and decimation by a factor of 8 and then stores the low-sampling rate baseband data for further processing. The XeThru radar is configurable with two different bands, supporting two carriers frequencies: 7.29GHz and 8.42GHz. It uses a sampling rate of $F_s = 23.328GHz$ to sample the received RF signal to acquire up to 1536 samples per frame. The 1536 samples are also called $N_{samps} = 1536$ bins in the XeThru radar which record the radar signal received during a period of about $65.84ns$. The maximum target range that the radar can detect can be calculated by

$$range_{max} = \tfrac{1}{2}\tfrac{((N_{samps}-1)c)}{F_s} = 9.8701m \tag{2.25}$$

where $N_{samps} = 1536$, $F_s = 23.328GHz$, and $c = 3\times10^8 m/s$ is the speed of light. The X4 radar decimates the bins by 8, makes the maximum bin number 188, after rate reduction, which span the round trip of the radar pulse. In other words, each bin corresponds to a physical displacement of the target by 5.14 cm.

Fig.2.8 shows one frame of the radio frequency (RF) samples received by the X4 radar. The radar receiver has acquired 1536 bins starting from the beginning of transmitting the narrow pulse. The initial waveforms during the first 100 bins of the RF frame have large amplitude and represent the signal transmitted by the radar, which are followed by a small-amplitude waveform located around 200 bins denoting the received interference/clutters. The waveform marked by yellow circle represents the reflection of an object located at about 2 metters away from the radar.

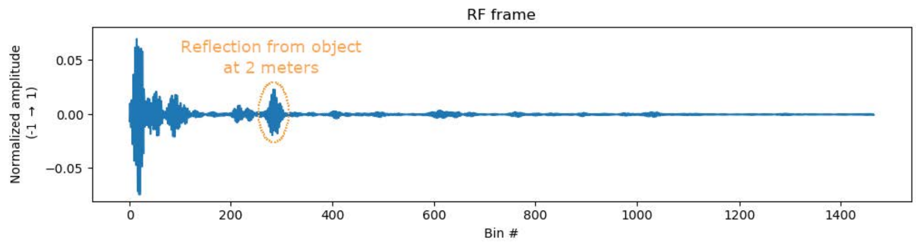

Figure 2.8: A RF data frame received by X4 radar

After digital downconversion, filtering out of band energy and decimating the samples with a factor of 8, a baseband data frame with 192 bins. Fig.2.9, shows the amplitude of the downconverted data, where the reflection from the object located at 2 meters can now be seen around bin 35.

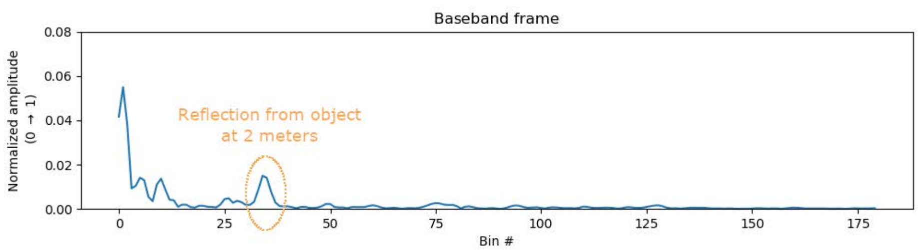

Figure 2.9: The baseband data frame after downconversion and decimation.

In pratice, the X4 radar captures multiple frames of data and save them in a 2-D data array (matrix). Fig.2.10 illustrates the array structure comprised of I columns, each column denoting one frame of the received N baseband samples. The frame index i is called slow-time and the sample index n within each frame is called fast time. Obviously, the fast-time corresponds to the distance of an object from the radar. The new X4 radar employs 30 frames of data samples in order to enhance the intensity of the object's echo signal, since a single frame is vulnerable to noise and may not provide reliable reflection.

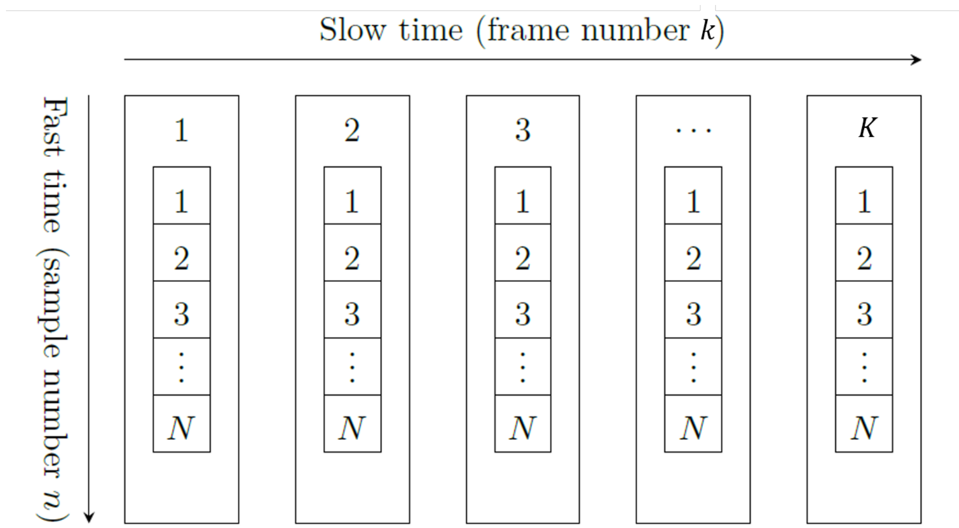

Figure 2.10: Multi-frame data array with slow-fast time scales

2.2.3 Doppler frequency shift

The Doppler frequency shift is often used in a radar system, to measure the displacement of a target. The Doppler effect causes the frequency of the received signal to differ from the original carrier frequency due to a motion that is increasing or decreasing the distance between the source and the receiver. When the distance between the target and the receiver remains constant, the electromagnetic wave is the same in both places. When the distance is increasing, the frequency of the received waveform is lower than the frequency of the target waveform. When the distance is decreasing, the frequency of the received waveform will be higher than the target waveform.

The Doppler effect can be used in radar, to measure the velocity of detected object. Suppose radar beam is fired at a moving car shown in Fig.2.11, where the car is approaching or receding from the radar source. When the car is moving toward the radar, each successive wave travels a lesser distance, thus decreasing the wavelength. Otherwise, when car is going away from the radar, the radar wave has to travel farther to reach the car, thus increasing the wavelength.

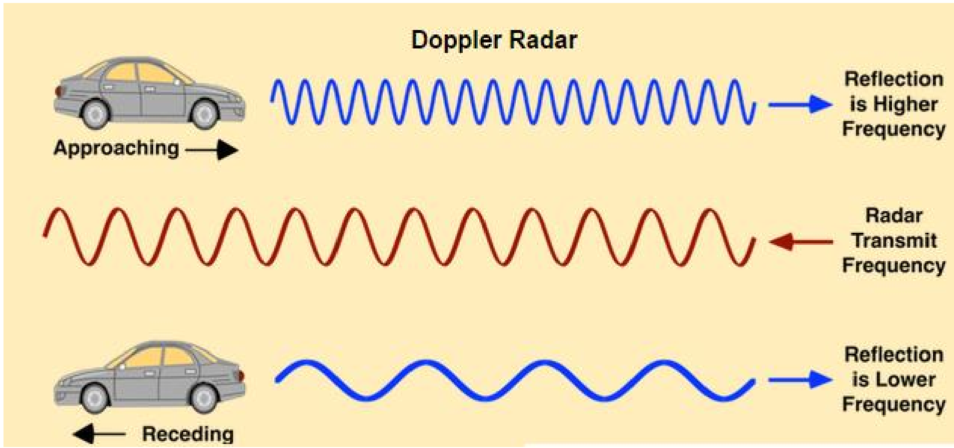

Figure 2.11: Doppler effect

When a radar signal is reflected by a moving target, the received signal has a Doppler shift given by

$$f_d = \pm \frac{2v_r}{\lambda} \tag{2.26}$$

where the positive sign is used for an approaching target which yields a positive doppler frequency shift, and in turn a negative is employed for a leaving target. The radial velocity v_r is defined by [4],

$$v_r = v \cos \theta \tag{2.27}$$

where v is the original velocity and θ is the angle between the object's forward velocity and the line of sight from the object to the radar receiver. Also,the carrier wavelength λ is given by,

$$\lambda = \frac{c}{f_c} \tag{2.28}$$

where f_c is the carrier frequency as mentioned above. By using equation 2.28, we can rewrite equation 2.24, showing the relationship between the range and the phase of the baseband signal in terms of the number of wavelengths:

$$r_{i,bb}\left[n\right] = p(t_s + nT_s - \frac{2 \cdot R\left(iT\right)}{c})\exp\left(-\frac{j4\pi R\left(iT\right)}{\lambda}\right) \tag{2.29}$$

According to equation 2.29, we define the phase term ϕ_i as

$$\phi_i = -\frac{4\pi R\left(iT\right)}{\lambda} \tag{2.30}$$

The rate of change of ϕ_i is the angular Doppler frequency $\omega_d = 2\pi f_d$, with f_d being the doppler frequency, namely,

$$\omega_d = \frac{d\phi_i}{dt} = \frac{-4\pi}{\lambda}\frac{dR\left(iT\right)}{dt} = \frac{-4\pi v_r}{\lambda} \tag{2.31}$$

As mentioned, the real targets can be modeled as a group of point scatterers. We therefore assume that the target and clutter can be modeled with L point scatterers. Then the ith frame, denoted as $\Upsilon_i[n]$, is expressed as

$$\Upsilon_i\left[n\right] = \sum_{l=0}^{L-1} p\left(t_s + nT_S - \frac{2R_l\left(iT\right)}{c}\right)\exp\left(-\frac{j4\pi R_l\left(iT\right)}{\lambda}\right) \tag{2.32}$$

where $R_l(iT)$ is the range of the lth point scatterer. Note that $\Upsilon_i[n] = r_{i,bb}[n]$ only when $L = 1$ if and if we ignore the unpredictable noise term.

Chapter 3

Vital Signal Monitoring

This chapter will first preprocess the fast-slow raw data matrix obtained in chapter two, extract the significant component containing the vital signs, and then introduce a few algorithms to estimate the heartbeat and respiration rates.

3.1 Preprocessing

3.1.1 SVD based clutter removal

The raw data generated from radar reflections include background noise and clutters, making direct detection of a target difficult. Singular value decomposition (SVD) based noise and clutter removal can be used for identifying and removing such noise and clutters [75, 71]. The raw radar data are organized as a $N \times K$ matrix where N is the number of range bins in the fast time direction and K is the number of frames (slow time). The number of frames K is assumed to be greater than or equal to the number of range bins for a sufficiently large time window [75]. Let X be an $N \times K$ matrix, and then the singular value decomposition(SVD) is given by

$$X = USV^T \tag{3.1}$$

where U and V are $N \times N$ and $K \times K$ matrices respectively with $U^TU = I_N, V^TV = VV^T = I_k$, and S is an $N \times K$ matrix whose main diagonal elements are non-negative square roots of the eigenvalues of $X^T X$ in decreasing order, called singular values. The non-diagonal elements of S are all zero. The columns of U and V are called the left and right singular vectors, respectively. Let the main diagonal elements of S be denoted as σ_i with $\sigma_1 \geq \sigma_2 \geq \cdots \geq \sigma_k \geq 0$ If $rank(X) = r$, we have $\sigma_{r+1} = \sigma_{r+2} = \cdots = \sigma_K = 0$. Then S can be simplified as

$$S = \left[\begin{array}{ccc|c} \sigma_1 & & & \\ & \ddots & & 0 \\ & & \sigma_r & \\ \hline & 0 & & 0 \end{array}\right]_{N \times K} \tag{3.2}$$

Using equation 3.2, X can be compactly expressed as

$$X = \sum_{i=1}^{r} \sigma_i u_i v_i^T = \sum_{i=1}^{r} M_i \tag{3.3}$$

where M_i are matrices of the same dimensions as X and are called as modes or ith eigen image of X. Through a large number of experiments, the authors in [71] found that the clutter information is contained in first eigen image. Thus, the clutter can be removed by applying SVD to the data matrix and then subtracting the the first eigen image matrix. In [75] Verma et al. reported that the target signal is mainly contained within the second eigen image, and accordingly, it can be extracted from the second eigen image. By decomposing X into three sub-images corresponding to clutter (M_c), target (M_t) and noise (M_n) [75], we get

$$X = M_c + M_t + M_n \tag{3.4}$$

where,

$$M_c = M_1 = \sigma_1 \times u_1 \times v_1^T \tag{3.5}$$

$$M_t = M_2 = \sigma_2 \times u_2 \times v_2^T \tag{3.6}$$

$$M_n = \sum_{i=3}^{r} \sigma_i \times u_i \times v_i^T \tag{3.7}$$

However, it was noticed that in most cases the target signal is also contained in the 3rd, 4th and other subsequent eigen images and thus part of the useful signal would be removed as noise when using only the second eigen image. Through extensive and corporation experimental studies for various scenarios, we found that most target information is contained in the $2nd$, $3rd$ and $4th$ eigen images.

Fig.3.1 shows an example of the SVD result of a fast-slow matrix, where the abscissa axis refers to the frames and the ordinate axis refers to the range bins (fast time). Moreover, the color represents the normalized amplitude where a bright color indicates a large amplitude which means a strong echo signal at that distance. In Fig.3.1(a), we can see that there is a great deal of clutter and noise during 0-30, and 40-60 bins. After clutter and noise removal using SVD, the fast-slow matrix is shown in Fig.3.1(b), which indicates a person located approximately 1m away from the radar as reflected in the interval of 20-30 bins. Moreover, we can see the breathing of the person, because during the breathing process, the chest cavity of the person moves which drives the entire body to move. At this time, the radar will detect a stronger echo signal (like the part in the orange circle). When breathing finishes, the person enters a short stationary state, then the radar echo signal at this time is weaker than that received during breathing (the part between the orange circles).

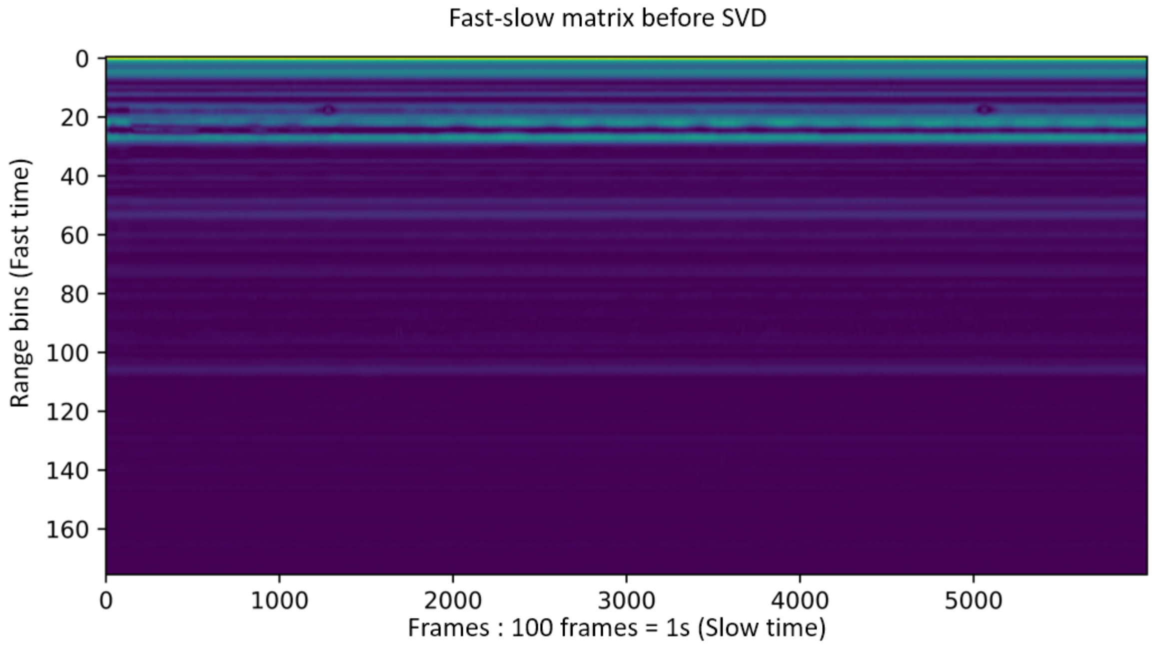

(a) Before SVD-based clutter removal

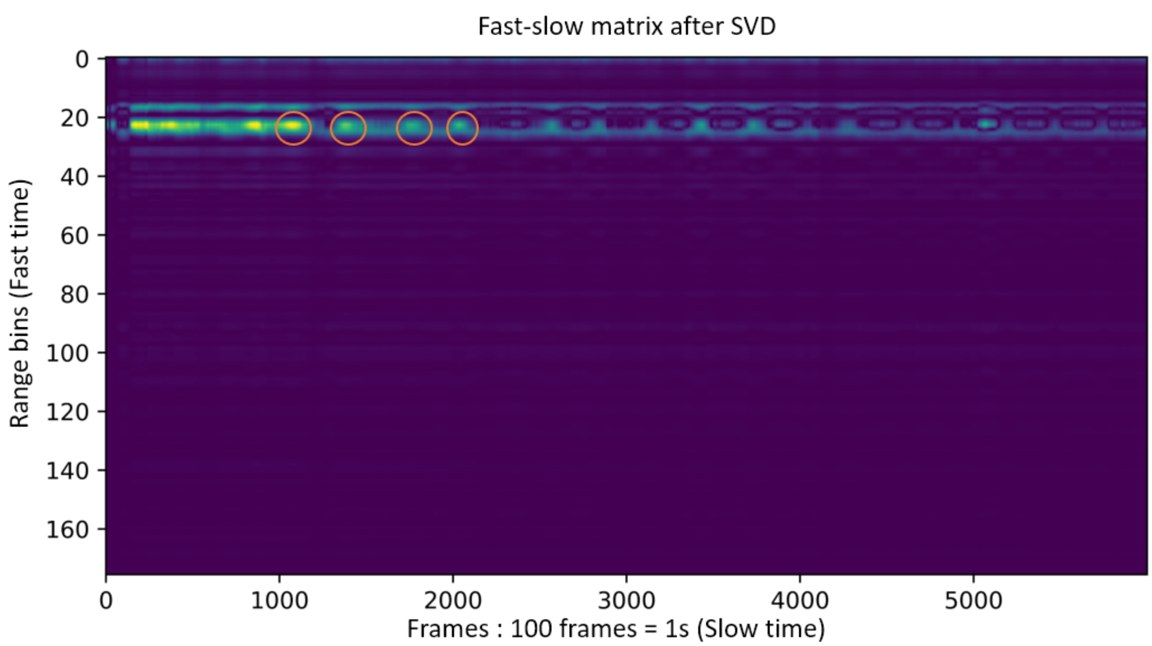

(b) After SVD-based clutter removal

Figure 3.1: Fast-slow data matrix before and after SVD-based clutter removal

3.1.2 Target location detection

Following the SVD-based prepossessing of the fast-slow time matrix , we determine the approximate location of the human body. Thereby, we will find the accurate position of the human chest in the matrix, based on which the rate of breathing and heartbeat will be estimated. In this section, we detect the range bin where a human target is located. To localize the echo data received from the chest vibration, we calculate the variance of each row of matrix X at different range bins. The maximum variance over range bins means the strongest chest movement [40]. Fig.3.2 shows an SVD-processed fast-slow matrix and the corresponding variance plot with respect to each bin. It shows the maximum variance occurring around bin 22 which indicates that the person is at a range approximately 1m from the radar. As can be seen from the figure, the variance at other bins is much smaller which means the radar echo at those bins almost remains unchanged or is slightly changed, namely, this kind of constant echo is not caused by chest movement. In conclusion, the row of the matrix with to the largest variance most represents the chest movement which contains heartbeat and respiration information. Therefore, this row of data is selected for further processing.

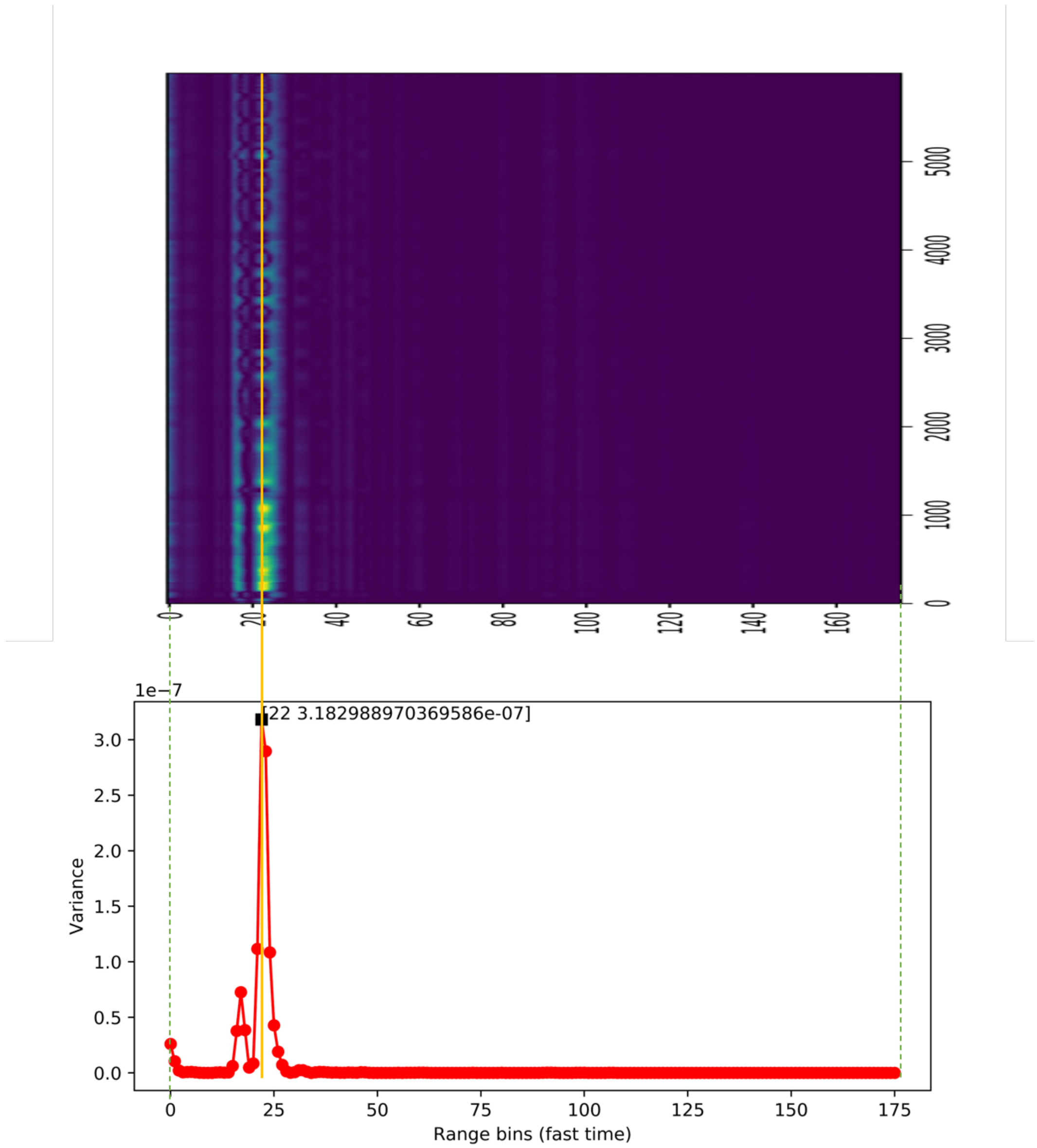

Figure 3.2: Variance of all range bins

3.1.3 Identifying the presence of a breathing-like signal

It should be mentioned that in the previous localisation and detection process of the chest movement, the human remains stationary during the measurement period. But this is not practical in real-world environment, since the radar is continuously monitoring the vital sign while the subject can not always keep stationary, and thus not all the measurement data can be used. Therefore, a motion detection algorithm is required to detect the motion of the human during the measurement process.

The auto-correlation function of the radar echo from a stationary human usually exhibits a wider main lobe as compared to that of a moving human. This is because there is comparatively less correlation among the signal samples when a person makes random body movements (RBM). If the main lobe width of correction function is significantly smaller, then we can determine that the person is moving and thus discard the measurement data [32]. Fig.3.3 illustrates the auto-correlation functions in three typical scenarios [31]. As pointed out by the authors in [32], the main lobe in Fig.3.3(a) is three-times wider than that in Fig.3.3(c). In particular, when a person stays still, the width of the main lobe like that in Fig.3.3(a) is about 2.04 seconds; When the human body moves slightly, the main lobe width is 1.47 seconds as shown in Fig.3.3(b). When human body moves randomly, the corresponding main lobe width is less than 0.25s as indicated by the distance of 'alpha' in the figure.

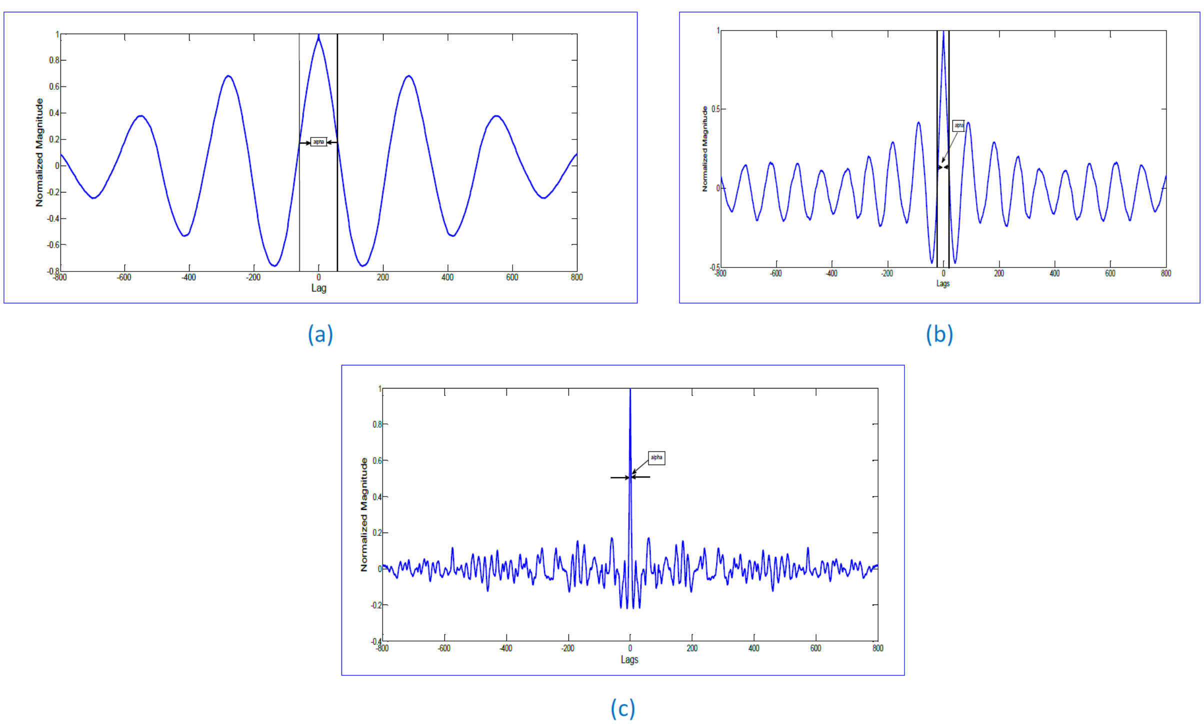

Figure 3.3: Auto-correlation signal of an object when it is: (a) stationary; (b) moving slightly; and (c) moving. [31]

Fig.3.4 presents a simple motion detection flow chat. The algorithm starts with an input of a largest-variance signal. Once a motion is detected, the algorithm discards the current bin and then picks the next valid bin with the largest variance.

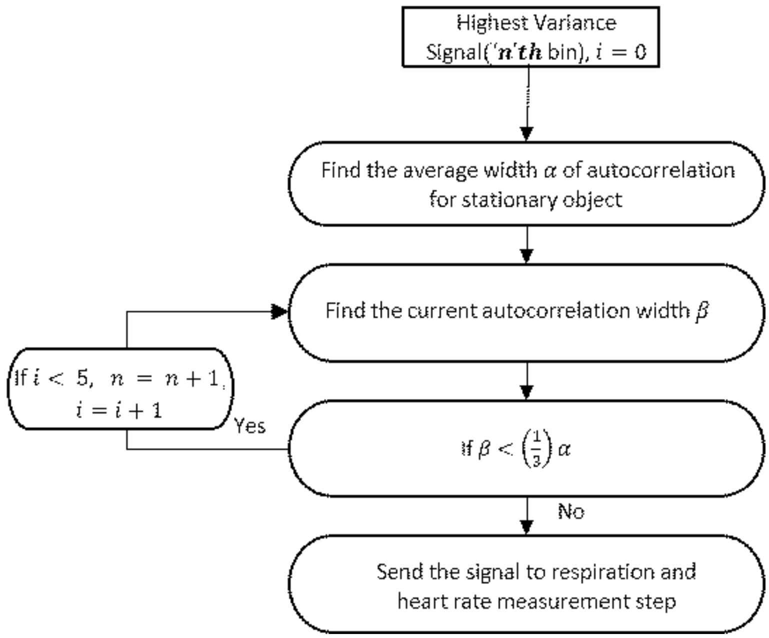

Figure 3.4: Object motion detection method

3.2 Breathing and Heart Sound Rate Estimation

3.2.1 FFT+BPF based breathing and heart sound rate estimation

Having detected the correct bin that contains true vital signal, the next task is to estimate the breathing and heart sound rate.

Analysis of the Fourier transform of a signal is one of the most prevalent methods to estimate a specific signal's repetition rate. The authors of [51] utilized some FFT-based methods to estimate phase and frequency and also discussed zero-crossing based phase and frequency estimation methods.

If the UWB radar captured signal includes a pure sinusoidal breathing signal, the estimation of breathing rate would be as simple as the estimation of frequency of this sinusoidal signal. Moreover, the signal is captured from the movements of the abdomen and chest as such movements take place in parallel with the human breathing. As shown in [56], the UWB radar captured signal can be modelled as

$$d(t) = d_0 + m_c(t) + m_a(t) = d_0 + \sum_{i=1}^{P} c_i \sin(2\pi i f_b t) + \sum_{j=1}^{Q} a_j \sin(2\pi j f_b t) \tag{3.8}$$

where $m_c(t)$ refers to the abdomen movement and $m_a(t)$ refers to the chest movement, and d_0 is the distance between the target and UWB radar. Further, c_i and a_j are the harmonic components of chest displacement and harmonic components of the abdomen displacement respectively and f_b is the breathing frequency. Finally, P and Q refer to the number of significant components of the chest and that of abdomen movements, respectively.

As seen from equation 3.8, since the signal contains harmonic components of the fundamental breathing frequency, summing up multiple harmonic components of the breathing signal and getting the frequency component with the maximum magnitude value would result in the fundamental breathing frequency.

As mentioned in chapter 2, the frequency range of breathing rate is between 0.13-$0.40Hz$, and the heartbeat is between 0.83-$1.66Hz$. Then, we let the series pass through a band-pass filter (BPF) that selectively passes the frequency components between 0.1-$0.75Hz$ and 1-$3Hz$ respectively to separate the breathing and heart sound parts (considering some extreme situations where the heart rate may be increased after strenuous exercise, and/or the breathing rate may be increased during tension, etc., we have increased the bandwidth of the band-pass filter to ensure that more accurate data can be obtained). The separation of the heart rate (HR) and breathing rate (BR) parts can be observed clearly by comparing Fig.3.5 and Fig.3.6 before and after passing through the BPF.

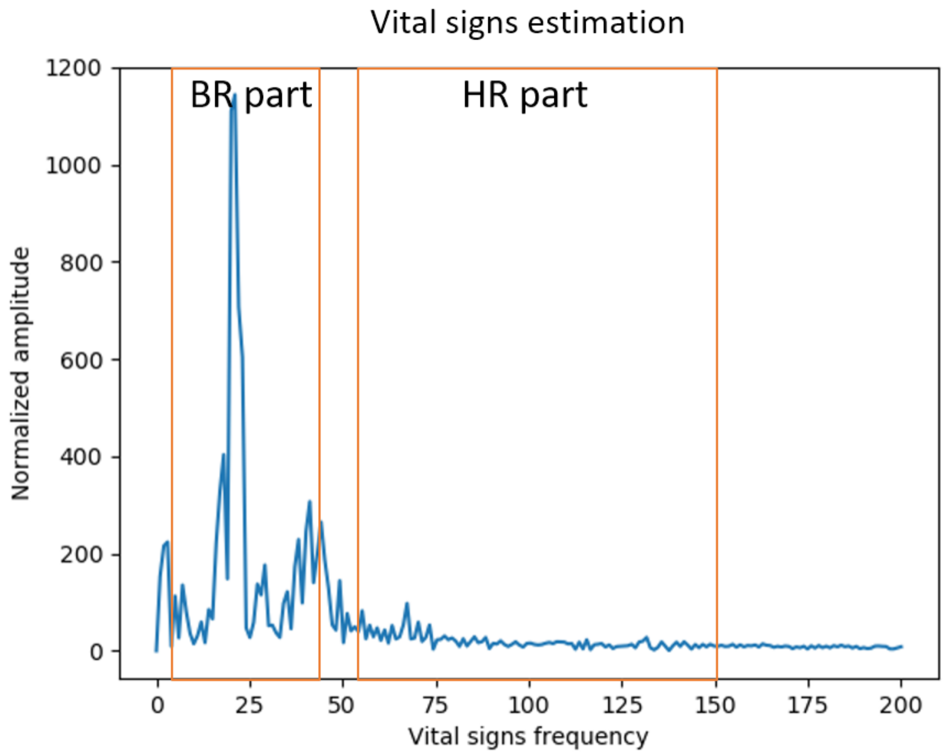

Figure 3.5: The spectrum of the vital signal.

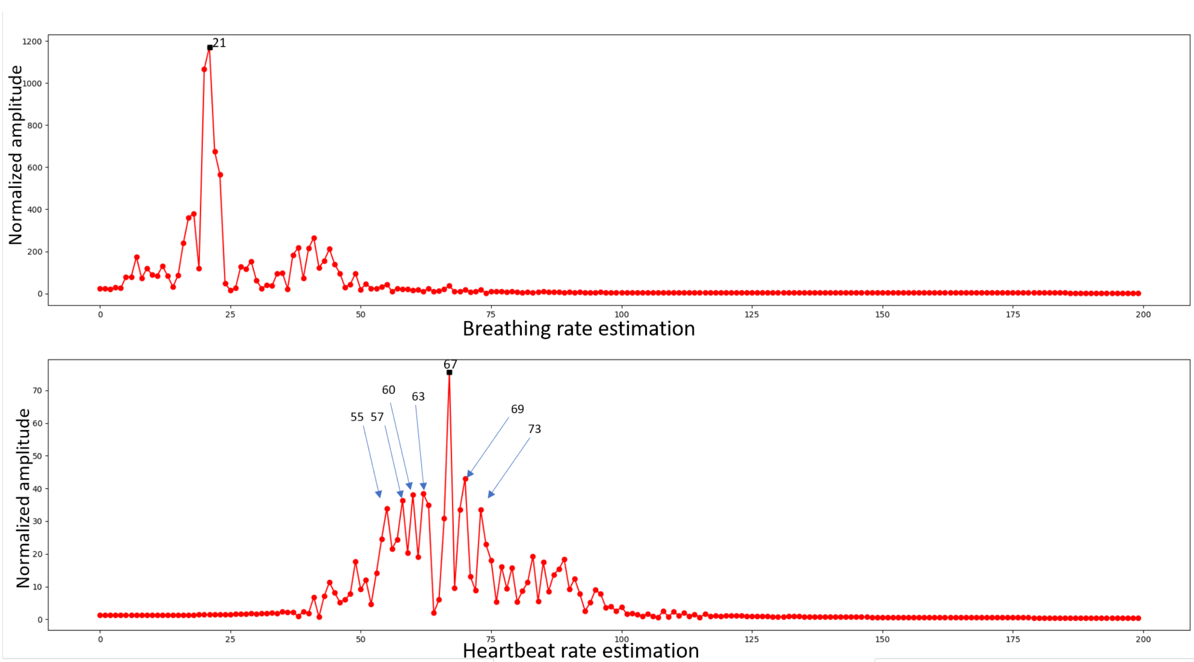

Figure 3.6: The breathing and heart sound rate estimation.

Even though the current algorithms perform generally well when the vital signs signal is model by equation 3.8, yet due to the sub-harmonics of the breathing rate [37] involved in the heartsound signal, the frequency summation algorithms may fail since they tend to choose sub-harmonics rather than the correct component corresponding to the actual HR.

In this thesis, we adopted an algorithm in [31] to extract the HR by selecting the peak location based on the probability of occurrence. In the algorithm, after performing the HR band-path filtering, we first find the highest frequency peak in the HR range. If HR is integer multiples of BR, we will discard the peak and then choose the second peak. Doing so may cause the heartbeat to be deleted when it is an integer multiple of the respiratory harmonic order. However, when the respiratory harmonic and the heartbeat frequency are the same, the breathing harmonics may have a higher magnitude than the heart rate [31] which means we cannot accurately separate the respiratory harmonic from the heartbeat signal. The authors in [31] proposed an iterative method to perform multiple iterative calculations, that is, to calculate the heartbeat from part of data and average the heartbeats obtained at each partial time. However, in actual scenarios, this method still has deviations due to individual differences.

3.2.2 EMD based breathing and heart sound detection

Empirical mode decomposition(EMD) is an efficient method for analyzing nonlinear and non-stationary data. Its basic idea is to decompose the data into a finite number of intrinsic mode functions (IMFs). The IMF satisfies two conditions:

(i) The number of extrema and the number of zero crossings must either be equal or differ at most by one.

(ii) At any point, the mean value of the envelope defined by the local maxima and that by the local minima is zero.

These conditions indicate that the intrinsic mode function is a single-component signal. That is, any given multi-component signal $s(t)$ can be decomposed into several single-component signals with the EMD approach.

The EMD algorithm works by extracting IMF step by step in an empirical manner. The process of extracting IMFs involves a procedure called sifting, which is briefly described as follows:

- Step1: Find all local extreme points of the signal $s(t)$, including local maximum and minimum points.

- Step2: Apply cubic spline interpolation to local maximas and minimas obtained in step (1), respectively to achieve a upper envelope $S_{\max}(t)$ and a lower envelope $S_{\min}(t)$, based on which the following envelope mean $m_1(t)$ is calculated,

$$m(t) = \frac{S_{\max}(t) + S_{\min}(t)}{2}. \tag{3.9}$$

Fig.3.7 demonstrates the decomposition results from from the above two steps, where black color plot denotes original signal, red color means lower envelope, blue color means the upper envelope and pink one is mean envelope.

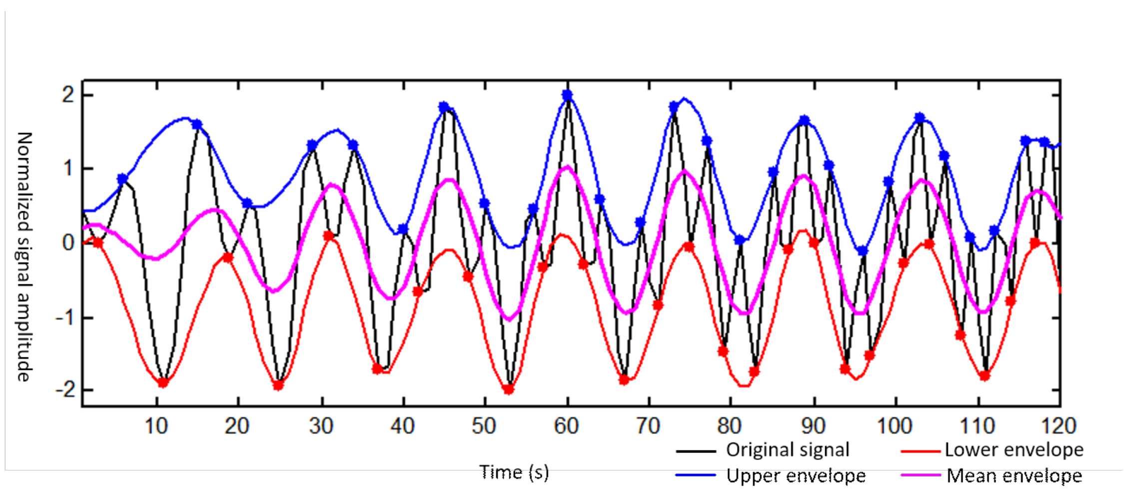

Figure 3.7: Envelope mean value graph

- Step3: Find the difference between the original signal $s(t)$ and the envelope mean $m(t)$, denoted by.

$$h(t) = s(t) - m(t) \tag{3.10}$$

If $h(t)$ satisfies the aforementioned two conditions for intrinsic mode function, then it is called the first intrinsic mode component of the original signal $s(t)$, denoted as $imf_1(t)$.

- Step4: When $h(t)$ does not satisfy the requirements of intrinsic mode function, let, $s(t) = h(t)$ and repeat step 1 to 3 until $h(t)$ satisfies the IMF conditions. The above process continues till $imf_1(t)$ is obtained. Next, define the residue function ad,

$$r_1(t) = s(t) - \mathrm{i}mf_1(t) \tag{3.11}$$

Fig.3.8 shows the residual signal and the corresponding upper and lower envelops as well ad their mean plot.

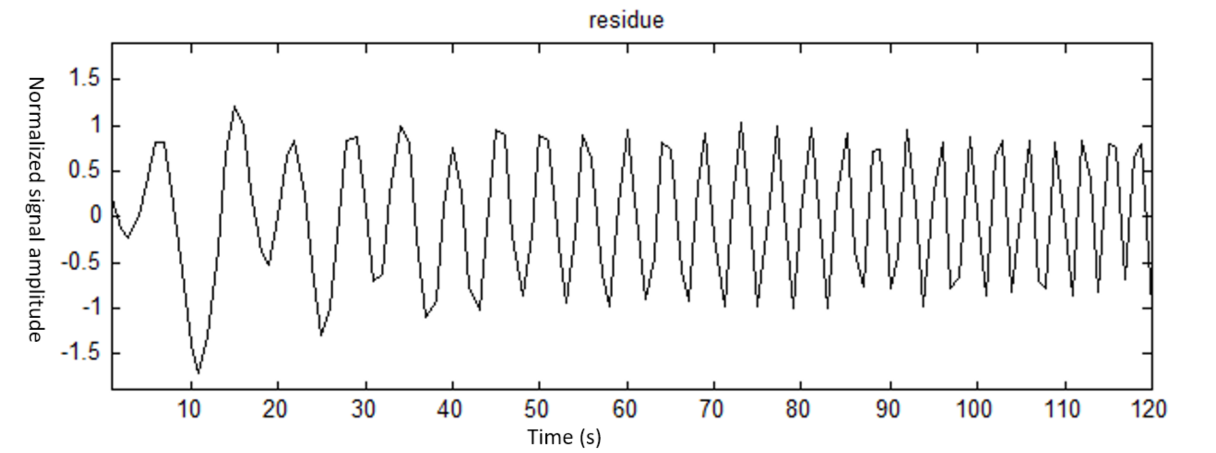

(a) Residue signal

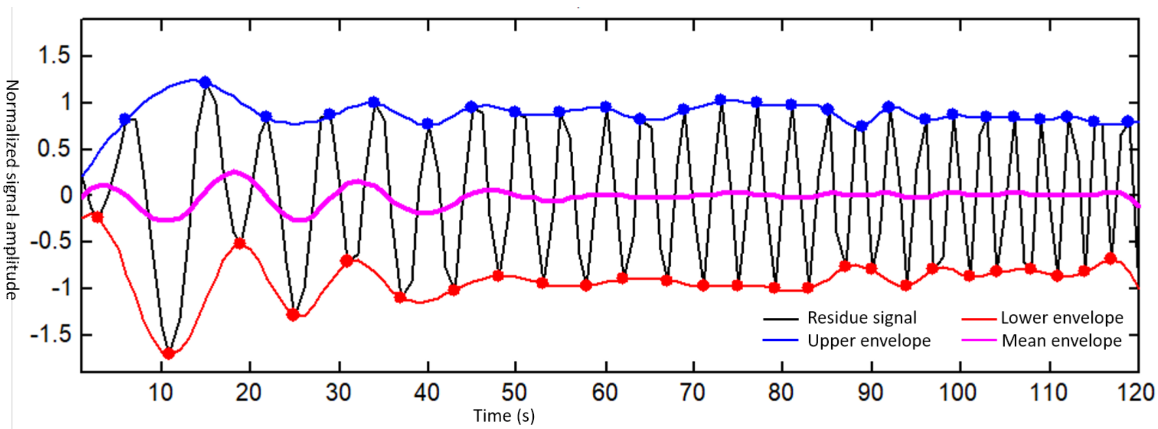

(b) Upper and lower envelopes and their mean

Figure 3.8: The residual signal and its envelops.

- Step 5: Let $s(t) = r_1(t)$ and apply steps 1, 2, 3 and 4 above to determine all the IMFs $imf_2(t)$, $imf_3(t) \cdots$, and residuals $r_2(t)$, $r_3(t) \cdots$. If $r_i(t)$ is is just a monotonic sequence or a constant sequence, the whole decomposition process stops. Finally, the original signal $s(t)$ can be expressed as the sum of several intrinsic mode functions and a residual, namely,

$$s(t) = \sum_{j=1}^{i} imf_j(t) + r_i(t). \tag{3.12}$$

As an example, Fig.3.9 shows a complete EMD of a given signal.

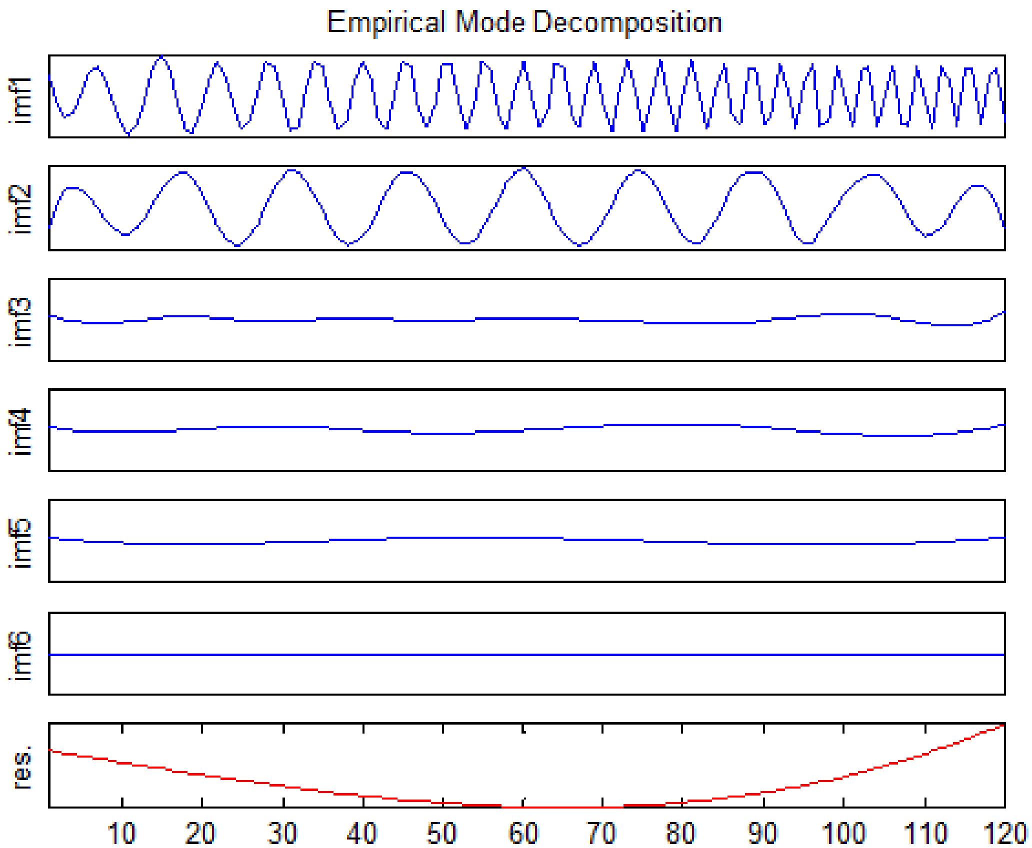

Figure 3.9: IMFs resulting from a complet EMD of a given signal

The flow chart of the EMD algorithm is shown in Fig.3.10.

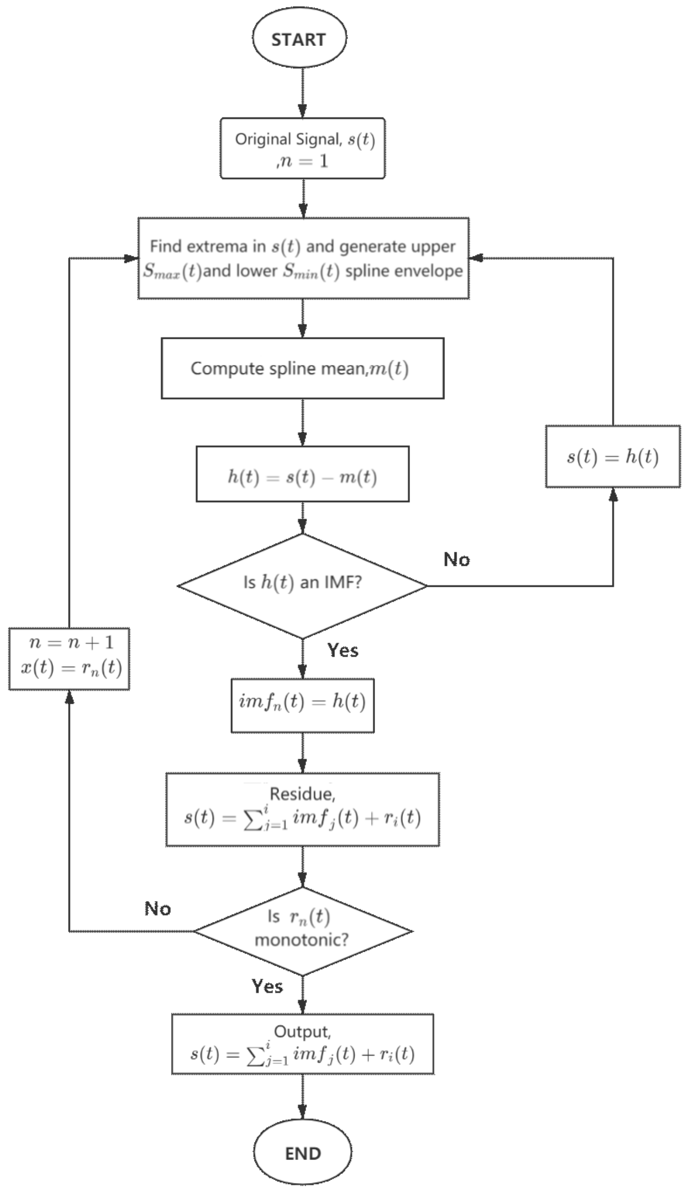

Figure 3.10: The flow chart of EMD algorithm

Having obtained all the IMFs, we now select two of them that are closest to breathing and heartbeat signals. From chapter 2,the frequency range of BR is $0.13 - 0.40Hz$, and the HR is between 0.83 and $1.66Hz$. By computing the partial energy of each IMF during the specified frequency range, we can identify the IMF that is closest to the breathing or heartbeat signal. The partial energies for the breathing and the heartbeat signals are, respectively, calculated by

$$b_i = \frac{\int_{0.13}^{0.4} |F_i(\omega)|^2 \, d\omega}{\int_{-\infty}^{\infty} |F_i(\omega)|^2 \, d\omega} = \frac{E_b(i)}{E(i)} \tag{3.13}$$

$$h_i = \frac{\int_{0.8}^{1.66} |F_i(\omega)|^2 \, d\omega}{\int_{-\infty}^{\infty} |F_i(\omega)|^2 \, d\omega} = \frac{E_h(i)}{E(i)} \tag{3.14}$$

Where $F_i(\omega)$ is the Fourier transform of the $i-th$ IMF, b_i is the normalized partial energy of the $i-th$ IMF during the frequency range of breathing signal and h_i is that of the heartbeat component. Finally, the IMF that takes the maximum partial energy is selected as the breathing or heartbeat signal.

3.2.3 EEMD based breathing and heart sound detection

By using the EMD introduced above, a signal can be decomposed into a number of IMFs and a residual item based on which the vital sign signal is extracted. However, the main problem of EMD is the phenomenon of mode mixing. Although mode mixing has not been strictly defined in the literature, it is known to happen due to the EMD mechanism to extract mono-components from a multi-component signal according to the extremes. Since EMD heaving replies on the local minimas and maximas of the input signal, the presence of intermittent components in the signal would lead to mixed characteristics in one mode function or split of the desired mode into different mode functions.

In 2009, Wu and Huang presented the ensemble empirical mode decomposition (EEMD) to cope with the mode mixing phenomena [79, 78]. In the EEMD method, different white noises were added to the original signal separately, and then the EMD is applied to decompose an "ensemble" of such noisy signals. The EMD components from each noise-added signal will be averaged as the final results of decomposition. Since the corresponding IMFs of different series of noise are unrelated to each other, the noise in each trial can be cancelled out in the ensemble process [78].

In contrast to the EMD, the EEMD is much more robust to noises or interference, which makes it a natural candidate for analyzing signals that inevitably contain time varying noises. The steps of EEMD are decribed below.

- Step1: Add Gaussian white noise $n_i(t)$ to the original signal $x(t)$,yielding

$$x_i(t) = x(t) + n_i(t), (i = 1, 2...., I) \tag{3.15}$$

  where I is the number of signals created by adding noise onto the original signal $x(t)$.

- Step2: Each $x_i(t)$ is fully decomposed by EMD, giving their modes $imf_{k,i}(t)$ where $k = 1, 2, ..., K$.

- Step3: Assign $\overline{imf}_k(t)$ as the $k-th$ mode of $x(t)$, which is obtained as the average of the corresponding $imf_{k,i}(t)$, namely,

$$\overline{imf}_k(t) = \frac{1}{I}\sum_{i=1}^{I} imf_{k,i}(t) \tag{3.16}$$

  After the decomposition of a signal by EEMD, the signal can be finally written as

$$x(t) = \sum_{k=1}^{K} \overline{imf}_k(t) + r_K(t) \tag{3.17}$$

  where $r_K(t)$ is the residual sequence. Similar to the EMD method, among the components decomposed by EEMD, the low-order part bears higher frequency. On the contrary, the high-order mode bears lower frequency component.

The flow chart of EEMD is shown in Fig.3.1

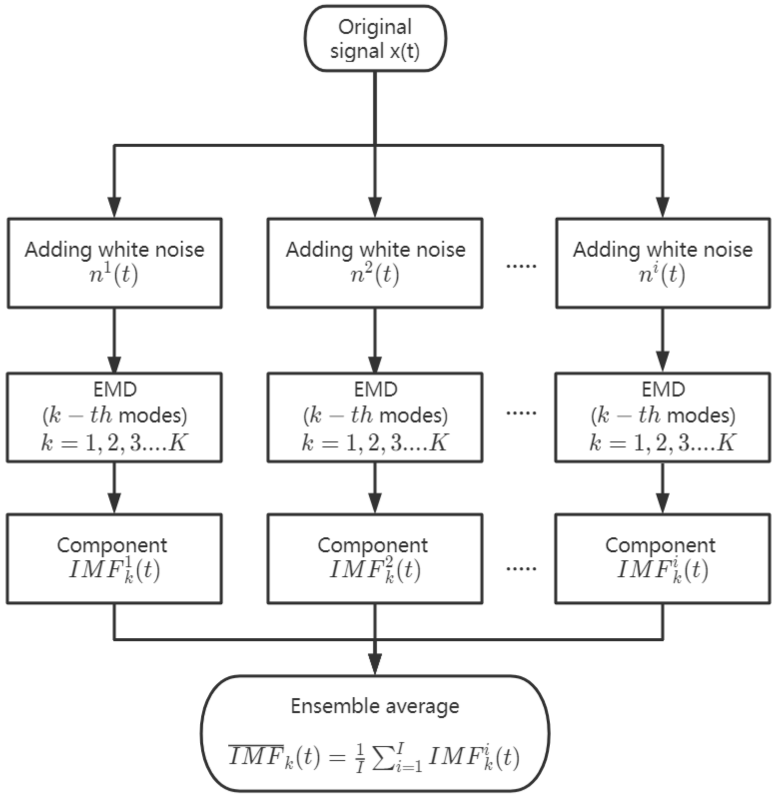

Figure 3.11: EEMD flow chart

Fig 3.12 shows the decomposition results obtained by processing the same echo signal is processed with EMD and EEMD respectively. The component in red is the original signal, which clearly shows the breathing signal, as seen from the wave peaks. Through the EMD and EEMD of the signal, we can see that the respiratory signal appears modal aliasing, that is, the respiratory signal is separated into $IMF5$ and $IMF6$ (orange circle). In contrast, the breathing signal resulting from the EEMD algorithm is consistently and accurately, shown in $IMF6$.

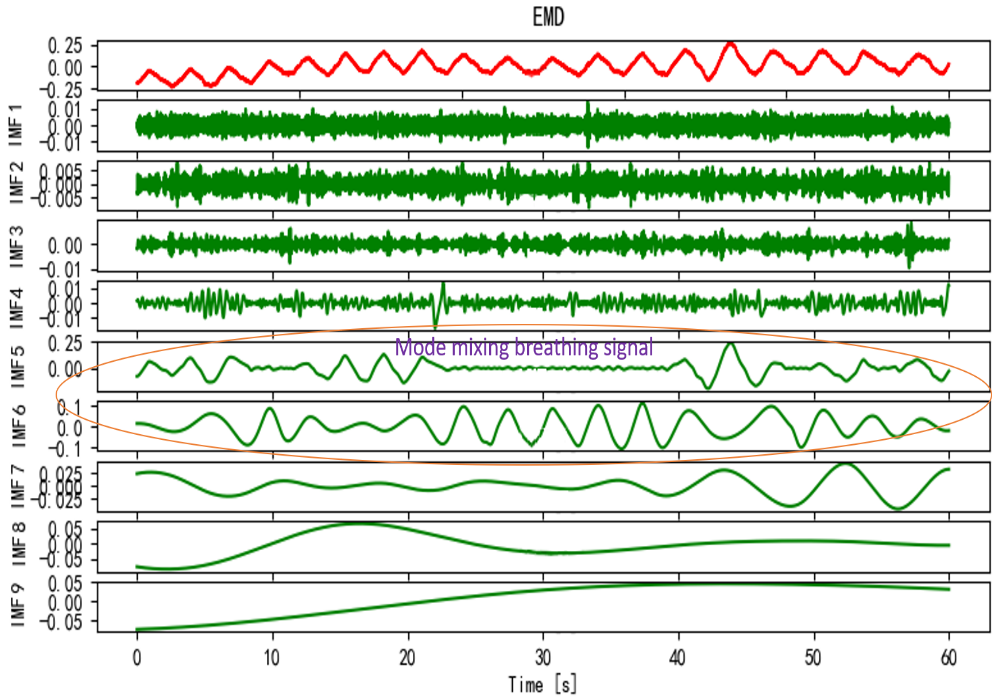

(a) EMD

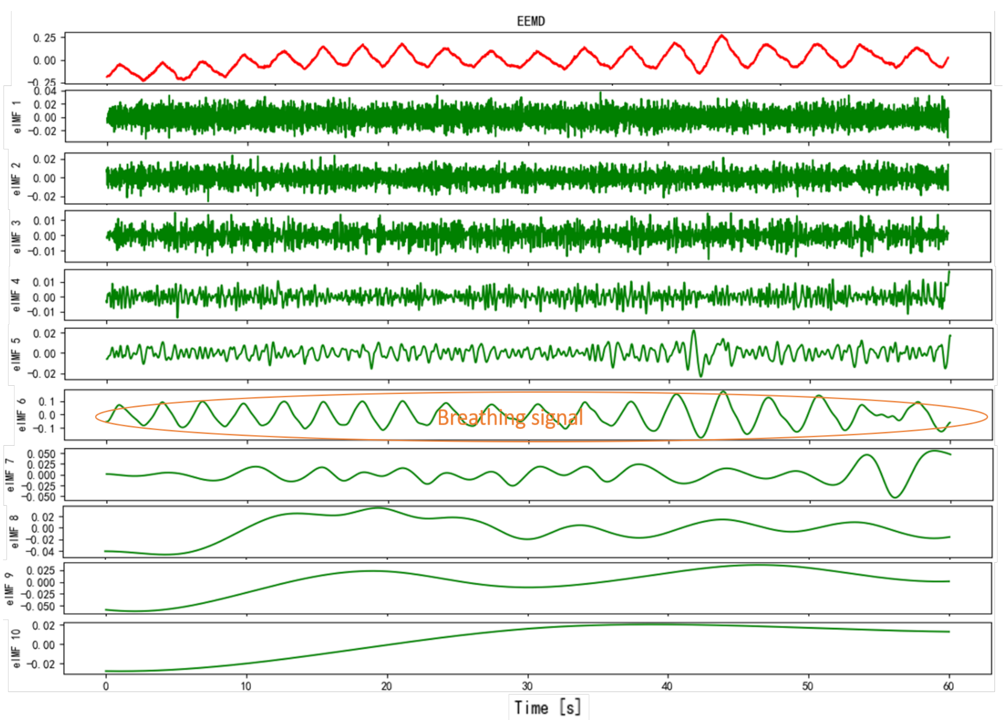

(b) EEMD

Figure 3.12: Comparison EMD and EEMD results

3.2.4 VMD based breathing and heart sound detection

variational mode decomposition (VMD) algorithm is an entirely non-recursive method, whose modes, extracted concurrently, constitute a nice partition of the input spectrum, with each mode being clearly dominant around the signal, and it is capable of capturing the relevant center frequencies quite precisely [16]. This algorithm is much more robust to noise. In this section, we use VMD algorithm to track the vital signs of multiple targets.

The VMD algorithm begins with the computation of the Fouier transform $\hat{f}(\omega)$ of the preprocessed echo signal $f(t)$, and then determines the mode function in the frequency domain in an iterative manner. At the $(n+1)th$ iteration, the Fouier transform of the $k-th$ mode function $u_k(t)$ is computed by [16]

$$\hat{u}_k^{n+1}(\omega) = \frac{\hat{f}(\omega) - \sum_{i=1,i\neq k}^{K} \hat{u}_i^n(\omega) + \frac{\hat{\lambda}^n(\omega)}{2}}{1 + 2\alpha\left(\omega - \omega_k^n\right)^2} \tag{3.18}$$

where $\hat{u}_i^n(\omega)$ is the Fourier transform of the of $i-th$ mode function obtained at the $n-th$ iteration, ω_k^n is the center frequency of the $k-th$ mode function, which is computed by

$$\omega_k^{n+1} = \frac{\int_0^\infty \omega \left|\hat{u}_k(\omega)\right|^2 d\omega}{\int_0^\infty \left|\hat{u}_k(\omega)\right|^2 d\omega}, \tag{3.19}$$

and $\lambda^n(\omega)$ is the frequency domain Lagrangian multiplier used to enforce exact reconstruction of the input signal [16], which is updated as follows,

$$\hat{\lambda}^{n+1}(\omega) \leftarrow \hat{\lambda}^n(\omega) + \tau\left[\hat{f}(\omega) - \sum_k \hat{u}_k^{n+1}(\omega)\right] \tag{3.20}$$

where τ is the update parameter of the Lagrangian multiplier. In equation 3.18, α is a parameter to control the data-fidelity constraint. The termination criterion for the iteration of $\hat{u}_k(\omega)$ is set as

$$\sum_k \frac{\left\|\hat{u}_k^{n+1} - \hat{u}_k^n\right\|_2^2}{\left\|\hat{u}_k^n\right\|_2^2} < \varepsilon \tag{3.21}$$

where ε is the tolerance of the total relative error of all the mode functions at the $n-th$ iteration (typically around 10^{-6}) and $\hat{u}_k^n$ is a vector representation of $\hat{u}_k^n(\omega)$ for notational convenience. Upon convergence, the VMD algorithm outputs the FT of K mode functions and their center frequencies. After performing the inverse FT, we obtain the time-domain mode function $u_k(t)$, $k = 1, 2, \cdots, K$. The flowchart for the VMD algorithm is shown in Fig.3.13. It is to be noted that the total number of mode functions K in the VMD algorithm is a pre-scribed parameter, which is determined based on the desired modes in the decomposition. In this work, we focus on $K = 3$ or 4 as we are mainly concerned about the breathing and heart sound signals.

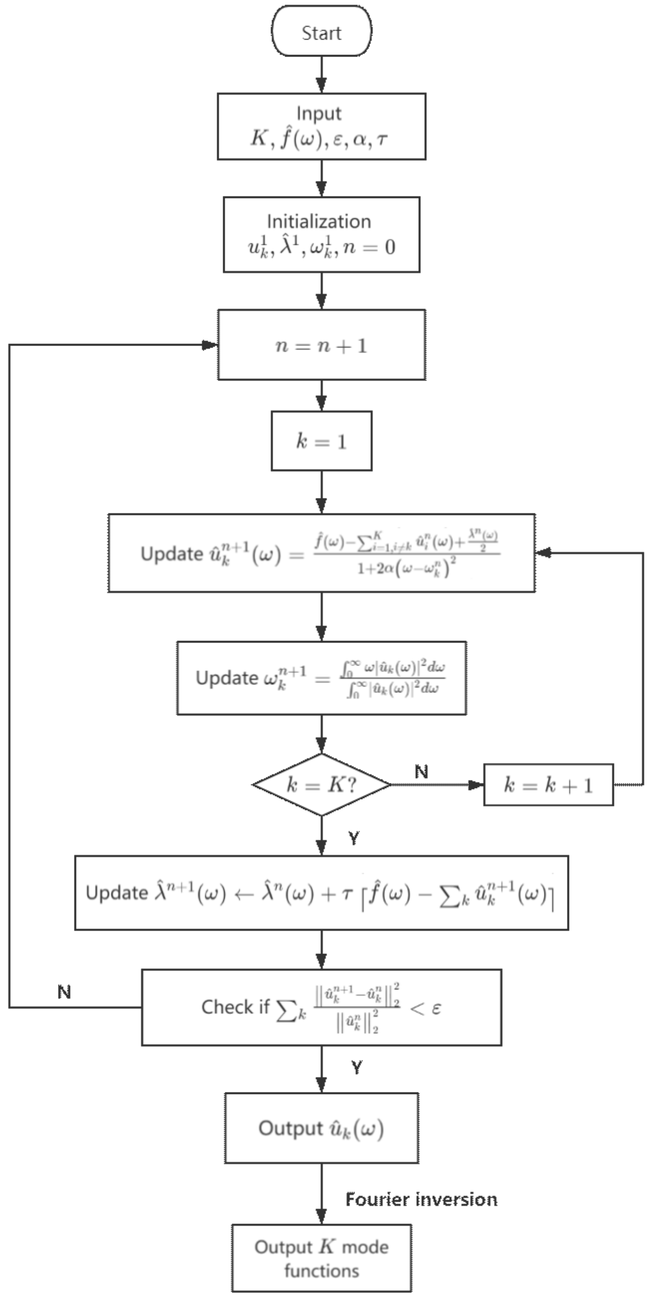

Figure 3.13: Flow chart of the VMD algorithm

Chapter 4

Experimental Results

This chapter carries out extensive experimental studies to evaluate the four algorithms introduced in the previous chapter. We consider two main scenarios in our experimentation: single target detection and double target detection. In the single-target experimentation, we will estimate the BR and HR of the person when he is located at different distances from the radar. We will also investigate the estimation error rate when the person has different sitting positions and compare the estimation results from different persons.

In the case of double-target estimation, we will test two situations, i.e., (i) when the two targets are located at different distances to the radar, and (ii) when they appear at almost the same location. The second scenario is the limiting case of the first situation and imposes a great challenge to the four estimation methods.

4.1 Single Target Estimation

4.1.1 Baseline setup of single target

Here we first consider a simple setup, where the target faces the radar at a distance of 70 cm or 250 cm. We arrange two persons for this test in order to show the discrepancy of the BR and HR estimation results among different persons considering that the radar echo reflected by different persons could be different. To measure the estimation error rate of the four algorithms, we use the Electrocardiogram (ECG) measurement as ground truth for the heart rate (number of beats per minute). The chest strap type of ECG is utilized in this project as illustrated in Fig.4.5. In the meantime, we use video recording to observe the breathing of the testee to get the ground truth of BR.

Figure 4.1: Chest strap type ECG

The estimation error of the HR and BR is defined as [85]

$$e_c = \left(\frac{|T - T_0|}{T_0} \right) \times 100\% \tag{4.1}$$

where T is the number of heartbeats or breaths obtained by the four algorithms, and T_0 is the ground truth of the breath or heart rate.

At distance of 70 cm:

As shown in Fig.4.2, the testee is required to stay as stationary as possible during the experiment to reduce irrelevant movements such as body shaking. The left picture shows the object is located 70 cm away from the radar and the right one shows the object is 250 cm away from the radar. Then, Fig.4.3 shows the BR estimation results of the four algorithms for object 1 at 70 cm to the radar. According to the figures, we can see that the FFT+BPF, EEMD, VMD give an accurate estimation as compared with the ground truth 12 i.e., breaths per minute of the objects and the EMD only got 10 breaths per minute because of mode mixing.

Figure 4.2: Single target HR and BR experiment scenario

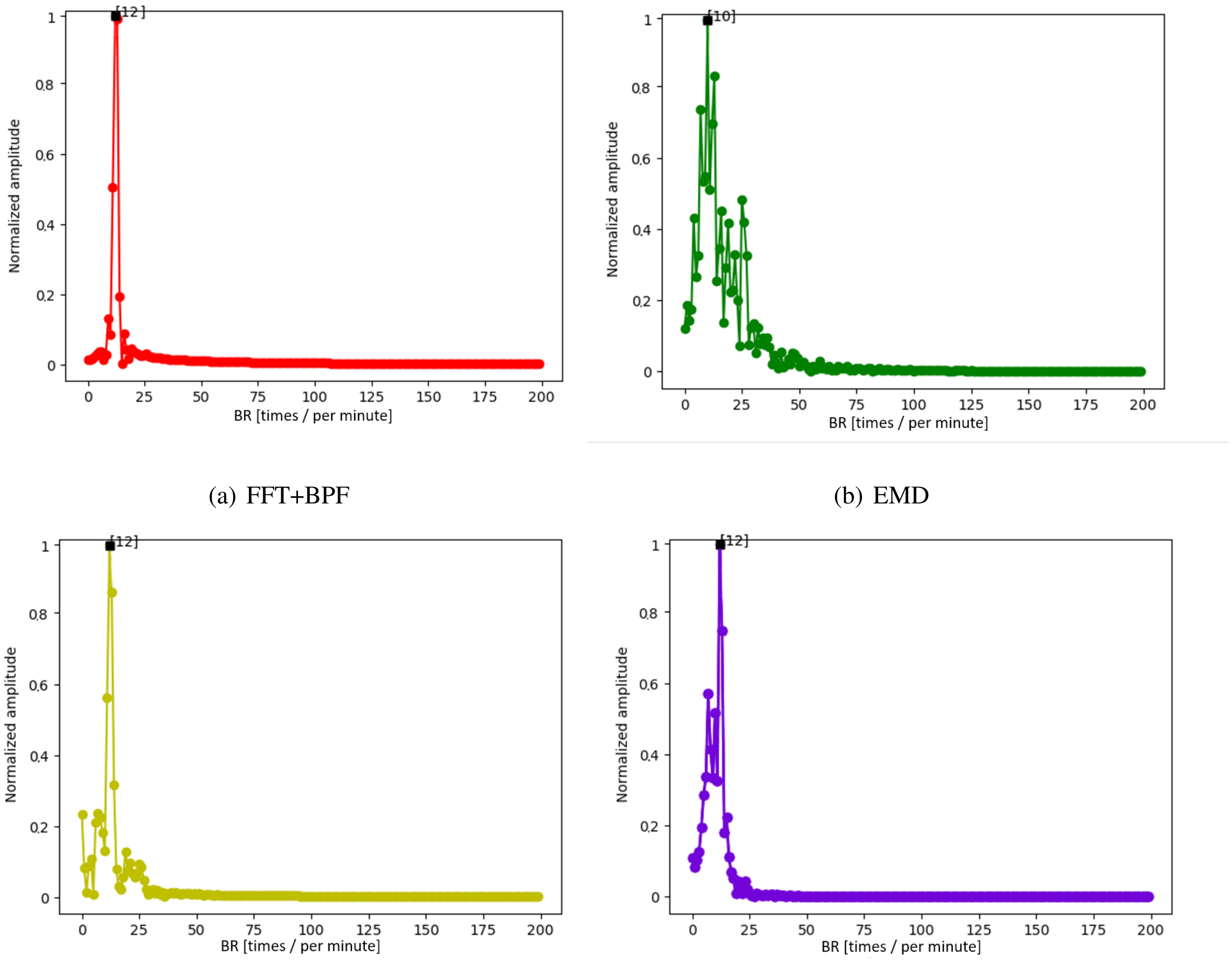

(a) FFT+BPF (b) EMD

(c) EEMD (d) VMD

Figure 4.3: BR estimation results for object 1 at 70 cm

Fig.4.4 shows the HR estimation results of the four algorithms for the same object. By comparing with the ground truth reported by the ECG device as shown in Fig.4.5, we can see that the FFT+BPF, EEMD and VMD give similar and relatively accurate estimations whereas EMD provided a poor estimation. It is of interest to see that the FFT+BPF and EEMD gave the same estimation result.

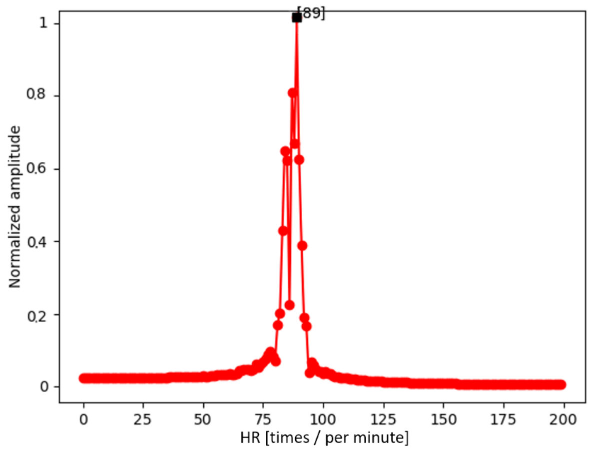

(a) BP

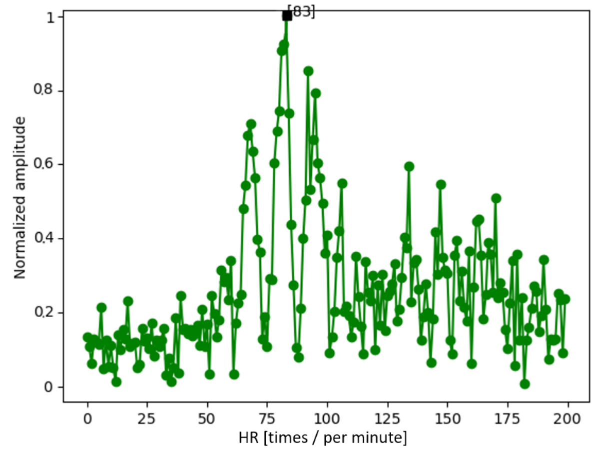

(b) EMD

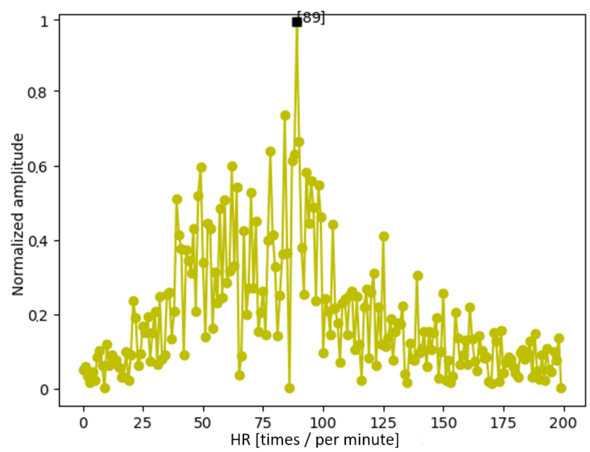

(c) EEMD

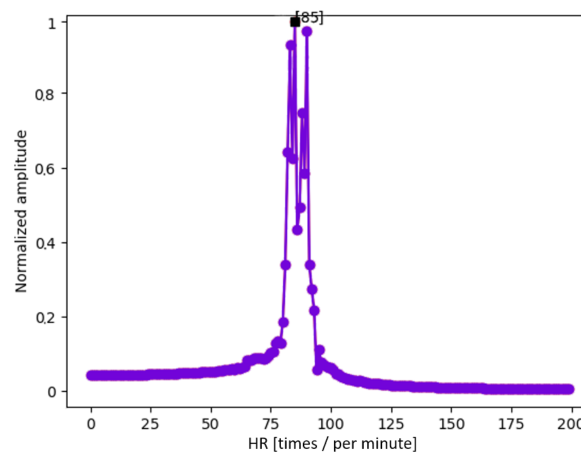

(d) VMD

Figure 4.4: HR estimation results for object 1 at 70 cm

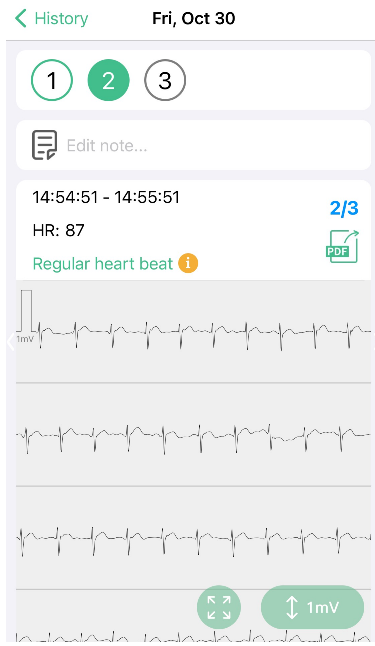

Figure 4.5: HR reported by ECG for object 1 at 70 cm

Now we repeat the same experiment for object 2 for the estimation of BR and HR. Fig.4.6 gives the BR estimation results from the four algorithms. Similar to the first experiment for object 1, the FFT+BPF, EEMD and VMD methods led to the same result and exactly match with the ground truth 19. Fig.4.7 gives the estimation results for the HR of object 2 obtained from the four algorithms. In contrast to the ground truth HR shown in Fig.4.8, all of the four algorithms gave accurate estimation with an error rate of $\leq 10\%$. Table 4.1 summarises the estimation result from the four methods for the two objects located at 70 cm from the radar.

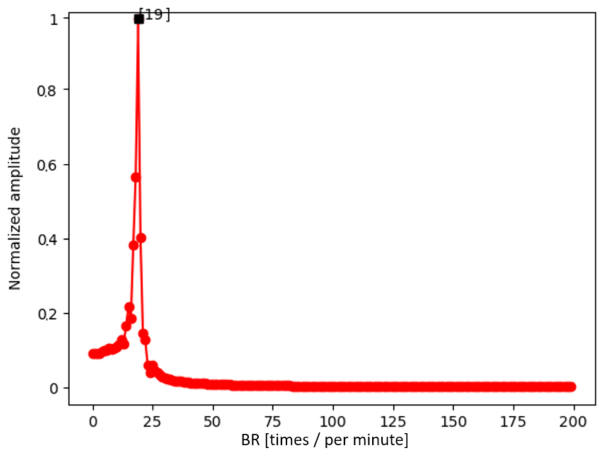

(a) FFT+BPF

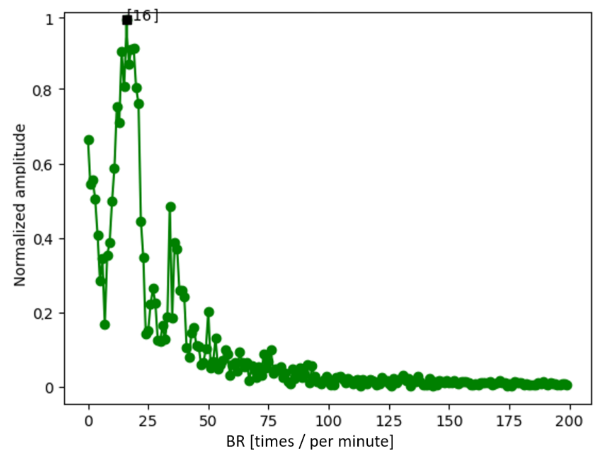

(b) EMD

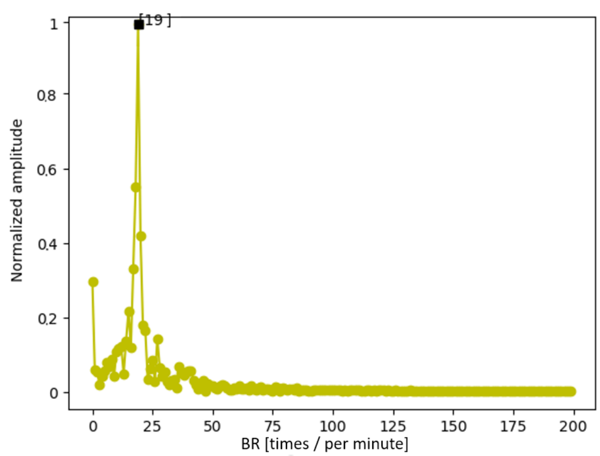

(c) EEMD

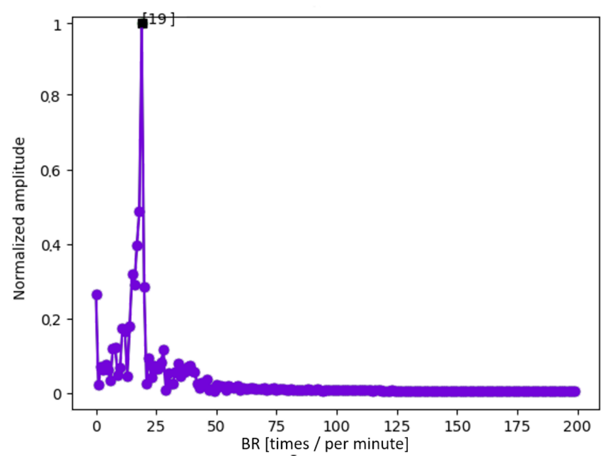

(d) VMD

Figure 4.6: BR estimation results for object 2 at 70 cm

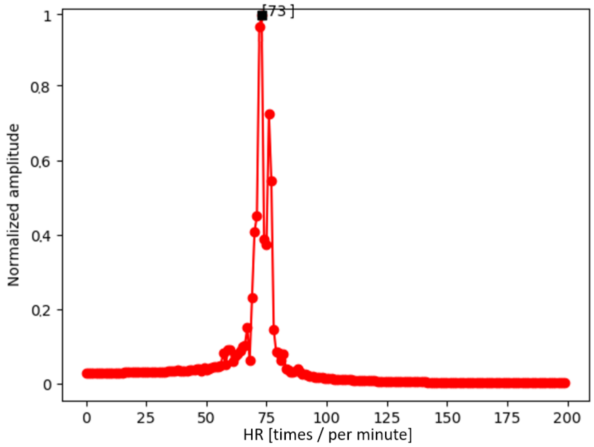

(a) BP

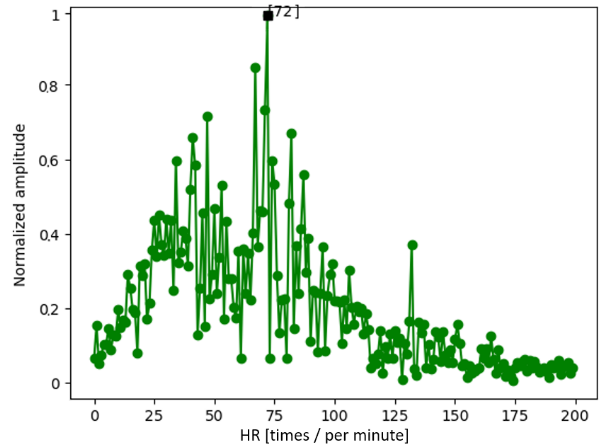

(b) EMD

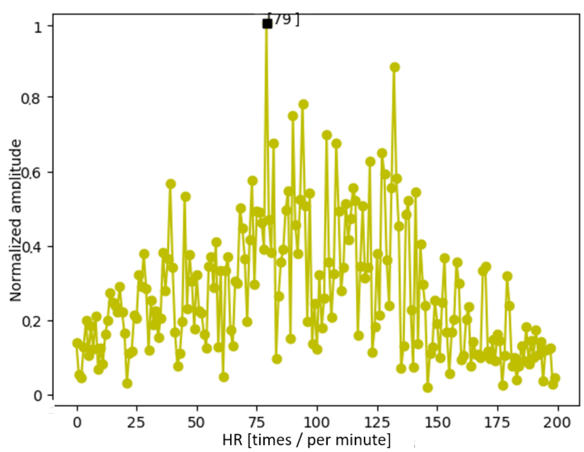

(c) EEMD

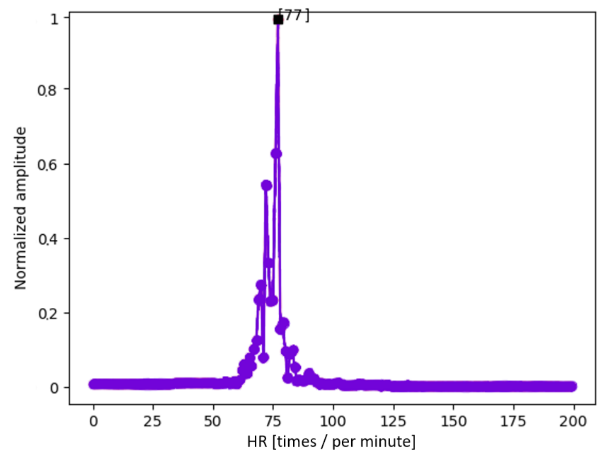

(d) VMD

Figure 4.7: HR estimation results for object 2 at 70 cm

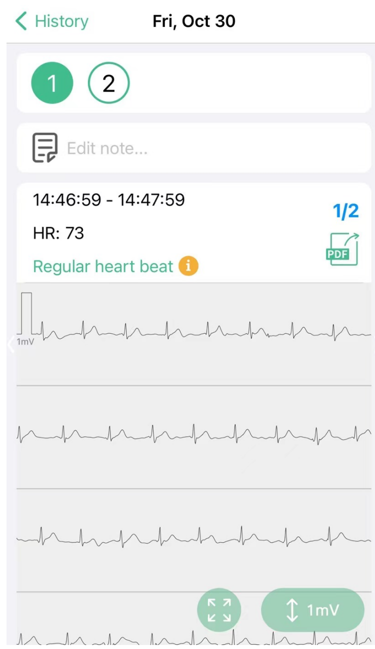

Figure 4.8: HR reported by ECG for object 2 at 70 cm

Table 4.1: BR and HR estimation results from four algorithms for the two objects at 70 cm

	Breathing					Heartbeats				
	FFT+BPF	EMD	EEMD	VMD	Reported	FFT+BPF	EMD	EEMD	VMD	ECG
Object1	12	10	12	12	12	89	83	89	85	87
Error rate	0.0%	16.7%	0.0%	0.0%		3.3%	4.6%	2.3%	2.3%	
Object2	19	16	19	19	19	73	72	79	77	73
Error rate	0.0%	18.2%	0.0%	0.0%		0.0%	1.4%	8.2%	5.5%	

At distance of 250 cm:

Next, we repeat the same experiment for the two objects individually by increasing the distance to the radar to 250 cm and then compare the estimation results from the four algorithms with the BR and HR ground truths. The BR and HR estimation results of object1 and object2 are shown in Fig.4.9, 4.10, 4.11, and 4.12, respectively. For the sake of comparison, Fig.4.13 gives the HR results measured by ECG for the two objects.

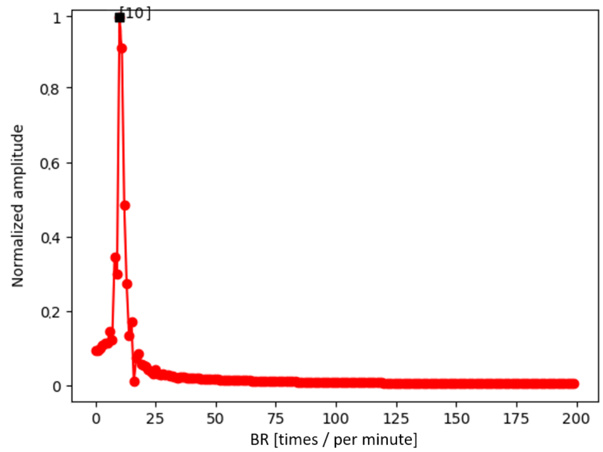

(a) FFT+BPF

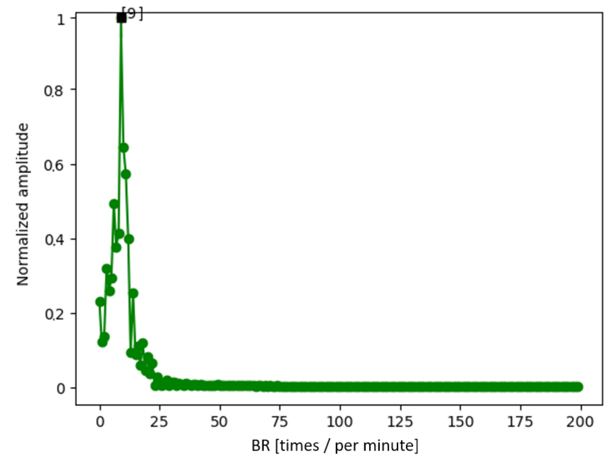

(b) EMD

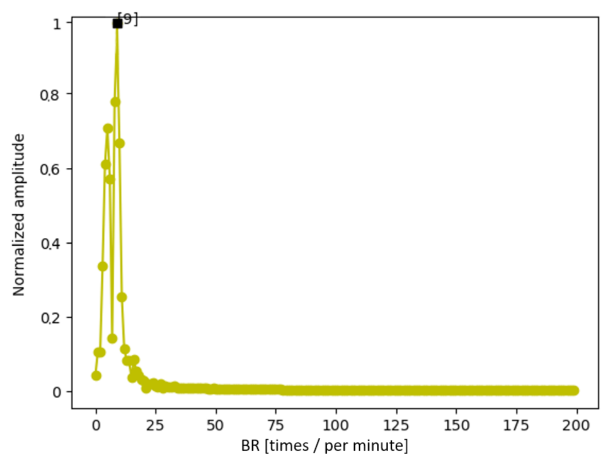

(c) EEMD

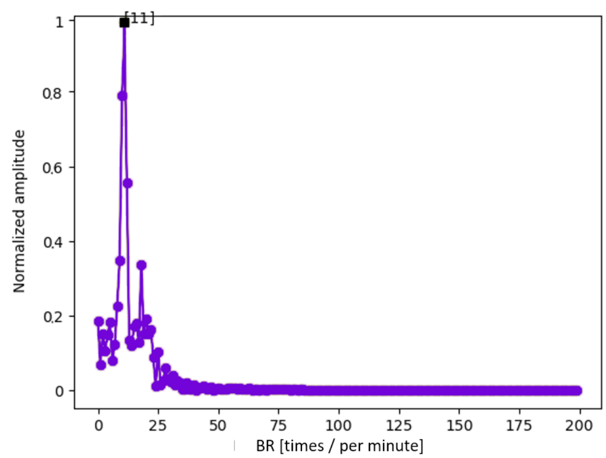

(d) VMD

Figure 4.9: BR estimation results for the object 1 at 250 cm

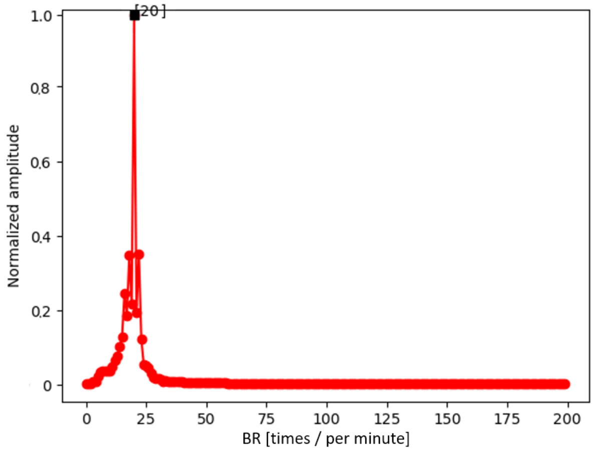

(a) FFT+BPF

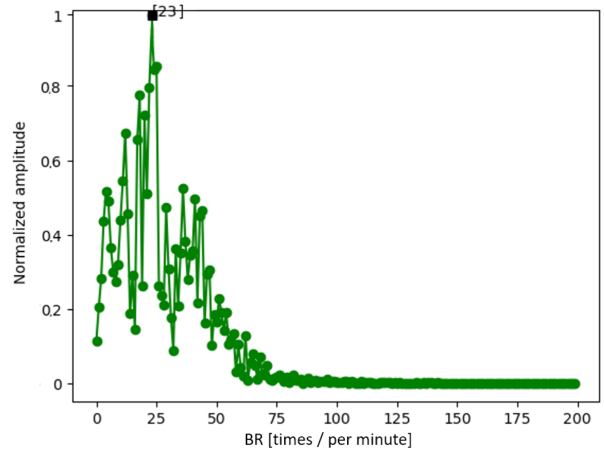

(b) EMD

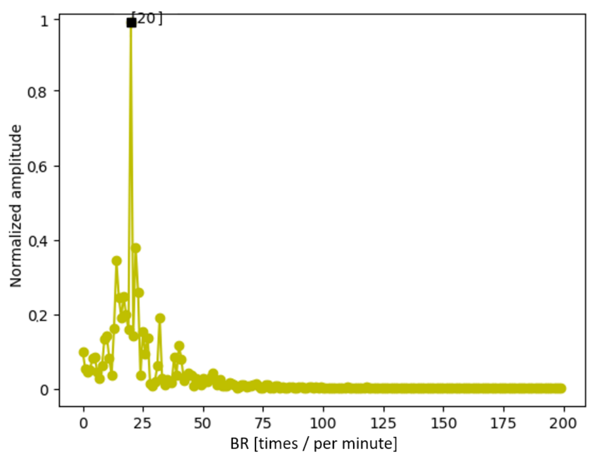

(c) EEMD

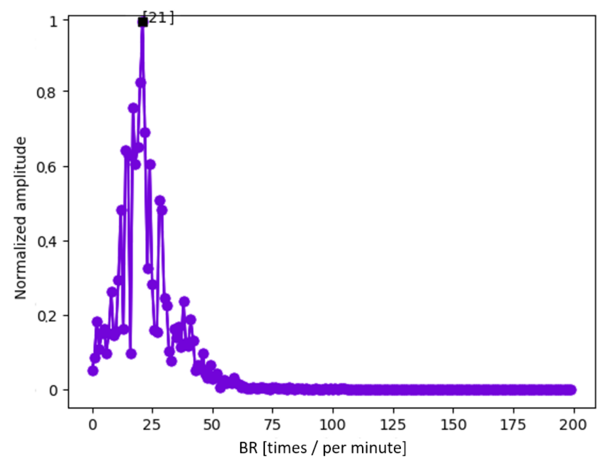

(d) VMD

Figure 4.10: BR estimation results for object 2 at 250 cm

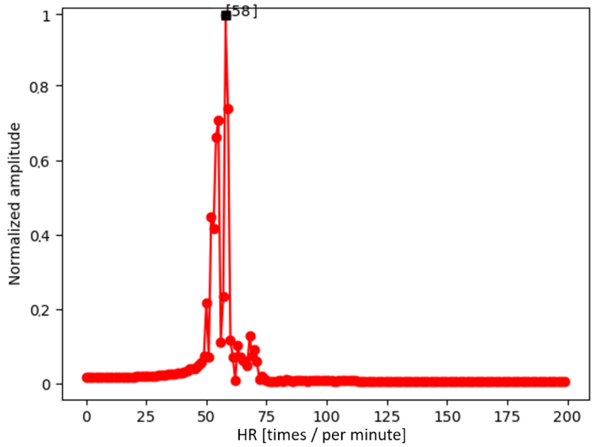

(a) FFT+BPF

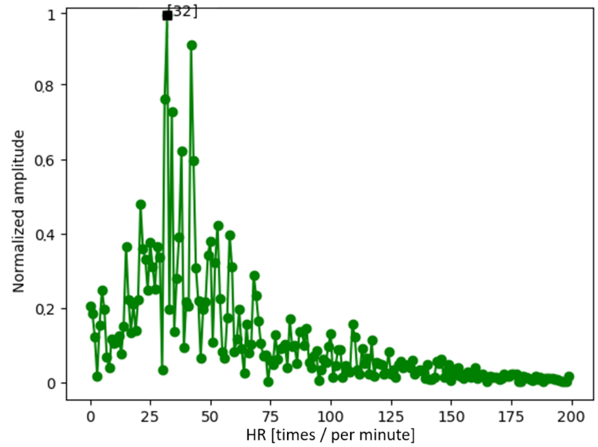

(b) EMD

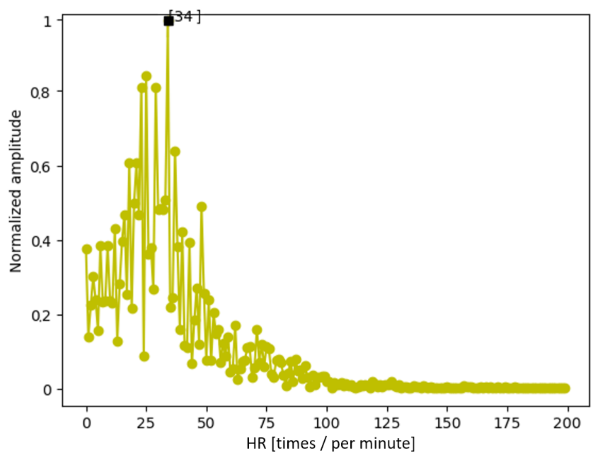

(c) EEMD

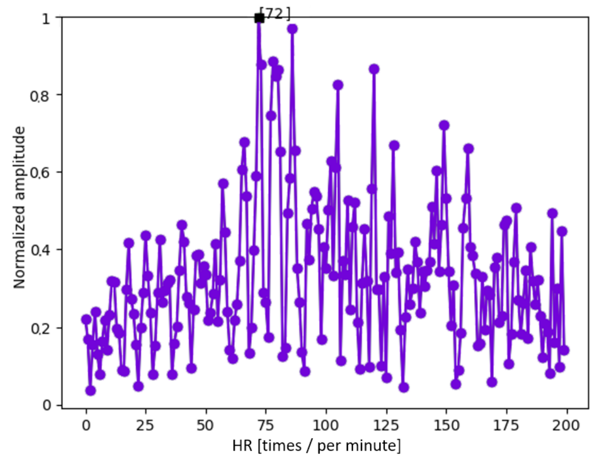

(d) VMD

Figure 4.11: HR estimation results for object 1 at 250 cm

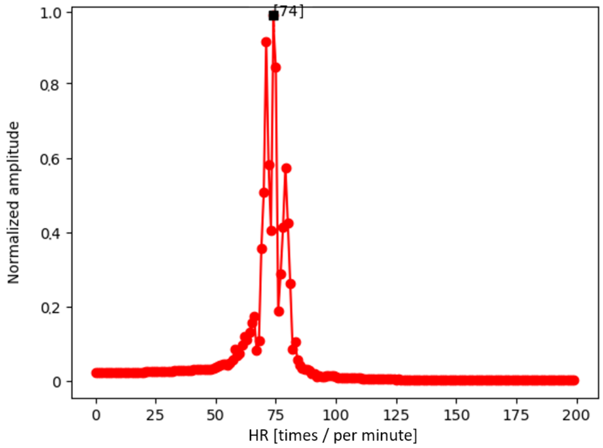

(a) FFT+BPF

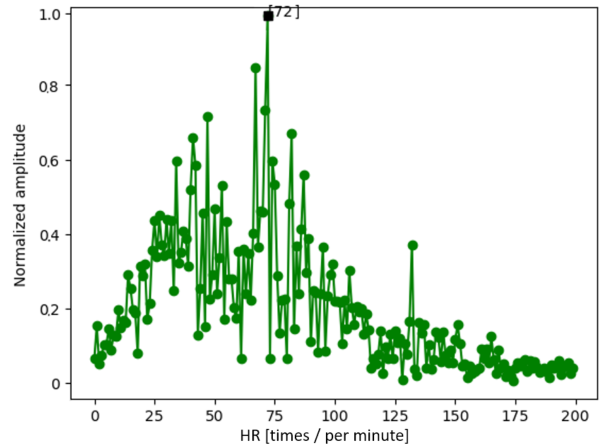

(b) EMD

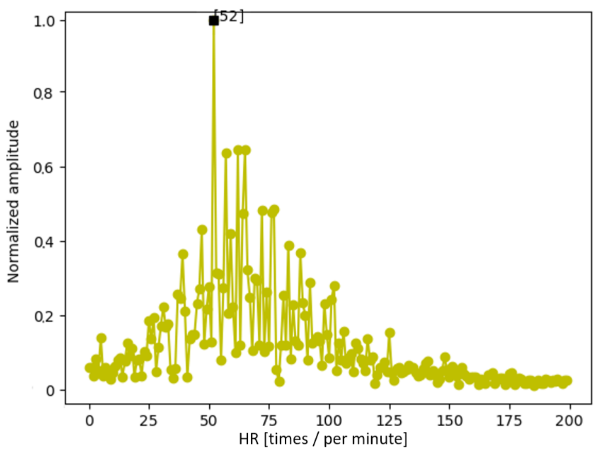

(c) EEMD

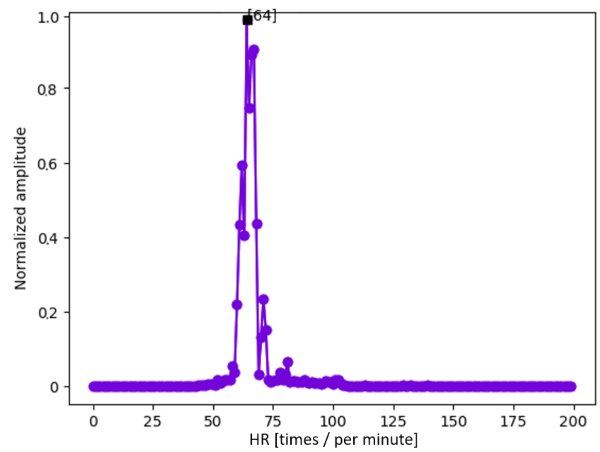

(d) VMD

Figure 4.12: HR estimation results for object 2 at 250 cm

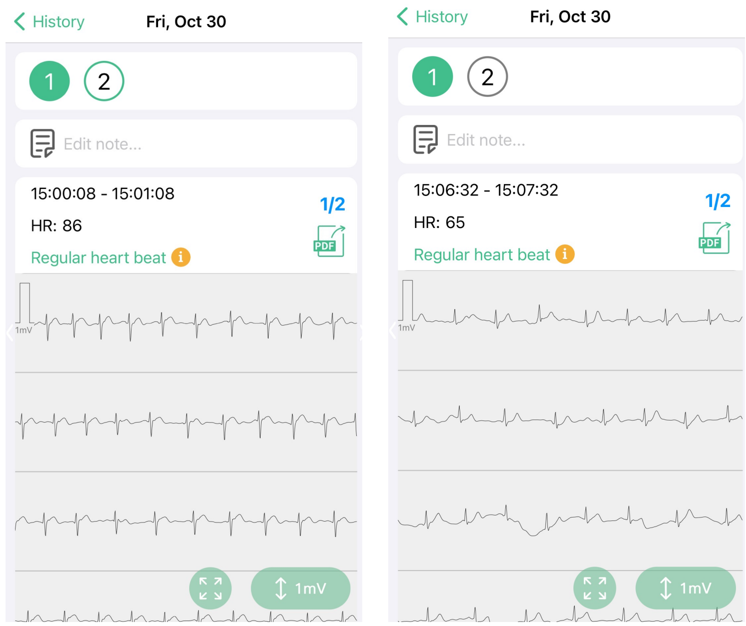

(a) Object 1 HR (b) Object 2 HR

Figure 4.13: HR reported by ECG for two objects at 250 cm

Table 4.2: BR and HR estimation results from four algorithms for the two objects at 250 cm

	Breathing					Heartbeats				
	FFT+BPF	EMD	EEMD	VMD	Reported	FFT+BPF	EMD	EEMD	VMD	ECG
Target1	10	9	9	11	10	58	32	34	72	86
Error rate	0.0%	10.0%	10.0%	10.0%		32.6%	62.8%	60.5%	16.3%	
Target2	20	23	20	21	20	74	72	52	64	65
Error rate	0.0%	19.2%	0.0%	5.0%		13.9%	10.8%	20.0%	1.6%	

Table 4.2 lists together with the ground truth the BR and HR of the two objects at 250 cm, estimated by the four algorithms. From our extensive experimental studies, we have found that even if the distance between the object and radar exceeds 200 cm, like 250 cm, the FFT+BPF, EEMD and VMD algorithms can estimate the BR accurately while the EMD method failed to give accurate BR estimation possibly due to the mode mixing issue of the algorithm. In the case of HR estimation, only VMD works well at the distance exceeding 200 cm. Unfortunately, all other methods could not yield a satisfactory estimation error rate.

4.1.2 Challenging setup of single target

In this sub-section, we conduct several experiments to estimate the BR of the target in more challenging situations. In the first setting, the person remains side sitting against the radar. Other situations involve deep breathing, changing breath frequency purposely and holding breath by the object. In all the experiments, the target is located at 3 meters from the radar. In this section, we pay more attention to the breathing signals detected by the algorithms since these signals are not the typical breathing detected by the radar when the testee is facing the radar.

As shown in Fig.4.14, the object keeps side sitting in the front of the radar with a distance of 3 meters. Fig.4.3 shows the original radar echo (after preprocessing) along with the breathing signals extracted by the four algorithms. The top figure in Fig.4.3 exhibits a body shake as indicated by the large variation in the waveform amplitude. Due to this body shaking, the FFT+BPF is not able to extract the respiration signal. Meanwhile, the EMD and EEMD algorithms also failed to detect the breathing waveform. The last three subfigures are produced by the VMD method when K is set as 3. The third figure in this group represents the respiration signal, implying that only VMD can estimate the BR in this setting of target estimation. Table 4.3 summarises the BR values estimated by the four algorithms.

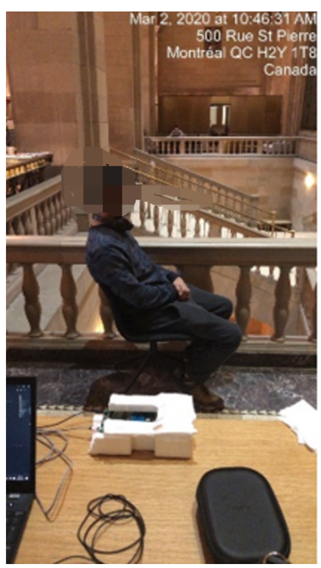

Figure 4.14: Side-sitting experiment

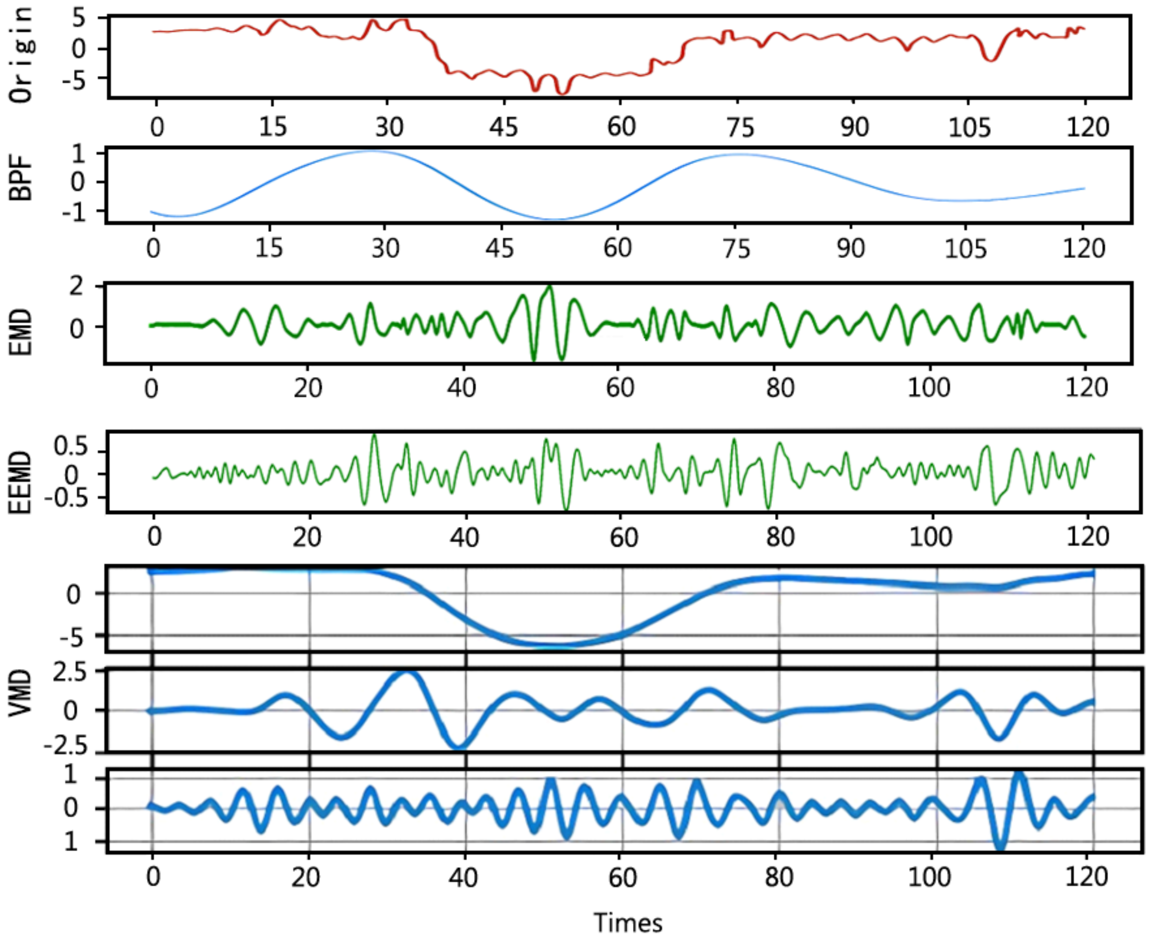

Figure 4.15: Breathing signal detected under side-sitting

Table 4.3: BR estimation results from four algorithms in side-sitting experiment

	Breathing (two minutes)				
	FFT+BPF	EMD	EEMD	VMD	Reported
Testee	2	30	32	26	25
Error rate	92.0%	20.0%	28.0%	4.0%	

In the second setup of this experiment, we ask the same testee to take deep breaths for a one-minute duration when facing the radar. Fig.4.16 illustrates the input preprocessed radar echo plus the waveforms estimated by the four algorithms. Interestingly, all the algorithms can extract well

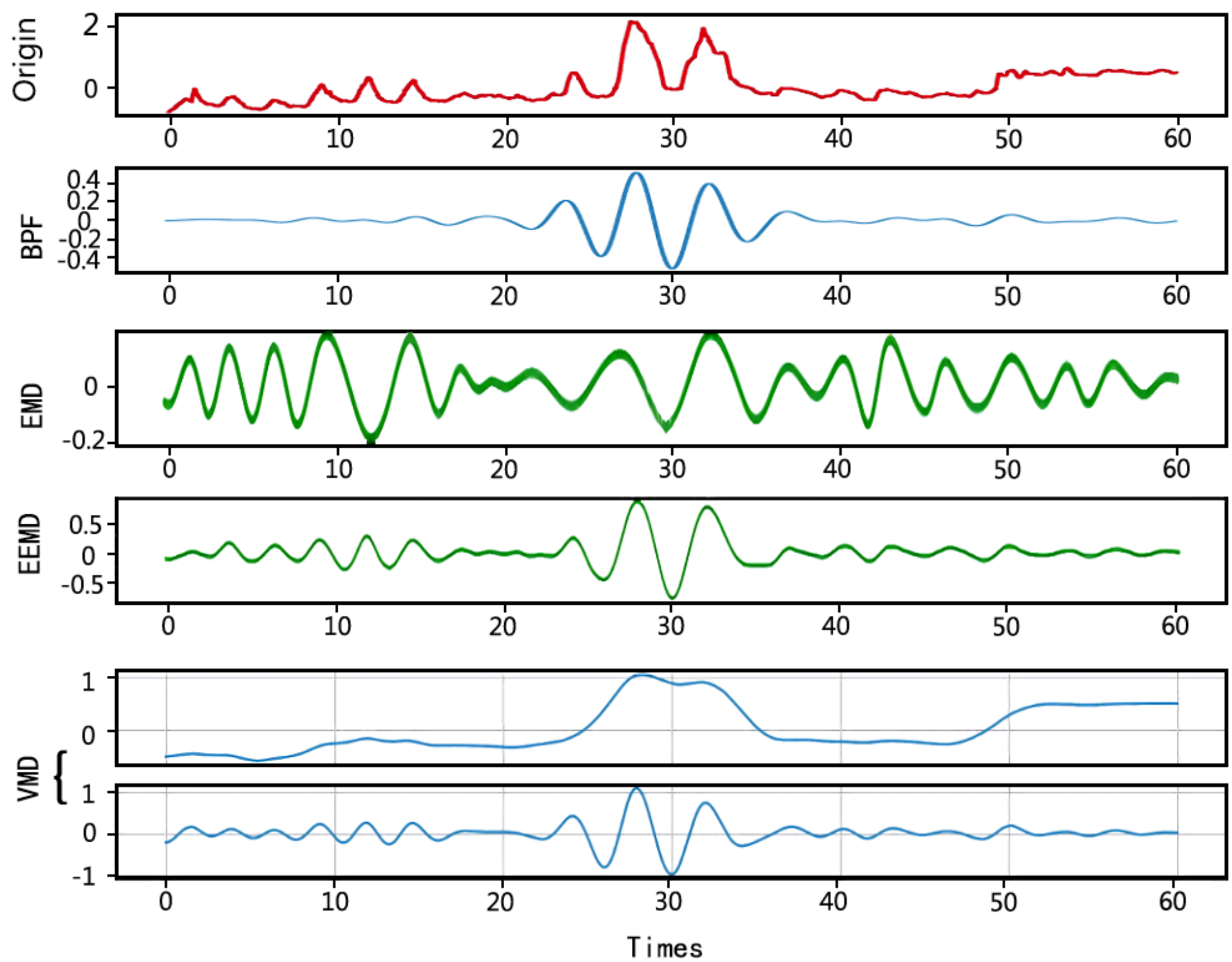

Figure 4.16: Deep breath experiment

the breathing signal. Among them, the FFT+BPF algorithm omitted the first half of the respiratory signal as a result of too small normalized amplitude. The EMD algorithm automatically increases the number of breaths in the second half. In contrast, the EEMD and VMD algorithms provide more accurate estimation results. Table 4.4 shows the BR estimation results together with the reported ground truth.

Table 4.4: BR estimation results from four algorithms for deep breathing experiment

	Breathing (one minute)				
	FFT+BPF	EMD	EEMD	VMD	Reported
Testee	11	14	13	13	13
Error rate	23.1%	7.7%	0.0%	0.0%	

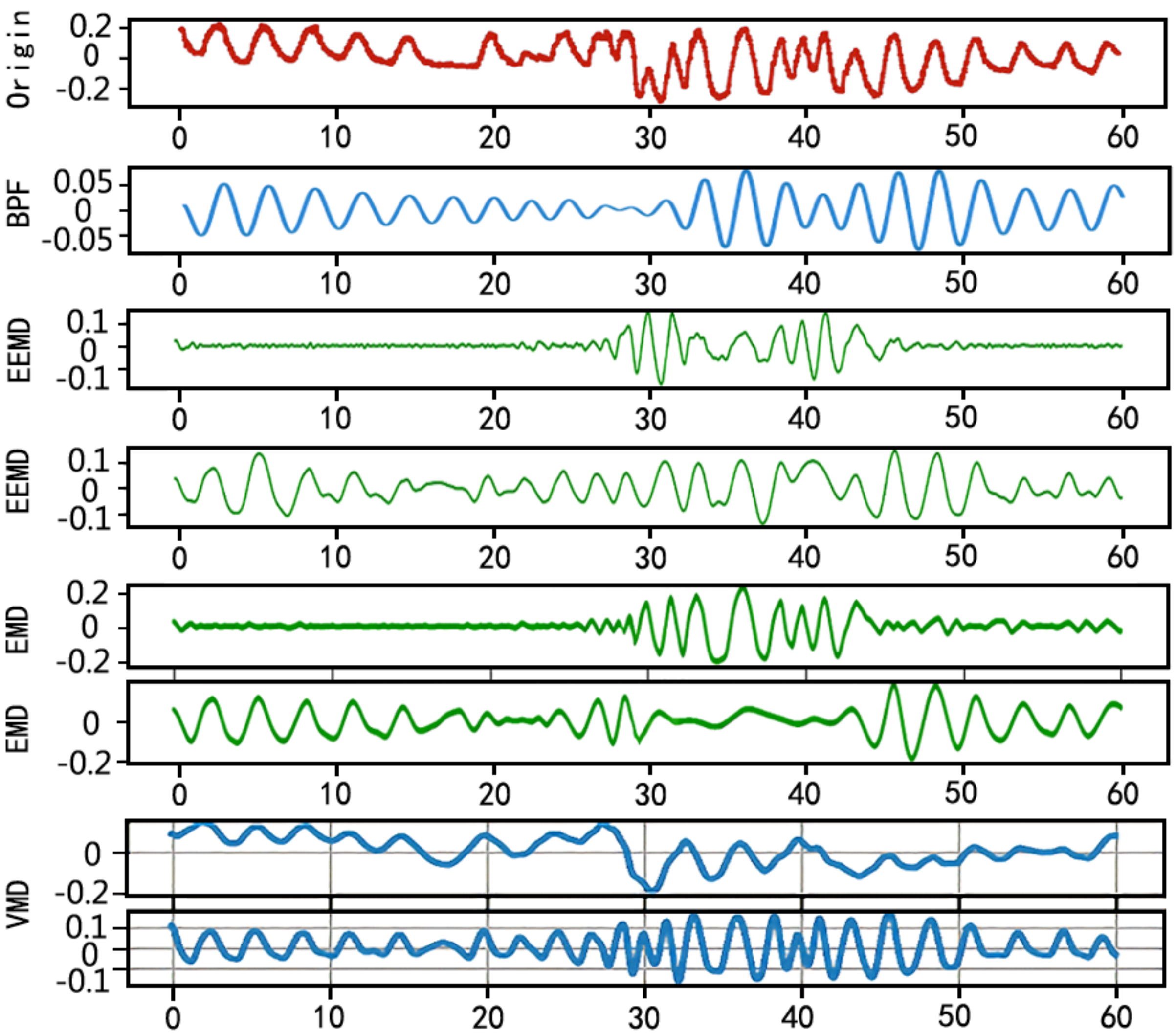

Figure 4.17: Breathing frequency change experiment

Fig.4.17 shows the relevant waveforms estimated by the four algorithms when the testee changes the frequency of breathing. From the results, we can see that EMD algorithm makes large errors during most of the test period. The EEMD algorithm eliminated most of the mode mixing by adding white noise, and thus significantly improved the EMD algorithm. In general, the FFT+BPF and VMD algorithms are able to detect the breathing signal in this challenging setting. The BR estimation results obtained by the four algorithms are listed in Table 4.5.

Table 4.5: BR estimation results from four algorithms for the breathing frequency change experiment

	Breathing (one minute)				
	FFT+BPF	EMD	EEMD	VMD	Reported
Testee	23	16	22	24	24
Error rate	4.2%	33.3%	8.3%	0.0%	

Finally, Fig. 4.18 shows the estimated breathing signals resulting from the four algorithms when the testee holds breath.

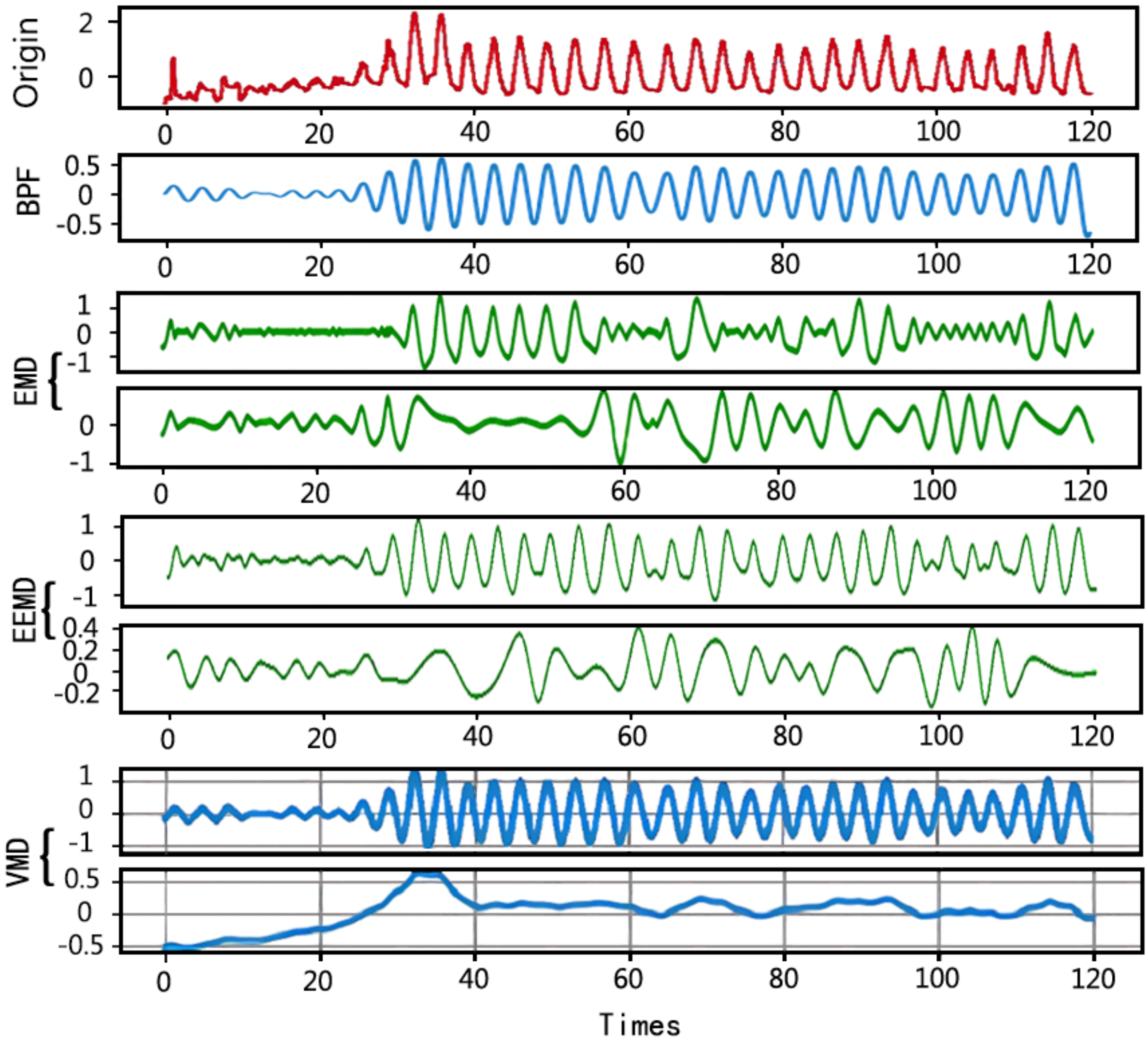

Figure 4.18: Hold the breathing experiment

Apparently, the EMD algorithm once again fits only a part of the true breathing signal. This is mainly because the weak exhalation signal and heartbeat signal are mixed up even though breath is held. As seen from the figure, the FFT+BPF, EMD, and VMD algorithms all show a low error rate, indicating that holding breath has no effect on these three algorithms. What is more interesting is that the VMD algorithm also separates the micro-motion curve of the human body (the last line). In contrast, the EMD algorithm once again gives mode mixing so that the number of breaths is lost compared with the ground truth. Table 4.6 shows the error rate.

Table 4.6: BR estimation results from four algorithms for holding the breathing experiment

	Breathing (two minutes)				
	FFT+BPF	EMD	EEMD	VMD	Reported
Testee	27	18	27	27	27
Error rate	0.0%	33.3%	0.0%	0.0%	

It is worth-mentioning that several researchers [68], [68], and [69] UWB radar with the aforementioned four algorithms to detect the BR and HR of one or two persons sitting in a car. The radar is mounted on the top of the windshield within the car. The driver and a passenger sit facing the radar. Table 4.7 shows the HR and BR estimation results reported in the literature. Note that these authors did not apply preprocessing, nor considered complex setup. The authors in [83] used the FFT+BPF method inside car and individually performed 4 individual experiments for four testees, respectively (3 male and 1 female at 1 meter away from the radar). They reported that the mean error in breaths is 1.06 times per minute. Due to the use of preprocessing in our project, the estimation accuracies of breathing rate using the FFT+BPF method at 70 cm and 250 cm are both 100%, indicating that the preprocessing algorithm has improved the estimation accuracy. The paper [68] individually estimated the HR of two targets sitting in the car at 1.5m (front seat) and 2m (back seat) respectively. The heartbeat error rate of the target in the front seat is 7.34% and in the back seat is 11.5%. Because of the different scenarios and different measurement distances in [68], we cannot compare our experimental results in this thesis with the results in the reference. Nevertheless, we can see that the VMD algorithm could accurately estimate the number of heartbeats within a distance of 2 m. The authors of [69] reported the HR estimation result of the EEMD method for a target at 50 cm away from the radar. However, their experimental setup is not based on a real person. Rather, they used a chest model with a 5-layer structure (front-cavity, front-lung, heart, back-lung and back-cavity) for simulation and finally got an error rate of 1.5 –3.75%.

Table 4.7: HR and BR estimation results reported in related literature

Vital Sign Assessed	Estimation Method	References	Experimental setup Range/Subjects/Ground Truth Method	Results
BR	FFT + BPF	[83]	1 m inside car/ 3 male, 1 female / ECG	Mean error: 1.06 breathing rate per minute
HR	VMD	[68]	Up to 1.5 m and 2 m (inside car) /2 human (one driver and one target) /Oximeter	Error rate for only driver HR: 7.34% Error rate for one targets in car HR:11.5%
HR	EEMD	[69]	50 cm/Human tissue /simulation results	Error rate: 1.5–3.75%

4.2 Double Targets Estimation

This section carries out two experiments to detect the breathing signal of two targets simultaneously. We consider two main scenarios in our experimentation: double targets detection at different distances and double target detection at the same distance. Here, we pay more attention to the breathing signals detected by the algorithms since we want to observe whether the breathing signals of two targets will interfere with each other. Then we will use the equation 4.1 mentioned above to estimate the error rate and compare the results from different algorithms.

4.2.1 Double breaths detection at different distances

We first consider two targets at different distances, facing the radar, where one target is at a distance of 110 cm and the other at 250 cm to the radar. Fig.4.19 shows the scenario of the experiment. As the purpose of this experiment is to observe the influence of the distance on the testees breathing, we divide the range bin into two intervals (50 cm-150 cm, and 150 cm-300 cm), and use the positioning algorithm in Chapter 3 to find the tester's breathing component in two intervals, respectively. Fig.4.20 shows the breathing signal of object 1 at 110 cm and Fig.4.21 shows the breathing component of object 2 at 270cm.

As seen from the figure, the breathing signal at 110 cm is displayed with a low error rate. It means that due to the relatively short distance to radar, the breathing signal of object 1 can be easily identified and the true BR reported by the video is 13. Furthermore, the BR estimated by all algorithms have an error rate $\leq 10\%$ (except for the EMD algorithm which lost one breath counting), as shown in Table 4.8.

Figure 4.19: Different distance double breathing experiment scenario

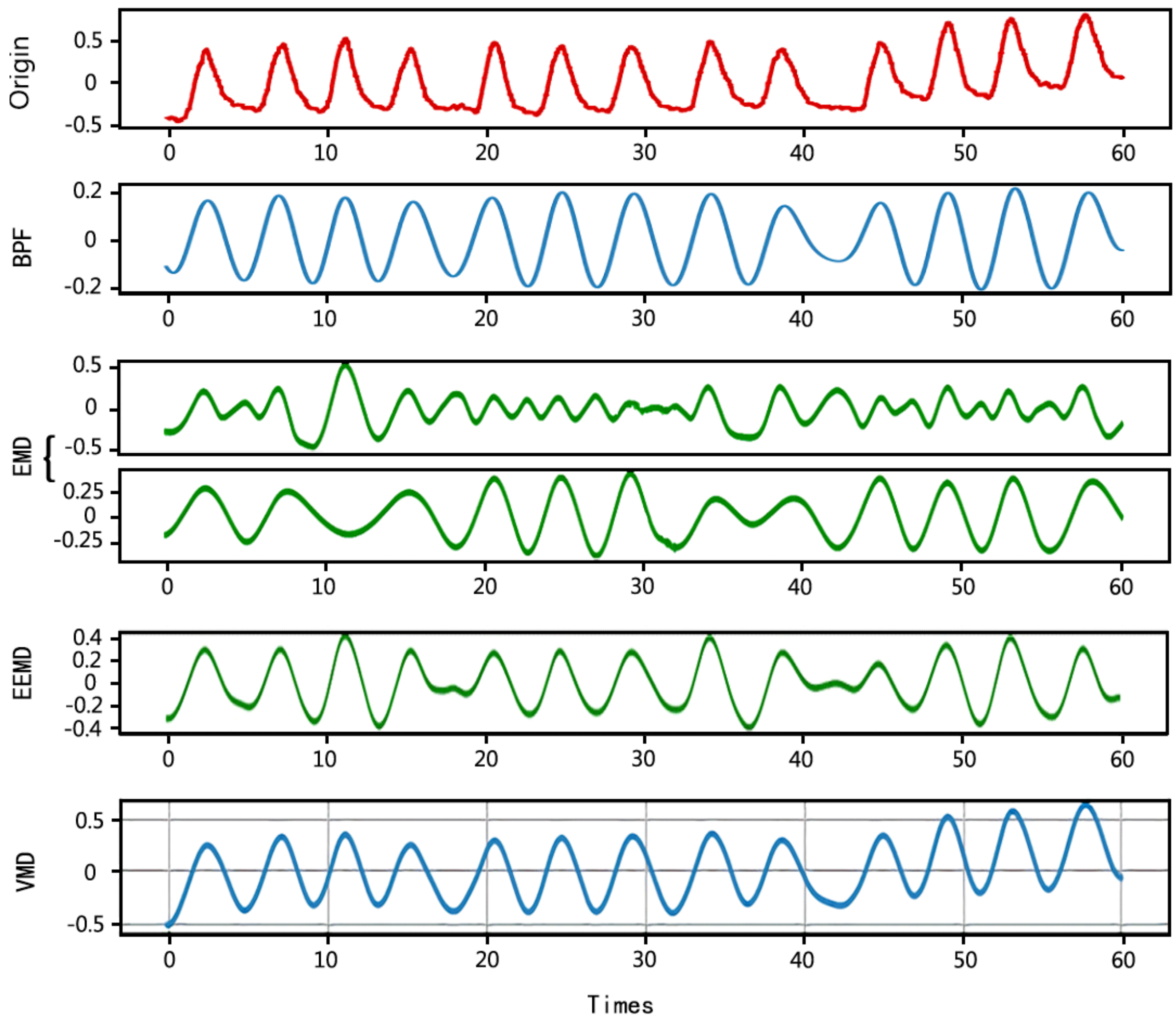

Figure 4.20: Breathing signal of object 1 at 110 cm

Table 4.8: BR estimation results of object 1 at 110 cm obtained from four algorithms in double breathing experiment

	Breathing (one minute)				
	FFT+BPF	EMD	EEMD	VMD	Reported
Testee	13	12	13	13	13
Error rate	0.0%	7.7%	0.0%	0.0%	

Next, we detect the breathing signed of the object at a distance of 270 cm. Due to various noise influences, we can see that there is a lot of noise and clutter in the initial signal, and the ground truth reported by video is 19 in a one-minute experiment. It is seen that the BR obtained by the FFT+BPF and VMD methods can accurately measure the respiratory rate. The other two algorithms suffered from mode mixing caused by noise and signal attenuation. Table 4.9 shows the estimation results of four algorithms.

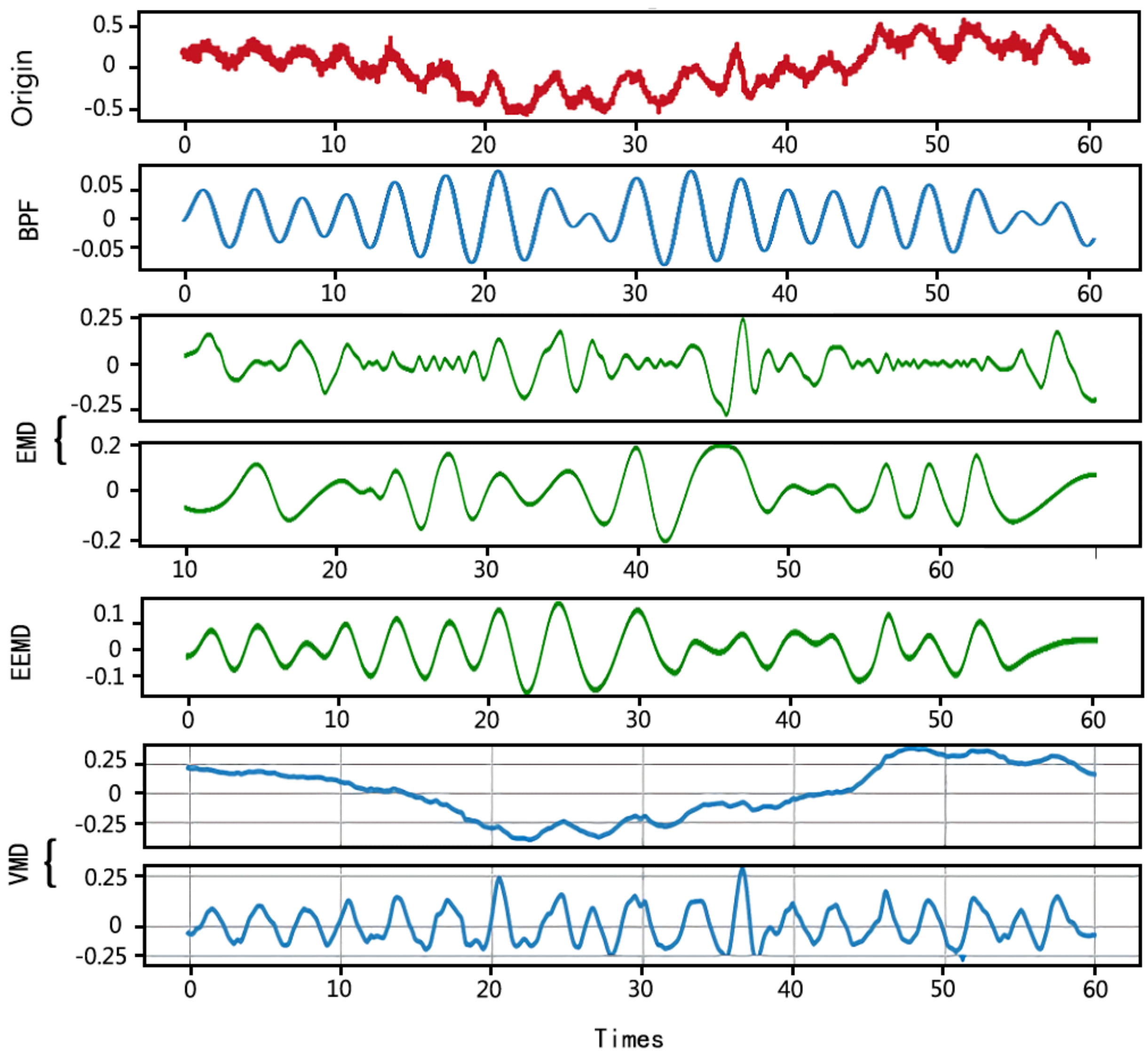

Figure 4.21: Breathing signal of object 2 at 270 cm

Table 4.9: BR estimation results of object 2 at 270 cm obtained from four algorithms in double breathing experiment

	Breathing (one minute)				
	FFT+BPF	EMD	EEMD	VMD	Reported
Testee	19	9	13	19	19
Error rate	0.0%	52.7%	31.6%	0.0%	

The above experiments show that the breathing signals of the two targets at 110 cm and 270 cm can be separated successfully, implying that at these two distances, the objects' breathing signals do not interfere with each other.

4.2.2 Double breaths separation at the same distance

Here, we try to employ a single UWB radar sensor to detect multiple targets located around the same distance, even though the signals from different human bodies may interfere with each other, which is the 'shading effect'.

In the experiment, testees were located at 1.5 meters away from the radar and were asked to lean their shoulders against each other and face the radar during the detection. Fig.4.22 shows the experimental scene.

Figure 4.22: Shading effects experiment scenario

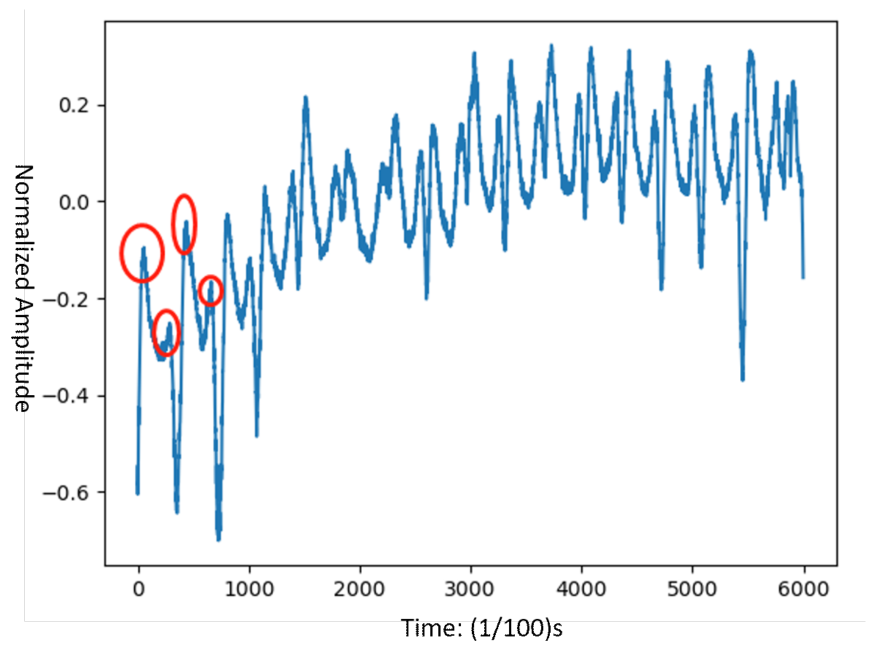

Figure 4.23: Selected signal after preprocessing

The selected signal after preprocessing is shown in Fig.4.23. From the image after preprocessing, we can clearly see that both breathing signals are aliased. Fig.4.24 shows the detected breathing signal. We can see that the FFT+BPF, EMD, and EEMD algorithms completely failed to separate the signals, whereas the VMD algorithm can distinguish the breathing signals of the two objects.

The BR estimation results obtained by four algorithms from two objects are listed in Table 4.10. It should be pointed out that in order to distinguish between the two breathing curves, we compared the breathing curves obtained by EEMD and VMD to the video stample one-to-one, and obtained the breathing curves of each person respectively.

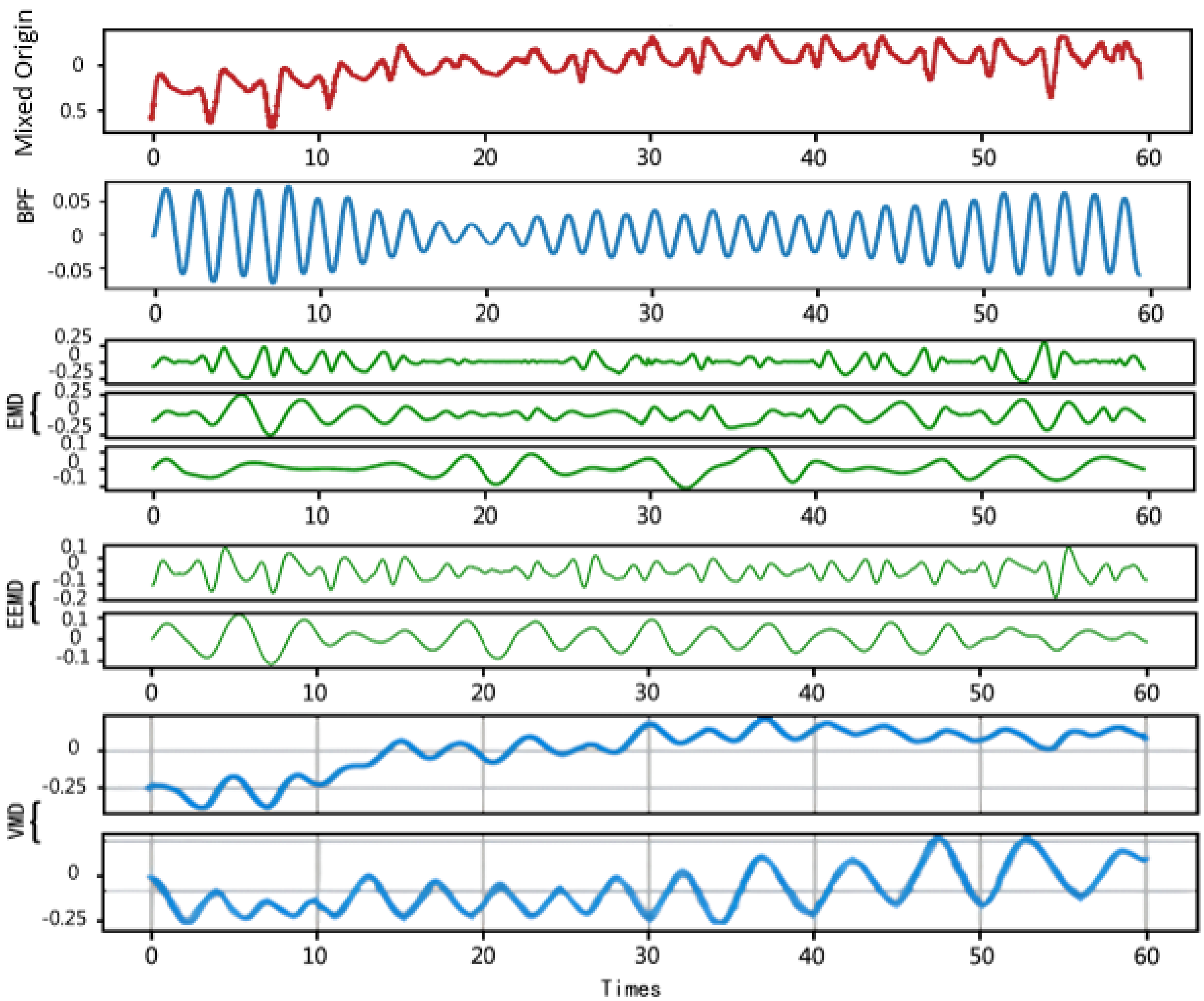

Figure 4.24: Double breathing separation

Table 4.10: BR estimation results from four algorithms for the double breathing at same distance

	Breathing				
	FFT+BPF	EMD	EEMD	VMD	Reported
Target1	Can not be separated	Can not be separated	17	16	18
Error rate	✖	✖	5.5%	11.1%	
Target2	Can not be separated	Can not be separated	Can not be separated	14	16
Error rate	✖	✖	✖	12.5%	

It should be mentioned that there are very limited works on separating double breaths. The authors in [81] used the VMD algorithm to separate both double breaths and triple breaths successfully but did not explain the accuracy of the measurement results. In general, multi breathing detection is a challenging and open topic. In this thesis, the experiments of the double breathing detection have focused on confirmatory exploration and tentative analysis. More experiments to verify the reliability and accuracy of different algorithms, will be needed to optimize these algorithms in the future.

4.2.3 Summary

In this chapter, we have carried out two large groups of experiments, namely single person vital signs detection and double breathing detection, and used equation 4.1 to calculate the error rate in different scenarios of a single person and double persons estimation. Based on the experimental results, the advantages and disadvantages of each algorithm are explained. From all the above single radar experiments, we can draw the following conclusions:

- XeThru X4 UWB radar can estimate the HR in a lower error rate within 2.5m.
- The FFT+BPF method is the most straightforward algorithm which takes the shortest time (in python) for estimation among the four algorithms. It is suitable for simple scenarios (facing radar) and positions (keep almost stationary), but this algorithm cannot eliminate

the signal mixing caused by human body micro-movement and thus causes great estimation errors.

- The EMD algorithm as a simple version of the EEMD algorithm can sometimes separate breathing signals from the body's micro-movements, but mode mixing will always take place when vital signs frequency changes or micro-movements occurs.

- The overall stability and accuracy of EEMD algorithm are higher than the EMD algorithm. However, the normalized amplitude of the respiratory waveform could be omitted.

- The VMD algorithm in general outperforms other algorithms. It has strong theoretical support for estimation, avoids the instability of EMD decomposition, and overcomes the shortcoming (easily affected by fretting and noise) of the respiratory IMF obtained by EMD and EEMD. In addition, VMD has a shortcoming that requires to determine the number of modes and the value of α. Meanwhile, these parameters heavily depend on applications and may be difficult to obtain beforehand.

In the multi-person breathing signal detection, we can reach the following conclusion

- When two objects are not located at the same distance to radar, the object closer to the radar will not affect the breath detection of the object far from the radar.

- When the two targets are located at the same distance, the FFT+BPF and EMD algorithms can not separate the mixed breathing signal at all, but the EEMD algorithm can separate only one breathing signal and the VMD can separate both breathing signals.

Chapter 5

Conclusion and Future Work

5.1 Conclusion

Heartbeat and breathing (respiration) are important vital signs of the human body. The traditional contact based detection methods for instance, electrocardiograph (ECG), photoplethysmography (PPG), etc., have many limitations especially for patients with severe infections and elderly people. Nowadays, non-contact vital signs detection technology has received growing attention. Due to the advantages such as wide bandwidth, high resolution, small size etc., UWB radar has been used in the health care systems. In this thesis, the movement on the surface of the human chest wall caused by breathing and heartbeat was detected using UWB radar. The breathing and heart rate have been estimated by processing the radar echo signals with several signal processing algorithms.

- First, state-of-the-art in the field of vital signal detection using radar technology has been reviewed, based on which the advantages of contactless detection and UWB radar-based technology were highlighted.
- The principle of UWB radar detecting vital signs was discussed in detail, followed by the introduction of the XeThru UWB radar system provided by Moonshot Health Company from the perspective of hardware structure and signal processing flow.

- Several preprocessing algorithms have been investigated to enhance the radar echo signal in order to improve the estimation accuracy of the breathing and heart rate. These preprocessing methods included SVD-based clutter and noise removal algorithms, the largest variance-based target detection method, and the autocorrelation-based breathing-like signal identification method.

- The thesis has then investigated four time-frequency analysis algorithms (FFT+BPF, EMD, EEMD and VMD) and compared their performance in estimating the BR and HR in different application scenarios.

- A large number of experiments have been conducted to evaluate the four algorithms. In single target vital signs detection, the FFT+BPF method is the best algorithm which takes the shortest estimation time and gives high accuracy in the simple scenarios (facing radar and keeping almost stationary). However, in the challenging scenarios, the VMD algorithm has the highest accuracy and the widest applicability.

- Extensive experiments were also undertaken for double objects' breathing estimation. It was shown that when the two objects are not located at the same distance to radar, their breathing signals are not interfered with each other. However, when they are very close or at the same distance to the radar, only VMD algorithm can separate mixed breathing signals.

5.2 Limitations and Future Work

Although many previous studies led to positive results in the detection of vital signs by UWB radar, there are still many limitations that limit the development of this technology as shown below:

- Most of the work in this field concentrated on test cases where the testees are almost stationary. However, in the real world, the testees may make large random body movements that adversely affect the reception of the radar echo signal. Current algorithms can only detect motion signals that do not contain biological signals, but how to extract vital signs from moving objects is still a difficult problem.

- The vital signs monitoring system is still not advanced enough and needs further optimization. Specifically, the current life signal radar detection program based on the LUNNA embedded system is suitable only for a few vital signs detection algorithms, which means this system needs more compatible algorithms to test the accuracy of life signals in different scenarios.

- Explorations are not made to distinguish between other motions generated by background sources including fans, water droplets falling from the faucet etc., which influence breathing rate estimation under periodic or random motion situations. Possible future research could be to analyse the influence of other physical motion sources on the radar surveillance.

Although it is widely recognized that UWB radar can penetrate solid obstacles not made of metal such as partition walls etc., the exploration of the role of solid obstacles between radar and objects has not been made in this study, which will be an interesting topic for future research. Some other possible future work based on this thesis may contain the following.

- The performance of the algorithm introduced in this study will be further evaluated under practical circumstances such as in a practical elderly care facility center. We plan to collect data from senior citizens in an elderly care institution in Montreal. The difference between the vital signs of the elderly and the young groups will be studied to optimize the algorithms.

- The dual-radar-based vital signs detection will be designed to locate the target's existence in a two-dimensional space and thus significantly improve the accuracy of multi-person life signal detection.

- An intelligent system that recognizes human events and analyzes the vital signs under different situations will be designed. The collection of human events is currently underway, including daily human actions such as falling, strolling, sleeping, sitting/standing up, turning around and squatting.

Finally, with the advent of high-performance and ultra-highly integrated UWB radar chips, more complex detection algorithms will be invented and optimized toward commercialization.

Bibliography

[1] F. Q. AL-Khalidi, R. Saatchi, D. Burke, H. Elphick, and S. Tan. Respiration rate monitoring methods: A review. *Pediatric pulmonology*, 46(6):523–529, 2011.

[2] H. Aoki, Y. Takemura, K. Mimura, and M. Nakajima. Development of non-restrictive sensing system for sleeping person using fiber grating vision sensor. In *MHS2001. Proceedings of 2001 International Symposium on Micromechatronics and Human Science (Cat. No. 01TH8583)*, pages 155–160. IEEE, 2001.

[3] G. Balakrishnan, F. Durand, and J. Guttag. Detecting pulse from head motions in video. In *Proceedings of the IEEE Conference on Computer Vision and Pattern Recognition*, pages 3430–3437, 2013.

[4] O. Boric-Lubecke, V. M. Lubecke, A. D. Droitcour, B.-K. Park, and A. Singh. *Doppler radar physiological sensing*. Wiley Online Library, 2016.

[5] W. Bouachir, R. Gouiaa, B. Li, and R. Noumeir. Intelligent video surveillance for real-time detection of suicide attempts. *Pattern Recognition Letters*, 110:1–7, 2018.

[6] B. Chen, X. Chen, Y. Huang, and J. Guan. Transmit beampattern synthesis for the fda radar. *IEEE Antennas and Wireless Propagation Letters*, 17(1):98–101, 2017.

[7] V. C. Chen, F. Li, S.-S. Ho, and H. Wechsler. Micro-doppler effect in radar: phenomenon, model, and simulation study. *IEEE Transactions on Aerospace and electronic systems*, 42(1):2–21, 2006.

[8] V. C. Chen, F. Li, S.-S. Ho, and H. Wechsler. Micro-doppler effect in radar: phenomenon, model, and simulation study. *IEEE Transactions on Aerospace and electronic systems*, 42(1):2–21, 2006.

[9] Y. Chen, E. Gunawan, K. S. Low, C. Boon, C. B. Soh, and L. L. Thi. Human respiration rate estimation using body-worn ultra-wideband radar. In *2007 IEEE Antennas and Propagation Society International Symposium*, pages 265–268. IEEE, 2007.

[10] Y. M. Chi, T.-P. Jung, and G. Cauwenberghs. Dry-contact and noncontact biopotential electrodes: Methodological review. *IEEE reviews in biomedical engineering*, 3:106–119, 2010.

[11] H.-S. Cho and Y.-J. Park. Detection of heart rate through a wall using uwb impulse radar. *Journal of healthcare engineering*, 2018, 2018.

[12] P. De Chazal, N. Fox, E. O'HARE, C. Heneghan, A. Zaffaroni, P. Boyle, S. Smith, C. O'CONNELL, and W. T. McNicholas. Sleep/wake measurement using a non-contact biomotion sensor. *Journal of sleep research*, 20(2):356–366, 2011.

[13] C. Ding, J. Yan, L. Zhang, H. Zhao, H. Hong, and X. Zhu. Noncontact multiple targets vital sign detection based on vmd algorithm. In *2017 IEEE Radar Conference (RadarConf)*, pages 0727–0730. IEEE, 2017.

[14] H. Donald, Alber, E. David, H., W. Ewald, R., B. Peter, H., and A. Robert. Respiratory system. `https://www.lung.ca/lung-health/lunginfo/respiratory-system`, accessed 14 April 2020.

[15] M. Donelli. A rescue radar system for the detection of victims trapped under rubble based on the independent component analysis algorithm. *Progress In Electromagnetics Research*, 19:173–181, 2011.

[16] K. Dragomiretskiy and D. Zosso. Variational mode decomposition. *IEEE transactions on signal processing*, 62(3):531–544, 2013.

[17] A. D. Droitcour, O. Boric-Lubecke, V. M. Lubecke, J. Lin, and G. T. Kovacs. Range correlation effect on ism band i/q cmos radar for non-contact vital signs sensing. In *IEEE MTT-S International Microwave Symposium Digest, 2003*, volume 3, pages 1945–1948. IEEE, 2003.

[18] D. N. Dutta, R. Das, and S. Pal. Automated real-time processing of single lead electrocardiogram for simultaneous heart rate and respiratory rate monitoring. *Journal of Medical Devices*, 11(2), 2017.

[19] C. Eren, S. Karamzadeh, and M. Kartal. The artifacts of human physical motions on vital signs monitoring. In *2019 Scientific Meeting on Electrical-Electronics & Biomedical Engineering and Computer Science (EBBT)*, pages 1–5. IEEE, 2019.

[20] T. Ø. Fossum. Exploration of micro-doppler signatures associated with humans and dogs using uwb radar. Master's thesis, NTNU, 2015.

[21] M. Garbey, N. Sun, A. Merla, and I. Pavlidis. Contact-free measurement of cardiac pulse based on the analysis of thermal imagery. *IEEE transactions on Biomedical Engineering*, 54(8):1418–1426, 2007.

[22] S. Gezici and H. V. Poor. Position estimation via ultra-wide-band signals. *Proceedings of the IEEE*, 97(2):386–403, 2009.

[23] A. L. Goldberger, Z. D. Goldberger, and A. Shvilkin. *Clinical electrocardiography: a simplified approach e-book*. Elsevier Health Sciences, 2017.

[24] S. Z. Gurbuz and M. G. Amin. Radar-based human-motion recognition with deep learning: Promising applications for indoor monitoring. *IEEE Signal Processing Magazine*, 36(4):16–28, 2019.

[25] N. Hallfors, M. Alhawari, M. Abi Jaoude, Y. Kifle, H. Saleh, K. Liao, M. Ismail, and A. Isakovic. Graphene oxide: Nylon ecg sensors for wearable iot healthcare—nanomaterial and soc interface. *Analog Integrated Circuits and Signal Processing*, 96(2):253–260, 2018.

[26] K.-P. Hoffmann and R. Ruff. Flexible dry surface-electrodes for ecg long-term monitoring. In *2007 29th Annual International Conference of the IEEE Engineering in Medicine and Biology Society*, pages 5739–5742. IEEE, 2007.

[27] C.-C. Hsu, B.-S. Lin, K.-Y. He, and B.-S. Lin. Design of a wearable 12-lead noncontact electrocardiogram monitoring system. *Sensors*, 19(7):1509, 2019.

[28] I. Immoreev and T.-H. Tao. Uwb radar for patient monitoring. *IEEE Aerospace and Electronic Systems Magazine*, 23(11):11–18, 2008.

[29] B.-J. Jang, S.-H. Wi, J.-G. Yook, M.-Q. Lee, and K.-J. Lee. Wireless bio-radar sensor for heartbeat and respiration detection. *Progress In Electromagnetics Research*, 5:149–168, 2008.

[30] Q. Jian, J. Yang, Y. Yu, P. Björkholm, and T. McKelvey. Detection of breathing and heartbeat by using a simple uwb radar system. In *The 8th European Conference on Antennas and Propagation (EuCAP 2014)*, pages 3078–3081. IEEE, 2014.

[31] F. Khan and S. H. Cho. A detailed algorithm for vital sign monitoring of a stationary/non-stationary human through ir-uwb radar. *Sensors*, 17(2):290, 2017.

[32] F. Khan, J. W. Choi, and S. H. Cho. Vital sign monitoring of a non-stationary human through ir-uwb radar. In *2014 4th IEEE International Conference on Network Infrastructure and Digital Content*, pages 511–514. IEEE, 2014.

[33] F. Khan, A. Ghaffar, N. Khan, and S. H. Cho. An overview of signal processing techniques for remote health monitoring using impulse radio uwb transceiver. *Sensors*, 20(9):2479, 2020.

[34] G. Kirose and T. Dogaru. Study of the human body radar signature variability based on computer models. In *Radar Sensor Technology XIV*, volume 7669, page 766915. International Society for Optics and Photonics, 2010.

[35] E. Knott, J. Shaeffer, and M. Tuley. Radar cross section 2nd edn (boston, ma: Artech house). 1993.

[36] T. Kondo, T. Uhlig, P. Pemberton, and P. Sly. Laser monitoring of chest wall displacement. *European Respiratory Journal*, 10(8):1865–1869, 1997.

[37] J. Kuutti, M. Paukkunen, M. Aalto, P. Eskelinen, and R. E. Sepponen. Evaluation of a doppler radar sensor system for vital signs detection and activity monitoring in a radio-frequency shielded room. *Measurement*, 68:135–142, 2015.

[38] S. Kwon, J. Lee, G. S. Chung, and K. S. Park. Validation of heart rate extraction through an iphone accelerometer. In *2011 Annual International Conference of the IEEE Engineering in Medicine and Biology Society*, pages 5260–5263. IEEE, 2011.

[39] C.-P. Lai. Through wall surveillance using ultrawideband random noise radar. 2007.

[40] A. Lazaro, D. Girbau, and R. Villarino. Analysis of vital signs monitoring using an ir-uwb radar. *Progress In Electromagnetics Research*, 100:265–284, 2010.

[41] A. Lazaro, D. Girbau, and R. Villarino. Techniques for clutter suppression in the presence of body movements during the detection of respiratory activity through uwb radars. *Sensors*, 14(2):2595–2618, 2014.

[42] K.-C. Lee, J.-S. Ou, and M.-C. Fang. Application of svd noise-reduction technique to pca based radar target recognition. *Progress In Electromagnetics Research*, 81:447–459, 2008.

[43] S. K. Leem, F. Khan, and S. H. Cho. Vital sign monitoring and mobile phone usage detection using ir-uwb radar for intended use in car crash prevention. *Sensors*, 17(6):1240, 2017.

[44] M. Leib, W. Menzel, B. Schleicher, and H. Schumacher. Vital signs monitoring with a uwb radar based on a correlation receiver. In *Proceedings of the Fourth European Conference on Antennas and Propagation*, pages 1–5. IEEE, 2010.

[45] B. Levitas and J. Matuzas. Uwb radar for human being detection behind the wall. In *2006 International Radar Symposium*, pages 1–3. IEEE, 2006.

[46] C. Li. *Non-contract estimation of respiration and heartbeat rate using ultra-wideband signals*. PhD thesis, Virginia Tech, 2008.

[47] C. Li and J. Lin. Optimal carrier frequency of non-contact vital sign detectors. In *2007 IEEE Radio and Wireless Symposium*, pages 281–284. IEEE, 2007.

[48] C. Li and J. Lin. Complex signal demodulation and random body movement cancellation techniques for non-contact vital sign detection. In *2008 IEEE MTT-S International Microwave Symposium Digest*, pages 567–570. IEEE, 2008.

[49] X. Liang, Y. Wang, S. Wu, and T. A. Gulliver. Experimental study of wireless monitoring of human respiratory movements using uwb impulse radar systems. *Sensors*, 18(9):3065, 2018.

[50] X. Liang, H. Zhang, S. Ye, G. Fang, and T. A. Gulliver. Improved denoising method for through-wall vital sign detection using uwb impulse radar. *Digital Signal Processing*, 74:72–93, 2018.

[51] Y. Liao. Phase and frequency estimation: High-accuracy and low-complexity techniques. 2011.

[52] Y. G. Lim, K. K. Kim, and K. S. Park. Ecg recording on a bed during sleep without direct skin-contact. *IEEE Transactions on Biomedical Engineering*, 54(4):718–725, 2007.

[53] Y. G. Lim, K. K. Kim, and S. Park. Ecg measurement on a chair without conductive contact. *IEEE Transactions on Biomedical Engineering*, 53(5):956–959, 2006.

[54] J. C. Lin. Noninvasive microwave measurement of respiration. *Proceedings of the IEEE*, 63(10):1530–1530, 1975.

[55] L. Liu, Z. Liu, H. Xie, B. Barrowes, and A. C. Bagtzoglou. Numerical simulation of uwb impulse radar vital sign detection at an earthquake disaster site. *Ad Hoc Networks*, 13:34–41, 2014.

[56] M. H. E. M. Mabrouk. *Signal Processing of UWB Radar Signals for Human Detection Behind Walls*. PhD thesis, Université d'Ottawa/University of Ottawa, 2015.

[57] A. Markman, X. Shen, and B. Javidi. Three-dimensional object visualization and detection in low light illumination using integral imaging. *Optics Letters*, 42(16):3068–3071, 2017.

[58] S. D. Min, J. K. Kim, H. S. Shin, Y. H. Yun, C. K. Lee, and M. Lee. Noncontact respiration rate measurement system using an ultrasonic proximity sensor. *IEEE sensors journal*, 10(11):1732–1739, 2010.

[59] H. Monkaresi, R. A. Calvo, and H. Yan. A machine learning approach to improve contactless heart rate monitoring using a webcam. *IEEE journal of biomedical and health informatics*, 18(4):1153–1160, 2013.

[60] K. Nakajima, Y. Matsumoto, and T. Tamura. Development of real-time image sequence analysis for evaluating posture change and respiratory rate of a subject in bed. *Physiological Measurement*, 22(3):N21, 2001.

[61] V. Nguyen, A. Q. Javaid, and M. A. Weitnauer. Harmonic path (hapa) algorithm for non-contact vital signs monitoring with ir-uwb radar. In *2013 IEEE Biomedical Circuits and Systems Conference (BioCAS)*, pages 146–149. IEEE, 2013.

[62] M.-Z. Poh, D. J. McDuff, and R. W. Picard. Non-contact, automated cardiac pulse measurements using video imaging and blind source separation. *Optics express*, 18(10):10762–10774, 2010.

[63] L. Ren, Y. S. Koo, H. Wang, Y. Wang, Q. Liu, and A. E. Fathy. Noncontact multiple heartbeats detection and subject localization using uwb impulse doppler radar. *IEEE Microwave and Wireless Components Letters*, 25(10):690–692, 2015.

[64] Y. Ren, C. Zhu, and S. Xiao. Deformable faster r-cnn with aggregating multi-layer features for partially occluded object detection in optical remote sensing images. *Remote Sensing*, 10(9):1470, 2018.

[65] J. Sachs, M. Helbig, R. Herrmann, M. Kmec, K. Schilling, and E. Zaikov. Remote vital sign detection for rescue, security, and medical care by ultra-wideband pseudo-noise radar. *Ad Hoc Networks*, 13:42–53, 2014.

[66] M. Schmidt, A. Schumann, J. Müller, K.-J. Bär, and G. Rose. Ecg derived respiration: comparison of time-domain approaches and application to altered breathing patterns of patients with schizophrenia. *Physiological measurement*, 38(4):601, 2017.

[67] M. Sekine and K. Maeno. Non-contact heart rate detection using periodic variation in doppler frequency. In *2011 IEEE Sensors Applications Symposium*, pages 318–322. IEEE, 2011.

[68] H. Shen, C. Xu, Y. Yang, L. Sun, Z. Cai, L. Bai, E. Clancy, and X. Huang. Respiration and heartbeat rates measurement based on autocorrelation using ir-uwb radar. *IEEE Transactions on Circuits and Systems II: Express Briefs*, 65(10):1470–1474, 2018.

[69] K.-K. Shyu, L.-J. Chiu, P.-L. Lee, T.-H. Tung, and S.-H. Yang. Detection of breathing and heart rates in uwb radar sensor data using fvpief-based two-layer eemd. *IEEE Sensors Journal*, 19(2):774–784, 2018.

[70] A. Sikdar, S. K. Behera, and D. P. Dogra. Computer-vision-guided human pulse rate estimation: a review. *IEEE reviews in biomedical engineering*, 9:91–105, 2016.

[71] S. Singh, Q. Liang, D. Chen, and L. Sheng. Sense through wall human detection using uwb radar. *EURASIP Journal on Wireless Communications and Networking*, 2011(1):1–11, 2011.

[72] S. Sonkusare, D. Ahmedt-Aristizabal, M. J. Aburn, V. T. Nguyen, T. Pang, S. Frydman, S. Denman, C. Fookes, M. Breakspear, and C. C. Guo. Detecting changes in facial temperature induced by a sudden auditory stimulus based on deep learning-assisted face tracking. *Scientific reports*, 9(1):1–11, 2019.

[73] J. Sun and M. Li. Life detection and location methods using uwb impulse radar in a coal mine. *Mining Science and Technology (China)*, 21(5):687–691, 2011.

[74] N. Tateishi, A. Mase, L. Bruskin, Y. Kogi, N. Ito, T. Shirakata, and S. Yoshida. Microwave measurement of heart beat and analysis using wavelet transform. In *2007 Asia-Pacific Microwave Conference*, pages 2151–2153. IEEE, 2007.

[75] P. K. Verma, A. N. Gaikwad, D. Singh, and M. Nigam. Analysis of clutter reduction techniques for through wall imaging in uwb range. *Progress In Electromagnetics Research*, 17:29–48, 2009.

[76] T. Wang, D. Zhang, L. Wang, Y. Zheng, T. Gu, B. Dorizzi, and X. Zhou. Contactless respiration monitoring using ultrasound signal with off-the-shelf audio devices. *IEEE Internet of Things Journal*, 6(2):2959–2973, 2018.

[77] P. Welch. The use of fast fourier transform for the estimation of power spectra: a method based on time averaging over short, modified periodograms. *IEEE Transactions on audio and electroacoustics*, 15(2):70–73, 1967.

[78] Z. Wu and N. E. Huang. Ensemble empirical mode decomposition: a noise-assisted data analysis method. *Advances in adaptive data analysis*, 1(01):1–41, 2009.

[79] Z. Wu, N. E. Huang, and X. Chen. The multi-dimensional ensemble empirical mode decomposition method. *Advances in Adaptive Data Analysis*, 1(03):339–372, 2009.

[80] Y. Xu, S. Dai, S. Wu, J. Chen, and G. Fang. Vital sign detection method based on multiple higher order cumulant for ultrawideband radar. *IEEE Transactions on Geoscience and Remote Sensing*, 50(4):1254–1265, 2011.

[81] J. Yan, H. Hong, H. Zhao, Y. Li, C. Gu, and X. Zhu. Through-wall multiple targets vital signs tracking based on vmd algorithm. *Sensors*, 16(8):1293, 2016.

[82] D. Yang, Z. Zhu, J. Zhang, and B. Liang. The overview of human localization and vital sign signal measurement using handheld ir-uwb through-wall radar. *Sensors*, 21(2):402, 2021.

[83] Z. Yang, M. Bocca, V. Jain, and P. Mohapatra. Contactless breathing rate monitoring in vehicle using uwb radar. In *Proceedings of the 7th International Workshop on Real-World Embedded Wireless Systems and Networks*, pages 13–18, 2018.

[84] A. Yarovoy, L. Ligthart, J. Matuzas, and B. Levitas. Uwb radar for human being detection. *IEEE Aerospace and Electronic Systems Magazine*, 21(3):10–14, 2006.

[85] W. Yin, X. Yang, L. Li, L. Zhang, N. Kitsuwan, and E. Oki. Hear: Approach for heartbeat monitoring with body movement compensation by ir-uwb radar. *Sensors*, 18(9):3077, 2018.

[86] J. Yoo, L. Yan, S. Lee, H. Kim, and H.-J. Yoo. A wearable ecg acquisition system with compact planar-fashionable circuit board-based shirt. *IEEE Transactions on Information Technology in Biomedicine*, 13(6):897–902, 2009.

[87] Y. Zhang, M. Amin, and F. Ahmad. Time-frequency analysis for the localization of multiple moving targets using dual-frequency radars. *IEEE Signal Processing Letters*, 15:777–780, 2008.

[88] D. Zito and D. Pepe. Monitoring respiratory pattern in adult and infant via contactless detection of thorax and abdomen movements through soc uwb pulse radar sensor. In *2014 IEEE Topical Conference on Biomedical Wireless Technologies, Networks, and Sensing Systems (BioWireleSS)*, pages 1–3. IEEE, 2014.

[89] D. Zito, D. Pepe, B. Neri, D. De Rossi, A. Lanata, A. Tognetti, and E. P. Scilingo. Wearable system-on-a-chip uwb radar for health care and its application to the safety improvement of emergency operators. In *2007 29th Annual International Conference of the IEEE Engineering in Medicine and Biology Society*, pages 2651–2654. IEEE, 2007.